Prediction of the effects of drugs on cardiac activity using computer simulations

Jordi Cano García

Supervisors

Dra. Lucía Romero Pérez

Dr. Francisco Javier Saiz Rodríguez

Valencia, January 2021

PhD. Tesis submitted to the Centro de Investicación e Innovación en Bioingeniería (CI2B) in fulfillment of the requirements for the degree of Doctor in Tecnologías para el Bienestar y la Salud at Universitat Politècnica de València, València, Spain

UNIVERSITAT
POLITÈCNICA
DE VALÈNCIA

Supervisors

Dra. Lucía Romero Pérez

Universitat Politècnica de València, Spain

Dr. Francisco Javier Saiz Rodríguez

Universitat Politècnica de València, Spain

External Evaluators

-

-

-

-

-

-

Reading Committee

-

-

-

This work was carried out in the *Centro de Investigación e Innovación en Bioingeniería* (Ci2B) at the Universitat Politècnica de València, Spain.

To my beloved parents, José Juan and Susima, to whom I owe everything. Especially in these hard moments, I wish to give you all my energy through this work.

To my precious family, who were there when I needed them.

To my dear friends, whose support was also invaluable.

Acknowledgements

I would like to express my profound gratitude to all the people that, in a direct or indirect way, has supported the consecution of this PhD thesis. I sincerely would have not been able to finish this work without their help.

First of all, I wish to thank my supervisors, Lucía Romero and Javier Saiz, whose excellent guidance and dedication to this project have crystallized into this document. Their professionalism and enthusiasm have enlightened the way during these 5 years of hard work. With them, this PhD thesis was not only interesting, but also fun. I would like to thank them for giving me the opportunity to work together, to be part of this community. Thank you also for those long meetings filled with printed documents and figures. I especially would like to thank Lucía Romero for her profound commitment and perseverance. Not only her knowledge in cardiac electrophysiology and modeling was key to finding the solutions to the obstacles that arose on the way, but her nice character made tackling the hardest problems a fun experience. I will always remember how she never gave up. For that and many more reasons, I will be always grateful.

Second, I would like to express my gratitude to all the people who shared their precious time with me during the development of this PhD thesis. I would like to thank Alejandro Daniel López, Laura Martínez and Juan Francisco Gómez for their support and knowledge as they were facing similar challenges while developing their own PhD thesis. Thank you for sharing your experience, which was crucial to solve the everyday struggle. I also would like to thank Julio Gomis-Tena for introducing me to simulation in our cluster and sharing great advice during the development of our Tx biomarker, and to José María Ferrero for giving me that extra bit of knowledge about sodium channels that made me open my mind. Last but certainly not least, I would like to thank Ángel Montoya and Juan José Manclús for their interesting conversations and for sharing their experiences with me during uncountable lunch times. Special thanks also to Sara, Edhison, Jordi, Rebecca, Víctor, Jorge and Fernando. You made working in our "pool" much more fun and interesting.

Finally, I would like to express my greatest gratitude to my family, to whom I owe having been able to live and work for my PhD thesis during these 5 years. My parents' advice and support has been invaluable to the consecution of this stage of my life and I could not be more grateful. Thank you for your continuous overwatch and for being there for me. This is the result of your efforts too, so I proudly dedicate this to you.

Abstract

Cardiovascular disease remains the main cause of death in Europe. Cardiac arrhythmias are an important cause of sudden death, but their mechanisms are complex. This denotes the importance of their study and prevention. Research on cardiac electrophysiology has shown that electrical abnormalities caused by mutations in cardiac channels can trigger arrhythmias. Surprisingly, a wide variety of drugs have also shown proarrhythmic potential, including those that we use to prevent arrhythmia. Current guidelines designed a test to identify dangerous drugs by assessing their blocking power on a single ion channel to address this situation. Study of drug-channel interactions has revealed not only compounds that block multiple channels but also a great complexity in those interactions. This could explain why similar drugs can show vastly different effects in some diseases. There are two important challenges regarding the effects of drugs on cardiac electrophysiology. On the one hand, companies and regulators are in search of a high throughput tool that improves proarrhythmic potential detection during drug development. On the other hand, patients with electrical abnormalities often require safer personalized treatments owing to their condition. Computer simulations provide an unprecedented power to tackle complex biophysical phenomena. They should prove useful determining the characteristics that define the drugs' beneficial and unwanted effects by reproducing experimental and clinical observations.

In this PhD thesis, we used computational models and simulations to address the two abovementioned challenges. We split the study of drug effects on the cardiac activity into the study of their safety and efficacy, respectively. For the former, we took a wider approach and generated a new easy-to-use biomarker for proarrhythmic potential classification using cardiac cell and tissue human action potential models. We integrated multiple channel block through IC_{50}s and therapeutic concentrations to improve its predictive power. Then, we quantified the proarrhythmic potential of 84 drugs to train the biomarker. Our results suggest that it could be used to test the proarrhythmic potential of new drugs. For the second challenge, we took a more specific approach and sought to improve the therapy of patients with cardiac electrical abnormalities. Therefore, we created a detailed model for the long QT syndrome-causing V411M mutation of the sodium channel reproducing clinical and experimental data. We tested the potential benefits of ranolazine, while giving insights into the mechanisms that drive flecainide's effectiveness. Our results suggest that while both drugs showed different mechanisms of sodium channel block, ranolazine could prove beneficial in these patients.

Resumen

Las enfermedades cardiovasculares siguen siendo la principal causa de muerte en Europa. Las arritmias cardíacas son una causa importante de muerte súbita, pero sus mecanismos son complejos. Esto denota la importancia de su estudio y prevención. La investigación sobre electrofisiología cardíaca ha demostrado que las anomalías eléctricas causadas por mutaciones que afectan a canales cardíacos pueden desencadenar arritmias. Sorprendentemente, se ha descubierto una gran variedad de fármacos proarrítmicos, incluidos aquellos que usamos para prevenirlas. Las indicaciones de uso de fármacos actuales intentaron solucionar este problema diseñando una prueba para identificar aquellos fármacos que podían ser peligrosos basado en el bloqueo de un solo canal iónico. El estudio de las interacciones fármaco-canal ha revelado la existencia no sólo de compuestos que bloquean múltiples canales, sino también una gran complejidad en esas interacciones. Esto podría explicar por qué algunos medicamentos pueden mostrar efectos muy diferentes en la misma enfermedad. Existen dos desafíos importantes con respecto a los efectos de los fármacos en la electrofisiología cardíaca. Por un lado, las empresas y entidades reguladoras están buscando una herramienta de alto rendimiento que mejore la detección del potencial proarrítmico durante el desarrollo de fármacos. Por otro lado, los pacientes con anomalías eléctricas a menudo requieren tratamientos personalizados más seguros. Las simulaciones computacionales contienen un poder sin precedentes para abordar fenómenos biofísicos complejos. Deberían ser de utilidad a la hora de determinar las características que definen tanto los efectos beneficiosos como no deseados de los fármacos mediante la reproducción de datos experimentales y clínicos.

En esta tesis doctoral, se han utilizado modelos computacionales y simulaciones para dar respuesta a estos dos desafíos. El estudio de los efectos de los fármacos sobre la actividad cardíaca se dividió en el estudio de su seguridad y de su eficacia, respectivamente. Para dar respuesta al primer desafío, se adoptó un enfoque más amplio y se generó un nuevo biomarcador fácil de usar para la clasificación del potencial proarrítmico de los fármacos utilizando modelos del potencial de acción de células y tejidos cardíacos humanos. Se integró el bloqueo de múltiples canales a través de IC_{50} y el uso de concentraciones terapéuticas con el fin de mejorar el poder predictivo. Luego, se entrenó el biomarcador cuantificando el potencial proarrítmico de 84 fármacos. Los resultados obtenidos sugieren que el biomarcador podría usarse para probar el potencial proarrítmico de nuevos fármacos. Respecto al segundo desafío, se adoptó un enfoque más específico y se buscó mejorar la

terapia de pacientes con anomalías eléctricas cardíacas. Por lo tanto, se creó un modelo detallado de la mutación V411M del canal de sodio, causante del síndrome de QT largo, reproduciendo datos clínicos y experimentales. Se evaluaron los posibles efectos beneficiosos de ranolazina, a la par que se aportó información sobre los mecanismos que impulsan la efectividad de la flecainida. Los resultados obtenidos sugieren que, si bien ambos fármacos mostraron diferentes mecanismos de bloqueo de los canales de sodio, un tratamiento con ranolazina podría ser beneficioso en estos pacientes.

Resum

Les malalties cardiovasculars continuen sent la principal causa de mort a Europa. Les arrítmies cardíaques són una causa important de mort sobtada, però els seus mecanismes són complexos. Això denota la importància del seu estudi i prevenció. La investigació sobre electrofisiologia cardíaca ha demostrat que les anomalies elèctriques que afecten a canals cardiacs poden desencadenar arrítmies. Sorprenentment, s'ha descobert una gran varietat de fàrmacs proarrítmics, inclosos aquells que utilitzem per a previndre-les. Les indicacions d'ús de fàrmacs actuals van intentar solucionar aquest problema dissenyant una prova per a identificar aquells fàrmacs que podien ser perillosos basada en el bloqueig d'un sol canal iònic. L'estudi de les interaccions fàrmac-canal ha revelat l'existència no sols de compostos que bloquegen múltiples canals, sinó també una gran complexitat en aquestes interaccions. Això podria explicar per què alguns medicaments poden mostrar efectes molt diferents en la mateixa malaltia. Existeixen dos desafiaments importants respecte als efectes dels fàrmacs en la electrofisiologia cardíaca. D'una banda, les empreses i entitats reguladores estan buscant una eina d'alt rendiment que millore la detecció del potencial proarrítmic durant el desenvolupament de fàrmacs. D'altra banda, els pacients amb anomalies elèctriques sovint requereixen tractaments personalitzats més segurs. Les simulacions computacionals contenen un poder sense precedents per a abordar fenòmens biofísics complexos. Haurien de ser d'utilitat a l'hora de determinar les característiques que defineixen tant els efectes beneficiosos com no desitjats dels fàrmacs mitjançant la reproducció de dades experimentals i clíniques.

En aquesta tesi doctoral, s'han utilitzat models computacionals i simulacions per a donar resposta a aquests dos desafiaments. L'estudi dels efectes dels fàrmacs sobre l'activitat cardíaca es va dividir en l'estudi de la seva seguretat i la seva eficacia. Per a donar resposta al primer desafiament, es va adoptar un enfocament més ampli i es va generar un nou biomarcador fàcil d'usar per a la classificació del potencial proarrítmic dels fàrmacs utilitzant models del potencial d'acció de cèl·lules i teixits cardíacs humans. Es va integrar el bloqueig de múltiples canals a través d'IC50 i l'ús de concentracions terapèutiques amb la finalitat de millorar el poder predictiu. Després, es va entrenar el biomarcador quantificant el potencial proarrítmic de 84 fàrmacs. Els resultats obtinguts suggereixen que el biomarcador podria usar-se per a provar el potencial proarrítmic de nous fàrmacs. Respecte al segon desafiament, es va adoptar un enfocament més específic i es va buscar millorar la teràpia de pacients amb anomalies elèctriques cardíaques. Per tant, es va crear un model

detallat de la mutació V411M del canal de sodi, causant de la síndrome de QT llarg, reproduint dades clíniques i experimentals. Es van avaluar els possibles efectes beneficiosos de ranolazina, a l'una que es va aportar informació sobre els mecanismes que impulsen l'efectivitat de la flecainida. Els resultats obtinguts suggereixen que, si bé tots dos fàrmacs van mostrar diferents mecanismes de bloqueig dels canals de sodi, un tractament amb ranolazina podria ser beneficiós en aquests pacients.

Contents

Figures List

Tables List

Acronyms

0D	usually refers to isolated cellular models
1D	usually refers to one-dimensional tissues
3D	usually refers to three dimensional matrices of simulation results
A	accuracy
AMP	adenine monophosphate
AP	action potential
APA	action potential amplitude
APDx	action potential duration at x% repolarization
ATP	adenine triphosphate
ATX-II	anemone toxin II
AUC	area under the curve
BCL	basic cycle length in milliseconds
C, D	refers to compound concentrations
C++	programming language
CiPA	comprehensive in vitro in vivo proarrhythmia assay
Cmax	maximum blood concentrations
CVD	cardiovascular disease
DAD	delayed after depolarization
EAD	early after depolarization
EC50	concentration that produces 50% of the Emax
ECG	electrocardiogram
EFTPC	estimated free therapeutic plasma concentration
Emax	maximum effect
FDA	federal drug administration
gap	proteins that enable ion flow between cells
H	the Hill coefficient in the simple pore model
HEK	human embryonic kidney
hERG	human ether-à-go-go related gene coding for IKr
IC50	concentration that inhibits a current to a 50% of its drug-free conditions
ICH	international conference of harmonization
IKr	rapid component of the potassium delayed rectifier current

INaf	fast component of the sodium current
INaL	slow component of the sodium current
Ix	membrane current called x
Jx	ion flux called x
LOO	leave-one-out
LQTS	long QT syndrome
M	Molarity/Molar, a measure of concentration
max dV/dt	maximum upstroke velocity during depolarization
mM, µM, M	millimolar, micromolar, molar
MOT	mean opening time
ODE	ordinary differential equation
ORd model	O'Hara Rudy model of the human ventricular action potential
P	first wave of the normal ECG
pIC50	negative decimal logarithm of the IC50
QRS	three-wave complex of the normal ECG
QSAR	quantitative structure-activity relationship
QT	time interval between the onset of the Q and the end of the T waves in the ECG
QTc	QT interval corrected by a formula that takes heart rate into account
R	onset of the QRS complex of the normal ECG
RMP	resting membrane potential
ROC	reciever operating characteristic
SCN5A	gene coding for the human cardiac sodium current Ina
T	usually the last wave of the ECG
TdP	torsade-de-pointes
TNR	true negative rate or specificity
TPR	true positive rate or sensitivity
TTX	tetrodotoxin
Tx	proarrhythmicity biomarker developed during this PhD thesis
US	Unites States of America
USD	US Dollar
Vm	membrane voltage
WT	wild type

Structure of this thesis

Chapter 1: Introduction. A brief presentation of the reasons that motivate the development of this PhD thesis and an overview of its main objectives.

Chapter 2: State of the art. In this chapter we explore the concepts that will contribute to this PhD thesis' ease of understanding.

Chapter 3: Development of an in-silico TdP biomarker for early proarrhythmicity detection. This chapter focusses on studying drug safety. Simple drug-channel interactions and human action potential models allow us to create a tool for TdP prediction during early stages of drug development.

Chapter 4: Study and modeling of a channelopathy and testing of specific treatments. This chapter focusses on studying drug efficacy. Detailed Ion channel dynamics and drug-channel interactions are used for the development of mutation-specific models to test the potential of an alternative treatment with ranolazine for patients carrying the SCN5A V411M mutation. At the same time, we provide deeper knowledge of drug-channel interactions which explain the obtained results.

Chapter 5: General conclusions. In this chapter, we review the degree of accomplishment of our main objectives.

Chapter 6: Future Work. An overview of the research paths that would extend the results of this PhD thesis.

Chapter 7: Contributions. A list of the works that have been directly or indirectly published owing to the development of this PhD thesis.

Appendix. Optimization procedure. Detailed information on the methods that we follow in Chapter 4.

References. A list of the references that have been consulted for the development of this PhD thesis.

Chapter 1. Introduction

1.1 Motivation

According to an article from the European Commission, cardiovascular disease (CVD) is the leading cause of death in Europe. In 2016, it took the lives of 1.83 million people, or the 35.7% of all deaths, which is almost ten percentage points greater than the second most prevalent cause of death[1]. Around 10 million patients suffering from circulatory diseases are discharged from hospitals every year. Among those, patients with conduction disease or arrhythmia account for 1.6 million people, a value that is bound to rise when reports from all countries become available. The average length of stay of these patients ranges from 4.3 days to values as high as 12.6 days depending on the country, highlighting the difficulties that are related to treating these conditions. The long QT syndrome, which is characterized by an abnormal elongation of the QT segment in the ECG, is one of the causes of death in the young. In fact, it accounts for 10% to 15% of the sudden infant death syndromes[2], which had traditionally been mislabeled. Furthermore, two independent cohort studies found that LQTS is the main cause of unexplained cardiac arrest in adults[3,4]. Electrical abnormalities in the cardiac tissue resulting from mutations in genes coding for transmembrane ion channels are the main cause of LQTS. They do so by altering the electrical dynamics that control the timing and contraction of the cardiac muscle. This syndrome is associated with a severe polymorphic ventricular tachycardia know as Torsade-de-pointes (TdP). This means that leaving the syndrome untreated can rise the mortality rate of the patients up to a 71%[5]. There are asymptomatic cases whose expected 10-year mortality is approximately of a 50%[6]. An appropriate treatment can reduce the mortality rate to a 0.3%[5]. Beta-blockers in combination with sodium channel blockers such as mexiletine, lidocaine, flecainide and ranolazine are indicated in patients whose QTc shows values over 500 ms,[7–9]. However, there is some concern for LQTS type 3 patients when also presenting features belonging to conduction defect or Brugada syndrome. In these cases, high temperature or administration of flecainide was able to reveal the presence of the other phenotypes, and even trigger life-threatening arrhythmias[10,11]. Study of the drug-channel interaction of the beforementioned drugs has shown that they are complex and not restricted to blocking either the fast (I_{Naf}) or the late (I_{NaL}) components of the sodium current. Study of these interactions may provide a deeper understanding of the effectiveness of these drugs. Mathematical models of the ion channels can help to study ion channel-drug interactions in detail, and models of the human action potential allow the study of the impact of those in the cardiac ventricular cell's function.

Genetic mutations are not the only cause of LQTS and TdP. In fact, in a retrospective study in a German hospital, it was found that there was an incidence of 2.5 per million males and 4 per million females with drug induced QT interval prolongation per year[12]. The exposure to QT prolonging drugs provoked drug-induced LQTS in 6.3% and TdP in 0.33% of the patients[13]. Naturally, the combination of both QT prolonging drugs and genetic mutations increases the risk of suffering drug-induced prolongation of the QT-interval. The International Harmonization Conference (ICH) published the current guidelines to ensure new drugs would not prolong the QT interval[14,15]. However, this came at a high cost due to the low specificity of the test that was being used, which could prevent useful drugs from reaching the market[16]. International efforts are currently being made to generate new guidelines that improve the arrhythmogenesis prediction. The Comprehensive in vitro-in vivo Proarrhythmia Assay (CiPA)[17] leads the efforts by providing new guidelines to help adopt a new paradigm of drug safety. Importantly, this will be done by integrating information from different sources, which include not only clinical and experimental data, but also in silico data. Therefore, mathematical models, including those of the human ion channels and action potential, represent a fundamental tool to test the effects of drugs[17].

Therefore, there are two main scenarios that would benefit from the use of mathematical models of the human ion channels and action potential, namely, to either select the best treatment for a particular LQTS syndrome or to improve the detection of potentially arrhythmogenic compounds before they reach the later stages of drug development.

Therefore, in this PhD thesis we will be exploring the use of electrophysiological models of the human cardiac ion channels and action potential both in the detection of potentially arrhythmogenic compounds and the study of the effectiveness of drugs in the LQTS.

1.2 Objectives

The main objective of this PhD thesis is to predict the effects of drugs on cardiac electrophysiology using computational modeling and simulation. This PhD thesis focusses on two relevant aspects where cardiac modeling is becoming more important, namely, the study of drug safety and efficacy. On the one hand, drug cardiotoxicity, which is the possibility of drugs provoking arrhythmia, is a key challenge for drug development. On the other hand, personalized medicine can improve the therapies of patients with cardiac

abnormalities, such as long QT syndrome. Therefore, this thesis was divided into two main chapters with the following objectives:

1. To develop an easy-to-use tool based on cardiac electrophysiological models to detect potentially arrhythmogenic drugs in the early stages of drug development.
    - To generate matrices with the results of the simulations of the effects of blocking relevant membrane ionic currents.
    - To create a prediction tool using a large number of drugs with known risk and the results of the simulations.
    - To evaluate the performance of the tool.
2. To provide evidence for an alternative treatment to flecainide for long QT syndrome SCN5A V411M patients when its use is not indicated.
    - To model the SCN5A V411M mutation reproducing its dynamics.
    - To simulate the effects of flecainide and ranolazine on cardiac electrophysiology.
    - To provide an explanation of the beneficial effects of flecainide on SCN5A V411M patients. To test a possible alternative treatment for SCN5A V411M patients with the drug ranolazine.

-

Chapter 2. State of the Art

2.1 The heart

The heart is at the core of the circulatory system, in the middle of the thoracic cage, between the lungs and covered in a protective epithelium called the pericardium. Its function is to keep blood flowing constantly eighty times a minute on average, powering the organism's transportation system for oxygen and nutrients, among others. To do so, the heart is made of mainly three types of tissue, namely, atrial, ventricular, and conductive muscle. Much like skeletal muscle cells, ventricular and atrial cells contract and, by doing so, they shrink their size pulling from each other. In turn, this reduces the volume of the cavities that lie inside the heart, propelling the blood they contain into the arteries and powering blood flow.

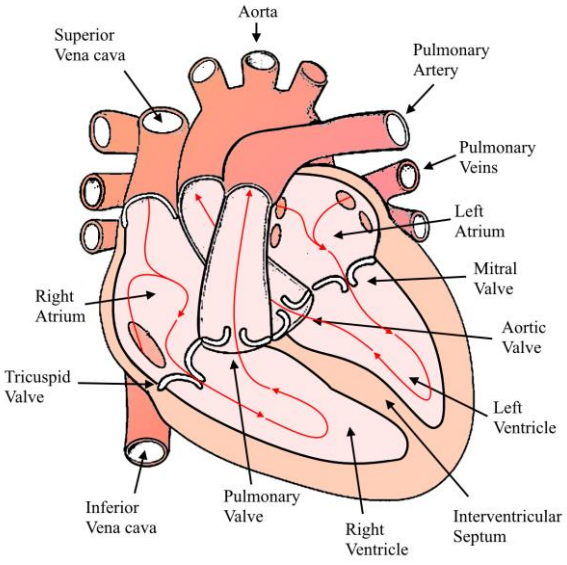

Figure 1. A**natomical representation of the human Heart.** Frontal section of the four chambers, main arteries and valves that allow the heart to pump blood in the direction indicated by the red arrows.

Figure 1 shows the main anatomical features of the heart. It contains four chambers, two atria and two ventricles. The latter are separated by the interventricular septum. The heart can be viewed as two independent pumps that feed into two distinct circulatory sub-systems. The left side of the heart pumps blood to all organs excluding the lungs, which are connected to the right

side of the heart. Red arrows indicate the path that blood follows during a heartbeat. Starting from the right side of the heart, deoxygenated blood is collected from the organs by both cava veins and funneled into the right atrium. In a first, weaker, contraction, it pushes blood into the right ventricle and, shortly after, the ventricle contracts funneling blood to the pulmonary arteries. Then, blood gets oxygenated before being collected by the pulmonary veins into the left atrium. There, it is pumped into the left ventricle, which strongly contracts to pump the blood into the aorta artery, feeding the rest of the organism and finally closing the cycle. Valves prevent blood from going backwards between atria and ventricles and between ventricles and arteries. The tricuspid valve lies between the left right atrium and right ventricle, while the mitral valve is its left side's counterpart. The pulmonary valve is placed between the pulmonary arteries and the right ventricle, while the aortic valve separates the left ventricle from the aorta.

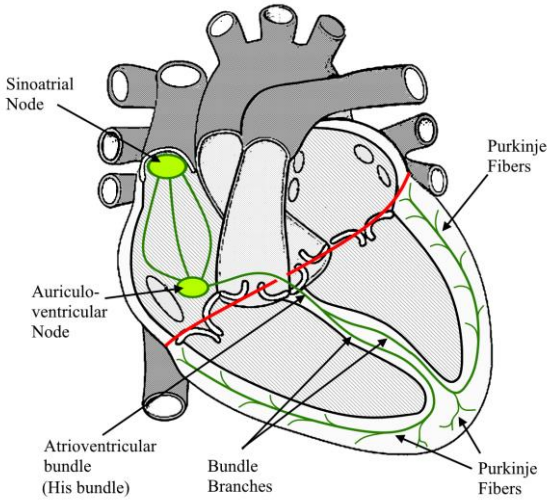

Figure 2. Cardiac conduction system. Representation of the main structures of the cardiac conduction system. Filled circles represent the position of the nodes. Dark green lines show the paths that signals arising from the nodes follow to fully stimulate the cardiac tissue. A red line symbolizes the electrophysiological separation of atria and ventricles.

This cycle ensures the organs receive a constant supply of nutritious oxygenated blood, but it would not be possible without the heart's conduction

system, as depicted by Figure 2. Every beat starts when a spontaneous signal is generated at the sinus node (top green circle), a bundle of self-excitable cells. This signal quickly propagates through the atria, triggering their contraction, but a layer of non-conducing fibrous tissue between atria and ventricles prevents the signal from reaching the latter. Instead, it reaches the auriculo-ventricular bundle, a slow-conducing tissue that guarantees enough time for the blood in the atria to be pumped into the ventricles. From there, the signal travels through a high conduction tissue consisting of first the His bundle and then the Purkinje fibers, which quickly spread it to the whole ventricular tissue so that it contracts synchronously. The period of contraction is called systole, while the period of relaxation where blood comes into the atria is called diastole[18–20].

2.2 The cardiac tissue.

Cardiomyocytes are the cells that form the cardiac muscle. There are three main types of cardiomyocytes, namely, nodal, working, and conductive. However, in this PhD thesis we will be focusing mainly on working cells. Figure 3, panel A, represents a cardiomyocyte inside a small section of the cardiac tissue. Much like other cells, a cardiomyocyte consists of a lipid bi-layer membrane enveloping a myoplasm (cytoplasm of a muscle cell) that contains the nucleus and common organelles that are necessary to maintain its function. The main feature of muscle cells is the large amount of actin-myosin fibers, responsible for their contractility, which occupy almost the entire myoplasm. As depicted by panel C, the fibers are surrounded with a special compartment called the sarcoplasmic reticulum. It forms a complex network that has the sole purpose of storing calcium ions and releasing them on demand. The cardiomyocyte's membrane has T-tubules, which are extensions that penetrate deep into its myoplasm and stay in close contact with the sarcoplasmic reticulum, vastly increasing its surface area[18].

Cells are tightly interconnected in the cardiac tissue, and muscle fibers are oriented in a specific direction. As described by Figure 3, panel B, special proteic pores called gap junctions create openings between cell myoplasms. These junctions provide a very low resistance channel for ion, molecule and even protein fluxes. In the cardiac tissue, they are especially abundant in the longitudinal direction of the cell. Ionic variations in one cell can be reflected in neighboring cells due to this exceptional interconnectivity[21]. There are other cell types in the cardiac tissue, such as fibroblasts and stem cells, which do not possess the same properties as the cardiomyocytes and instead show their role

not only as structural, regenerative, cells but also in specific diseases. The extracellular matrix surrounding the cells contains the extracellular fluid as well as proteins, mainly collagen, which is produced by fibroblasts. There is a remarkable ion concentration difference between the interior and exterior of the cells. Indeed, sodium ions tend to accumulate outside the membrane at a concentration of around 140 mM while remaining at a low 5-8 mM in the myoplasm. Contrarily, potassium ions tend to accumulate interior of the cells at around 155 mM while concentrations in the external medium stay around 5.4 mM.

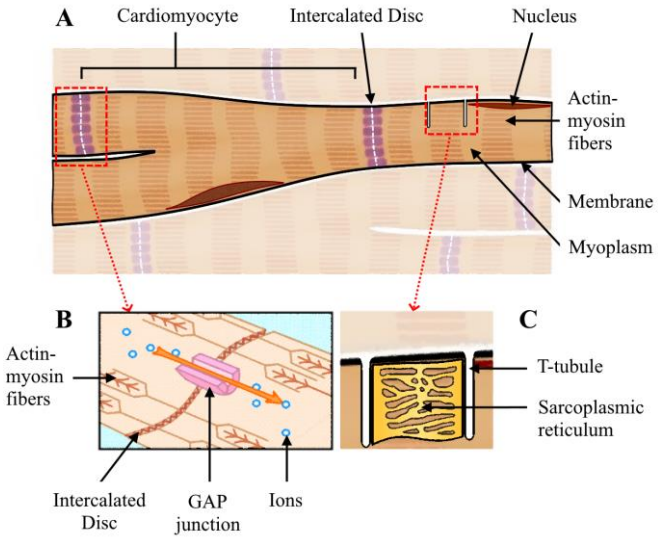

Figure 3. Representation of a cardiomyocyte. A) Representation of the cardiac tissue. A row of interconnected cardiomyocytes (working) has been highlighted. **B)** Diagram of a gap junction connecting two cardiomyocytes at the intercalated discs. Ions in solution were represented as blue circles. The orange arrow indicates ion flow, although it is not restricted to the sense that is shown. **C)** Sarcoplasmic reticulum, not shown in A for the sake of clarity, surrounds the actin-myosin fibers and T-tubules in the shape of a network. Note that features are not to scale.

The cardiac tissue contains several types of cardiomyocytes that slightly but importantly differ in their response to a stimulus. While at least 9 different

zones have been identified in the atrial tissue[22], the ventricles' tissue has been classified in four main types: working cells forming the endocardium, midmyocardium and epicardium, and specialized conductive cells forming the Purkinje system[19]. Epicardial cells form the outermost layer of the ventricular wall while endocardial cells form the internal side. Midmyocardial cells are found deep in the subepicardial to myocardial regions of the ventricular free wall, as well as in subendocardial layers both in trabeculae, papillary muscles, and septum. The differences of such cell types have been documented in a wide range of mammalians including humans. However, the limits of those layers are still diffuse as the nature and interconnectivity of the cardiac tissue normalizes the cell's electrophysiological characteristics, which are clearly defined *in vitro* but not *in vivo*[23]. In fact, there are numerous confusing factors when determining the midmyocardial tissue since its location, its thickness and its distribution can vary between preparations even from the same cardiac region. This is a strong argument supporting the controversy that surrounds the role of midmyocardial cells. While their existence is difficult to refute and their particular electrophysiology is known, the inability to identify them in intact coupled cardiac tissue in a reliable way keeps the community from agreeing on their definition[24–27].

Nevertheless, the fact that there are important electrophysiological differences throughout the ventricular wall has been widely demonstrated, including different response to drugs and their role amplifying the transmural electrophysiological heterogeneity of the tissue in pathological conditions[24–27].

2.2.1 Ion channels

Cardiomyocytes are excitable cells that can respond to stimuli by producing a fast depolarization of their membrane. This depolarization represents the "signal" that is able to propagate making use of the cardiac tissue's special properties. It occurs when sodium ions from the extracellular medium rush into the cell's myoplasm through special proteins called ion channels. These are special transmembrane proteins that are permeable to certain ions, mainly to sodium, calcium and potassium. Importantly, there are several channel types that not only differ in their specificity towards the ion, but also in their energy requirements and operation modes.

As for energy consumption, ion channels can be passive, where ion flow happens in the same sense as a concentration gradient – from high to low concentration – or active, where a source of energy, normally ATP, is used to catalyze the ion transport across the membrane.

Ion channels can be permeable to one or more ions. Some channels can profit from the gradient of one ion to provide the required energy to move other ions in the opposite direction. This is the case of the sodium-calcium exchanger, which is one of the main calcium regulators in the cardiac cells and responsible for exchanging three sodium cations from the extracellular medium for one calcium cation in the myoplasm[28]. However, the sodium-calcium exchanger can be reverted provided the electrochemical conditions are met. Contrarily, the sodium-potassium pump is the perfect example of an energy mediated ion exchange. Its function is to exchange one potassium ion from the intracellular medium for one sodium ion from the extracellular medium. To enable this counter gradient ion flow, it consumes an ATP molecule for every operation[29]. The energy investment is nonetheless worth it since the sodium-potassium pump maintains the sodium and potassium gradients that are essential for the cardiomyocytes and the main driver of their function.

The flow of ions through ion channels constitutes a current due to the movement of charged particles. The following list describes the ion currents and fluxes that mainly contribute to the cardiomyocyte function as a contractile cell.

- Potassium currents
    - I_{Kr}: rapid component of the delayed rectifier potassium current, I_K.
    - I_{Ks}: slow component of the delayed rectifier potassium current, I_K.
    - I_{K1}: inward rectifier potassium current.
    - I_{tof}: fast component of the transient outward potassium current, I_{to}.
    - I_{tos}: slow component of the transient outward potassium current, I_{to}.
    - I_{Kur}: ultrarapid delayed rectifier potassium current.
    - $I_{K\text{-}ATP}$: ATP activated potassium current.
    - $I_{K\text{-}ach}$: muscarinic gated potassium current.
    - I_{Kp}: plateau potassium current.
- Sodium currents
    - I_{Naf}: fast component of the sodium current, I_{Na}.
    - I_{NaL}: late component of the sodium current, I_{Na}.
    - I_b; background sodium current.
- Calcium currents
    - I_{CaL}: L-type calcium current
    - I_{CaT}: T-type calcium current

- Ion fluxes
    - J_{up}: calcium uptake from the myoplasm to the sarcoplasmic reticulum by the SERCA pump.
    - J_{rel}: calcium release from the sarcoplasmic reticulum to the myoplasm by the RyR channel.

Table 1. List of the genes that code for ion channels. The first column indicates the current that flows through the protein that is coded the gene on the second column. Data from Roden and Kuperschmidt[30].

Current name	Gene name
I_{Kr}	hERG
I_{Ks}	KvLQT1/minK
I_{Kur}	Kv1.5
I_{K1}	Kir2.1
$I_{K\text{-}ach}$	Kir3.1/Kir3.4
$I_{K\text{-}ATP}$	Kir6.1/2
I_{to}	Kv4.3
I_{Na}	SCN5A
I_{CaL}	α_1C
I_{CaT}	α_1H

Throughout this PhD thesis we will be frequently referencing several ion channels from their current names. For example, the I_{Kr} channel would represent the protein through which flow potassium ions whose current is called I_{Kr}. Proteins, and therefore ion channels, are transcribed and translated from genes. Sometimes we could reference an ion channel by its gene name. For example, the gene that codes the ion channel responsible for I_{Kr} is the human ether-à-gogo related gene, or hERG for short. Therefore, some sources could refer to it as the hERG channel instead. Another important gene throughout this work is the SCN5A gene, which codes for the α-subunit of the sodium channel. Table 1 shows a list of the genes that code for some of the main currents.

To review the structure and function of the ion channels, we will take on the example of the sodium channel, since it is a particularly important channel in this work. As its name suggests, the sodium channel shows permeability to sodium cations in the cardiac tissue. The channel consists of several subunits, but only the main α subunit is necessary to its function.

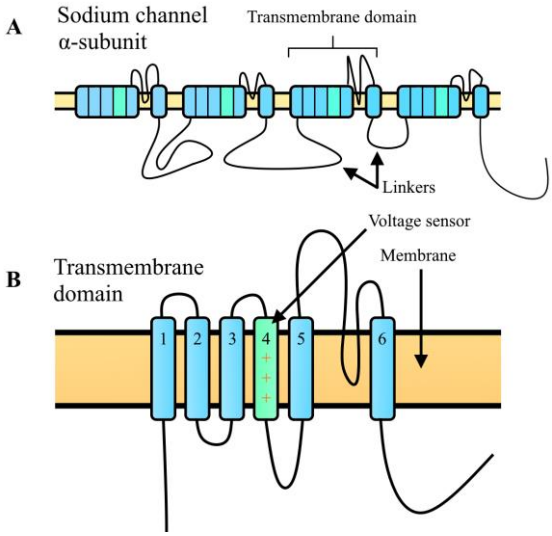

Figure 4. Representation of the unfolded proteic structure of the α-subunit of a human sodium channel. A) Unfolded complete structure of the sodium channel showing four transmembrane domains connected with linkers responsible for the gating properties of the channel. B) Representation of a single transmembrane domain showing its six segments. The fourth one contains a high concentration of positively charged residues, making it slide during voltage changes between the exterior (up) and interior (down) of the cardiomyocyte.

Figure 4, panel A, depicts the extended structure of the α subunit, which contains four identical interconnected domains (panel B) that fold together creating a central pore through which sodium ions can passively diffuse. Every domain consists of six segments (named 1 to 6 in panel B) of which the fourth (green) contains many positively charged residues, giving it voltage-sensing capabilities. Indeed, these can make the segment slide in (downwards) and out (upwards) of the membrane, changing the protein's conformation in the process, which triggers modifications of linker positions leading to important alterations in the channel's conductance[31]. Gating, or the ability to open or close depending on an external stimulus, is indeed a fundamental property of

the ion channels. The sodium channel is therefore a voltage-gated ion channel whose conductance can be regulated by changes in membrane potential. Of note, the α-subunit is accompanied by two auxiliary β subunits (β1 and β2, not shown) that importantly modulate the channel's function, increasing its conductance, altering its gating properties, or even altering the membrane's capacitance[21,32]. However these are not fundamental to the channel's main function,

2.2.2 The action potential

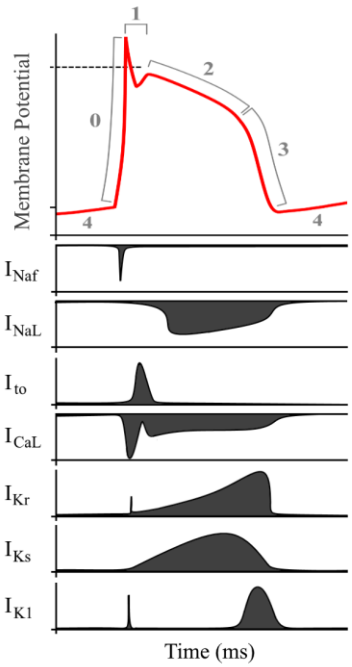

Figure 5. Time course of the major membrane currents that contribute to the time course of the action potential. Top panel illustrates the time course of the action potential during one beat. The remaining panels show the approximate time course of the major currents that contribute to it. Depolarizing currents are negative by convention. The area under the curve of every current has been filled for the sake of clarity. Currents are not to scale.

During a heartbeat, cardiomyocytes contract synchronously owing to a cycle of depolarization and repolarization of their membrane, a process known as the action potential (AP). By convention, the internal portion of the membrane is negatively charged at resting state, which can be assessed by a pair of

microelectrodes, one of them being inserted in the cardiomyocyte's cytoplasm and the other one being in the external medium.

Figure 5 illustrates the time course of an action potential during one heartbeat, along with the time courses of the main currents that take part in its formation. There are five phases to the action potential, starting with phase 4, where the cell is in equilibrium and the membrane potential stays around -80 to -90 mV. This is due to the presence I_{K1}, which are partially compensated by the sodium background current, and maintained by the potassium and sodium gradients generated by I_{NaK}.

Phase 0 is mainly driven by I_{Naf}. A small depolarization of the membrane is enough to trigger the opening of the sodium channels, enabling sodium ions to rush into the cell due to concentration gradient that exists between the intracellular and extracellular mediums. This further elevates the membrane potential, causing the opening of more sodium channels. Through this positive feedback loop, all sodium channels quickly open culminating in an extremely fast (around 2 ms) depolarization of the membrane to positive potentials. Then, the channels quickly close taking the depolarization to an end. Phase 1 starts with a small repolarization due to I_{to} activation, an outward current which partially counters the effects of I_{Naf}. While its peak is strong during this phase, I_{to} will inactivate after around 100 ms. Phase 2, also called the plateau phase, is by far the longest phase in cardiac ventricular cells, lasting around 200 to 400 ms. It is characterized by the opening of calcium and sodium channels, (I_{CaL} and I_{NaL}) and their depolarizing effects are compensated by the repolarizing effects of the potassium rectifier currents I_{Kr} and I_{Ks}[33]. Consequently, the membrane potential stays quite stable during this phase, a feature that is necessary to ensure a proper contraction of the cell. Like other muscle cells, ventricular cells need calcium in the sarcoplasmic reticulum to be released through the RyR channels. In resting conditions, there is almost no calcium in the myoplasm due to the activity of the SERCA pump (J_{up}), which brings it all into the sarcoplasmic reticulum, but, as I_{CaL} activates, a calcium induced-calcium release mechanism floods the cell with calcium, multiplying its concentration by a thousand times[34], which triggers the contraction of muscle fibers by exposing the actin-myosin binding site. Finally, phase 3 consists of a repolarization mainly driven by the potassium rectifier currents (I_{Kr} and I_{Ks}), now supported by the activation of I_{K1} and the inactivation of I_{CaL}, bringing the membrane potential to its initial resting state[33] and allowing the calcium to be imported to the sarcoplasmic reticulum in preparation for the next contraction.

An important property that is directly inherited from the sodium channel dynamics is refractoriness. An action potential can be triggered by an increase in membrane potential due to current injection (stimulus). However, the action potential cannot be triggered at any moment. There is an absolute refractory time window that begins after the start of an action potential and ends during late phase 2 where no new action potential will result from a stimulus. A relative refractory period consists of an additional time frame where action potentials can be triggered, albeit in response to stimulus of greater amplitude.

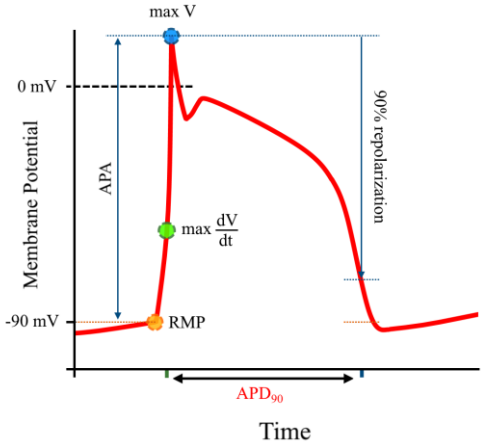

Figure 6. Graphical representation of the main biomarkers used to characterize the action potential.

Biomarkers that are typically used to characterize the action potential's morphology include the resting membrane potential (RMP), action potential duration (APD), action potential amplitude (APA), upstroke velocity (max dV/dt) and triangulation (see Figure 6). The most common measurement of APD is the one that is registered at 90% repolarization of the membrane voltage (APD_{90}), but this value can be assessed for any percent repolarization. In fact, triangulation can be calculating by subtracting the APD_{50} to the APD_{90} values.

The action potential time course is heavily dependent on pacing frequency (in Hertz) and its inverse value, the basic cycle length (BCL) which is the time interval in milliseconds between two consecutive stimuli. The former is a

measure of the number of stimuli that are applied in one second, while the latter indicates the time interval between stimuli. The electrophysiological differences between tissue types play an important role both during healthy and altered cardiac function.

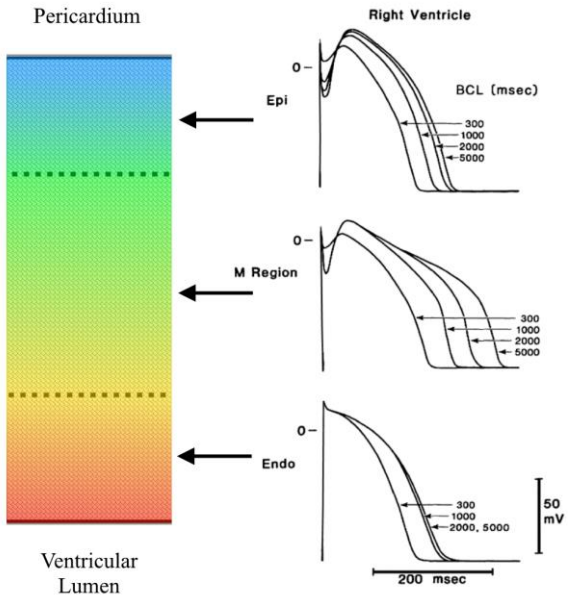

Figure 7. Action potentials from selected cells of the canine ventricular wall. Left panel symbolizes the ventricular wall and dashed lines represent the limits of the regions, whose exact position varies considerably between species, individuals, and preparations. The right panel was modified from Sicouri and Antzelevitch[35], and shows superimposed action potentials recorded at several BCLs from cells belonging to the indicated regions.

Figure 7 depicts the main features of representative action potentials from three cell types at several pacing rates. The left panel represents a transmural section of the ventricle where the main electrophysiological regions are delimited by dashed lines. Sample action potentials from epicardial (Epi), midmyocardial (M region) and endocardial (Endo) cells have been represented in the right panel at several BCLs. Colors remind of the interconnected properties of the cardiac tissue and show that the action potentials usually transition gradually

from one end to the other of the ventricular wall. The action potential duration is the first prominent difference that can be observed. Epicardial cells show the shortest action potentials, followed by endocardial and midmyocardial cells, which show the longest. These arise from changes in current densities as, for example, midmyocardial cells show a very small I_{Ks} and a larger I_{NaL} of almost twice that of the epicardial cells[24]. The presence of a notch following phase 0 (depolarization), also called spike-and-dome-morphology, which arises from the presence of a larger I_{to} that contributes to the phase 1 repolarization (see 2.2.1[24]), is characteristic of the midmyocardial and endocardial, but not epicardial, cells. The APD rate adaptation shows also differences between cell types, consisting of steeper curves in Purkinje and midmyocardial cells compared to endocardial and epicardial cells[36], as depicted by the greater AP differences in midmyocardial cells in Figure 7.

In healthy conditions, the midmyocardium would largely contribute to the cardiac contraction strength[37], followed by the endocardium and epicardium, while Purkinje cells are specifically in charge of stimulus conduction and delivery to strategic locations in the endocardium. As mentioned in 2.2.1, the electrophysiological differences of the cells get softened by the electrochemical coupling between cells in the cardiac tissue, averaging the APD differences[23], so much that sometimes it is difficult to identify the cells directly on the cardiac tissue as we reviewed in 2.2.

2.2.3 The electrocardiogram

In previous section we explored the evolution of the membrane voltage that cardiomyocytes experience during the action potential. While small, these fluctuations in voltage can add up to create an important voltage difference between adjacent regions in the heart. The depolarization wave propagation generates a dipole that induces a variable electric field through the human body. This dipole can be measured by connecting a pair of electrodes to the skin. However, the cardiac vector, whose direction gets determined by the position of the negative and positive charges, may not be aligned with the position of the electrodes, which is usually the case. Therefore, measured potential differences are a projection of the real cardiac vector on the imaginary vector formed by the electrodes. Consequently, a need to define standardized positions for electrodes appeared. Nine standard positions were defined by 1938 (I, II, III, V1, V2, V3, V4, V5 and V6). Three unipolar leads (aVR, aVL, aVF) were included later adding up to a total of twelve measuring locations which form the current electrocardiogram (ECG).

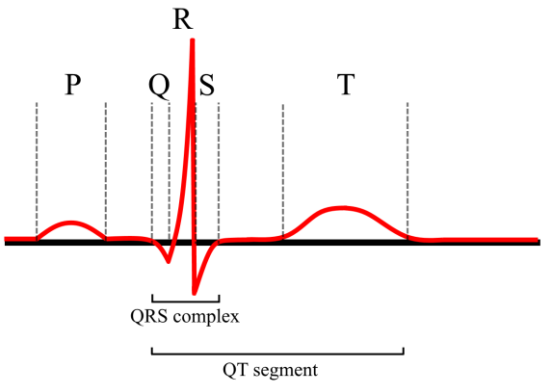

Figure 8. Time course of the typical ECG in humans. Illustration of a typical lead II electrocardiogram. Note that the time course of the electric field is substantially different between derivations.

Figure 8 shows a typical ECG time course. Briefly, there are up to 5 common waves. The first, P, is a small wave corresponding to the depolarization of the atria. It is followed by a triple wave complex starting with a small decrement (Q wave) that precedes a fast peak that swings up (R wave) and then down to another slightly greater depression (S wave) that goes back to the resting value. The latter is called the QRS complex and corresponds to the depolarization of the ventricles, although it might not always show as a triplet. The left ventricle is responsible for a major part of this complex because of its greater size. The interval between the P and Q waves gives information about conduction through the auriculoventricular node and widening of the QRS complex is usually related to ventricles that take longer to depolarize, indicating a reduction in conduction speed in the cardiac tissue. A short inactive period corresponding to the plateau phase of the action potentials in the tissue is then followed by a wide, albeit low, wave matching the repolarization of the ventricles (the T wave). Atrial repolarization happens during the QRS complex. However, due to the greater amplitude of the signals coming from ventricular repolarization, it cannot be observed. The QT segment, or QT interval, is defined as the interval between the beginning of the Q wave and the end of the T wave and is related to the time it takes for the ventricles to perform an entire depolarization-repolarization cycle. The R to R interval can be used to assess heart rate. Many cardiovascular diseases can be detected by monitoring the ECG of a patient, such as myocardial infarction, hypertension, ischemia, or myocardial neuropathy, due to the alterations they provoke on ECG parameters[38,39].

2.3 Cardiac Disease

Cardiovascular disease remains the most prevalent disease worldwide with more than 150 million people suffering from it[40], claiming approximately the same number of lives as cancer. In US alone, the estimated heart disease cost only in 2008 was of 448 billion USD. Due to the mechanical nature of the heart, cardiac disease is complex and multifaceted[41], as electrophysiological alterations can produce cardiac dysfunction without leaving visible modifications of the tissue.

2.3.1 Cardiac structural disease

Heart disease shows in a variety of causes that can lead to arrhythmia or heart failure. Obesity is tightly related to coronary artery disease, which is a consequence of atherosclerosis, a condition where vascular lesions get progressively thickened when a combination of lipid absorption, cell division and leukocyte aggregation tries to repair the damage[42,43]. These lesions are especially dangerous in essential vascular regions such as coronary arteries, which irrigate the cardiac tissue itself. Eventually, plaque detachment, coronary spasm, or even during a sudden effort requirement, blood flow can be severely restricted preventing the ventricular tissue from getting oxygen, consequently provoking angina and, in prolonged episodes, myocardial infarction[44].

Reactivation of the blood flow can mitigate the damage to the tissue to a certain degree, although the characteristics of the affected area can never be recovered. The stiffness of the tissue that grows to heal the damage, combined with its reduced electrical conduction properties, represents a continuous lag to the cardiac function. The ventricle tends to dilate and remodel to compensate for the lack of contractile power. Remodeling of the cardiac tissue is caused by increased stress with constant cellular death and regeneration, and leads to reordering, hypertrophy and elongation of the cardiomyocytes, accumulation of inflammatory molecules and increased interstitial fibrosis induction, among others. These changes are beneficial for the heart's function. However, the scar's fibroblasts couple to healthy cardiomyocytes leading to deeper alterations of their electrophysiological properties[45,46]. Therefore, cardiac structural disease, consisting of presence of scar tissue and cardiac remodeling, represents a perfect substrate for arrhythmia to trigger.

2.3.2 Long QT syndrome (LQTS)

LQTS patients show characteristic elongated QT segments of the ECG not related to structural cardiac defects. The causes of this elongation lie in

electrical abnormalities of the cardiac electrophysiology, which can be caused by mutations or external factors such as ion channel blocking drugs. Elongated QT segments have been linked to arrhythmia (see 2.4), which is why health institutions, researchers, regulators, and pharmaceuticals have shown great interest in developing methods for the early detection of drugs capable of inducing LQTS, as well as treatments for this condition. Detailed information necessary to understand relevant aspects of the LQTS from the drug safety perspective can be found in Chapter 2, and from the drug efficacy perspective in Chapter 3 of this PhD thesis.

2.4 Arrhythmia and Torsade-de-pointes

Arrhythmias are altered heart rates originated in an abnormal electrical behavior in the heart. They have been classified in tachyarrhythmias and bradyarrhythmias according to heart rate. The former is diagnosed when the patient heart reaches more than 100 beats per minute and the latter with less than 60 beats per minute. According to the anatomical and electrophysiological barrier that exists between atria and ventricles, arrhythmias that develop in the atria are classified as supraventricular while the rest are ventricular. Tachyarrhythmias can start from the development of electrical activity in an abnormal region of the cardiac tissue. If correctly timed, this ectopic activity can trigger the conduction of the electric signal in a non-physiological, even inverse, path that could confront the normal depolarization wave. This could lead, for example, to extra beats, ventricular contractions that are reflected in QRS complexes in the ECG that are not preceded by a P wave (which is produced by the atrial depolarization), but also to sustained tachyarrhythmias, which involve perpetuation of the abnormal depolarization of the heart by completely overriding the sinoatrial signal. One of the possible explanations behind atrial fibrillation is the existence of rotating depolarizing fronts – rotors for short – that can be triggered by ectopic activity, or circulation of the signal around fibrotic anatomical structures such as veins, arteries, or scars. Torsade-de-pointes (TdP) is a particularly dangerous polymorphic ventricular tachyarrhythmia characterized by a series of QRS complexes that appear to twist around the electrical baseline. Its subjacent mechanism is still not well understood but, among its causes, it has strongly been associated to prolonged QT segments in the ECG which can lead to early after depolarizations and/or delayed after depolarizations[39,47–49]. These can be induced by some drugs, particularly antiarrhythmic drugs, but also by inherited electrical abnormalities in the cardiac conduction system caused by gene mutations. The following phenomena are known to take part in the initiation of arrhythmias:

- EADs, or early after depolarizations, are premature depolarizations that occur during the repolarization phase. In normal conditions, sodium channels recover from refractoriness not long after the potential reaches its resting membrane value. Delayed repolarization involves a membrane potential that stays at a higher value during abnormally long durations, extending the plateau phase of the AP. Under these conditions, sodium channels could reopen as they recover towards the end of this phase, triggering new depolarizations. Drugs or mutations can induce delays in repolarization by reducing the amplitude of repolarizing currents such as I_{Kr}[48,50] or increasing depolarizing current such as INaL[51,52]. These sudden depolarizations can propagate through the cardiac tissue, a phenomenon that is called triggered activity[39,47].
- DADs, or delayed after depolarizations, are abnormal depolarizations similar to EADs but are triggered by completely different mechanisms. DADs typically result from sudden calcium release events from the sarcoplasmic reticulum in conditions of calcium overload promoted by increased APD_{90} or QT[39,47] intervals. Since DADs occur after a complete repolarization, they can trigger a new action potential provided they reach the depolarization threshold, which can also propagate through the cardiac tissue.
- Conduction slowness: drugs that block I_{Naf}, the fast component of the sodium current, not only reduce the upstroke velocity but also the conduction velocity, the speed at which the depolarization wave front propagates through the tissue, which can lead to arrhythmia as revealed by the CAST trial[53]. This is particularly dangerous in cardiac structural disease (scars), where functional and electrophysiological properties of the affected zone differ from the surrounding tissue. Scars themselves provide conduction slowness in the interface between healthy and fibrotic tissue (the border zone). They also may generate channels of slow conduction at their core consisting of surviving cardiomyocyte bundles, which creates the perfect substrate for arrhythmia[54]. When the wave front leaves the slow conduction area, it may enter a recently repolarized tissue ready for a new depolarization. This represents the origin of abnormal propagation, which can perpetuate itself by circulating through or around the scar again.

2.5 Antiarrhythmic therapy

The goal of dispensing drugs to patients suffering arrhythmias is naturally to terminate the arrhythmic activity while preventing the appearance of new episodes. Unfortunately, antiarrhythmics are known to be both the solution and the cause of arrhythmias. Antiarrhythmic drugs interact with ion channels, either enhancing or reducing their permeability (conductance) to ions, which in-turn produces changes in the time course of the action potential. This could potentially counter the alterations caused by subjacent abnormalities. However, it may as well induce electrical abnormalities by prolonging the APD_{90} and thus promoting EAD formation as we reviewed in a previous section.

Antiarrhythmics have been assigned a class from I to IV according to the Vaughan Williams classification[55], which is based on the molecular target of the drug. The fact that there are numerous drugs that target multiple channels constitutes the reason why there have been many attempts at creating other classifications, however the most widely used is the abovementioned one. Briefly, Vaughan Williams classes include sodium channel blockers in class I (with sub-classes a, b and c), beta adrenoreceptor blockers in class II, APD prolongers in class III and calcium channel blockers in class IV.

2.5.1 Class I: sodium channel blockers.

Sodium channel blockers can affect the fast or the late component of the sodium current. Class Ia drugs include compounds that block I_{Naf} and therefore reduce the upstroke velocity of the action potential's phase 0, reducing conduction velocity in the cardiac tissue. At the same time, they show affinity for I_{Kr} channels thus reducing repolarization and prolonging the APD, which induces a QT segment prolongation. Examples of class Ia drugs include disopyramide and quinidine. Class Ib comprises drugs that have a minimal effect on phase 0 and instead shorten the APD by means of I_{NaL} block, although high doses can produce I_{Naf} block-like side effects. Mexiletine and lidocaine are examples of these compounds. Class Ic contains drugs that show no effect on APD and strong effect on phase 0 of the action potential characterized by very slow dissociation dynamics, greatly reducing conduction velocity. Among the examples of these drugs, flecainide and encainide can be found.

2.5.2 Class II: β-blockers

β-stimulation increases I_{CaL}, calcium concentration in the sarcoplasmic reticulum, the magnitude of repolarizing potassium currents and the pacemaker activity in the cardiac tissue in order to shorten the APD while increasing contraction strength and heart rate. β-stimulation is associated to stressful

situations. Therefore, blocking β-receptors reduces heart rate, which leads to reduced oxygen demand during angina and prevents arrhythmia in some forms of the LQTS owing to less calcium overload of the sarcoplasmic reticulum, which reduces DAD generation. Some examples of these drugs include nadolol, sotalol and the widely used propranolol. Interestingly, the latter shows sodium channel block to some extent at high doses[39].

2.5.3 Class III: action potential prolongers.

Drugs belonging to this group generally display blocking effects on repolarizing potassium currents, such as I_{Kr} or I_{Ks}. The resulting prolongation of the APD and the QT segment can be antiarrhythmic by increasing refractoriness and therefore stopping the reentry of the wave front. Examples of pure potassium current blockers include dofetilide and ibutilide, while multi-channel blockers, such as amiodarone, dronedarone and quinidine, are also available. Sotalol has also shown β-blocker effects[39]. Recently, I_{Kr} block has been identified in many drugs that are not related to cardiac treatment, such as antimicrobial agents, antihistamines, antipsychotics, and others[56]. Since prolongation of the QT is also a surrogate biomarker for Torsade-de-pointes[48], these drugs are usually classified as dangerous[57].

2.5.4 Class IV: calcium channel blockers.

The effects of calcium channel blockers mainly rely on slowing heart rate, which are key to the nodal tissues. Reentrant arrhythmias that include the auriculoventricular node can be stopped using calcium these drugs. Ventricular arrhythmias initiated through triggered activity by DADs can be prevented as well[39]. Calcium currents are responsible for maintaining the action potential plateau (see Figure 5), therefore their block can contribute to reducing the APD. In fact, the apparent safety of some drugs that exert a strong block of potassium channels such as Verapamil could be explained by calcium channel block[58]. Other examples of drugs in this category include nifedipine, nitrendipine and diltiazem.

2.6 Modeling the cardiac electrophysiology

2.6.1 An introduction to cardiac modeling

Models are powerful tools in science that can provide useful information about the system they reproduce. They can be used to study and predict outcomes in many fields of knowledge, from weather forecast to airplane design. Models have indeed been able to predict the existence of phenomena before being experimentally observed, such is the case of the discovery of wave reentry in

cardiac tissue, which was first shown computationally[59] to later be found experimentally[60]. This is a formidable example of a great understanding of the principles that were modeled that proves the ability of computational models to provide insight into unknown mechanisms.

The modeler might approach the creation of a new model from several points of view depending on his needs. Statistical models are those that only seek to reproduce a phenomenon at a high level without delving into its subjacent properties, therefore their behavior is often compared to a black box. They need to be trained with datasets and seek to capture the trends of the data. The contrary of a top-down approach like the latter is a bottom-up approach, where the model seeks to study most basic units of a phenomenon to reproduce more macroscopic behaviors derived from them. These models are called mechanistic models and are optimized to reproduce certain dynamics with precision instead of relying on big datasets. One solution seeks to reduce complexity while the other seeks precision. In the end, all models have a combination of both approaches since they can be mechanistic at one level and black-box at another[61]. This is the case of most cardiac action potential models, where the ion currents combine to generate the action potential time course while the description of the current gates itself is statistic.

Electrophysiological models of the cardiac activity span multiple scales, from the ion channel to the whole body, including cell, tissue, and organ descriptions. One would think that switching scales would add-up an exponentially increasing amount of error from one level to the next. However, the field has matured enough that studies at the ion channel level can explain alterations at the body level, as demonstrated, for example, by Sadrieh and coworkers[62]. Consequently, cardiac electrophysiology modeling has proven its usefulness in many areas. It has been exceptionally successful in drug development[63] owing to the constantly increasing richness of its heritage[64]. In fact, the recent trend in safety pharmacology has acknowledged the need to create reliable models of the cardiac electrophysiology to test drug cardiotoxicity as an integral part of the drug development, and efforts are currently being made to refine them even more[17]. A number of projects have already elaborated their own biomarkers to try and assess the risk of cardiac arrythmias based on different parameters[48,58,65–68] with varied yet positive results. Beattie and coworkers[69] went further and included quantitative structure-activity relationship (QSAR) data to the mix, aiming to predicting the effect of a drug on an ion channel from its proteic and atomic structure. The ultimate goal of these tools is to assess the risk of arrhythmia of new compounds to reduce loss during drug development.

Cardiac electrophysiology models have shown success in other areas. A recent work from Martinez-Mateu and coworkers[22] showed using simulations the existence of phantom rotors in signal acquisition with atrial basket catheters, which could be hampering the determination of ablation procedures. On that note, a promising initiative seeks to help physicians to establish the minimal number and precise locations of the necessary ablations that can cancel atrial arrhythmias. For that matter, Boyle and coworkers[70] created personalized models of patients' hearts (through advanced imaging and segmentation) to simulate their specific atrial fibrillation. They determined the best locations for ablation and performed the interventions which resulted in no patient suffering from fibrillation again. This technology, despite being a proof-of-concept, shows the potential of cardiac electrophysiology models applied directly to human health.

2.6.2 Ion channel models

Ion channels compose the basis of all cardiac models. The combination of their dynamics leads to the formation of the action potential, the main driver of the cardiac contraction. Therefore, they are crucial during cardiac model development. In this section, the main mathematical descriptions that enable reproduction of ion currents, namely, the Hodgkin-Huxley and Markov chain formalisms, will be discussed in detail.

2.6.2.1 Hodgkin-Huxley formalism

The results of works from Hodgkin and Huxley in 1952[71] on the squid's giant axon paved the way for the scientific community and are still being used today[72]. In this section, we will be reviewing the most important conclusions of their work, which revolutionized the way of approaching ion channel and cell electrophysiology modeling. The Hodgkin-Huxley formalism considers the cell membrane and its ion channels as a simplified electronic circuit as described in Figure 9.

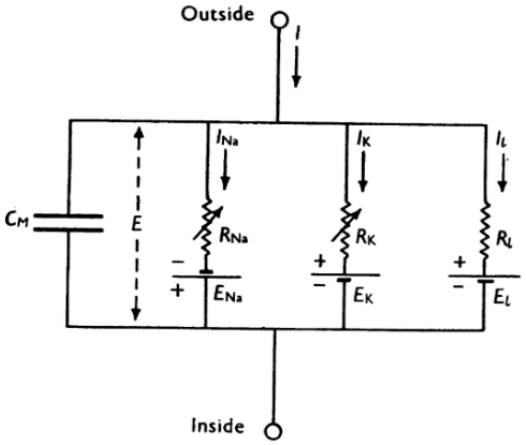

Figure 9. Electrical circuit representing the cellular membrane of a cardiomyocyte in the Hodgkin-Huxley formalism. The membrane possesses a capacitance (CM). Currents (I) can flow from one side to the other through channels represented as a generator (symbolizing the reversal potential) in series with a variable resistance (R), whose value depends on the membrane voltage (E), which is determined by ion concentrations on both sides of the membrane. Subscript indices specify the ion (K, Na, …, i). Figure modified from Hodgkin and Huxley (1952)[71].

C_M represents the membrane capacitance, E_i represents the reversal potential (or the tendency to cross the membrane) of a particular ion "i" (K^+, Na^+ or Ca^{2+}), and E represents the membrane potential. Every ion channel is included in the circuit as a variable resistor whose conductance "g" depends on E. Deduced from the Ohm's law, the current that flows through the whole membrane can be calculated as the addition of all currents that flow through each resistor across the membrane (see ***Eq. 1***).

$$\boldsymbol{I = C_m \cdot \frac{dV}{dt} + \sum G_i \cdot (V_m - E_i)} \qquad \textbf{\textit{Eq. 1}}$$

The term G_i represents the channel's conductance, which depends on the channel's gating properties. The membrane voltage was rewritten to V_m (previously named E) for the sake of clarity. Hodgkin and Huxley proposed a model where the channels would contain an appropriate number of independent gates, meaning their state does depend on other gates' states.

$$m \underset{\beta}{\overset{\alpha}{\leftrightarrows}} (1-m) \qquad \textit{Eq. 2}$$

The above model represents the two possible states of a gate "m", either open (m) or closed $(1-m)$. Switching between those states is governed by transition rates α (from the closed to the open state) and β (from the open to the closed state). Therefore, over time, the increment of the open state proportion can be written as

$$\frac{dm}{dt} = \alpha \cdot (1-m) - \beta \cdot m \qquad \textit{Eq. 3}$$

where α and β are voltage dependent. This equation can be rewritten as

$$\frac{dm}{dt} = \frac{m_{\infty} - m}{\tau} \qquad \textit{Eq. 4}$$

Where

$$m_{\infty} = \frac{\alpha}{\alpha+\beta} = \frac{1}{1+\frac{\beta}{\alpha}} \qquad \textit{Eq. 5}$$

And

$$\tau = \frac{1}{\alpha+\beta} \qquad \textit{Eq. 6}$$

From solving these equations, it can be deduced that, at any time t,

$$m(t) = m_{\infty} + \left(m_0 - m_{\infty}\right) \cdot e^{-\frac{t}{\tau}} \qquad \textit{Eq. 7}$$

In a channel population, the proportion of gates in the m state at time t (m_t) depends on the initial condition (m_0) and tends exponentially to the steady-state (m_∞) at a rate determined by the voltage dependent variable τ. A similar approach can be used for inactivation gates.

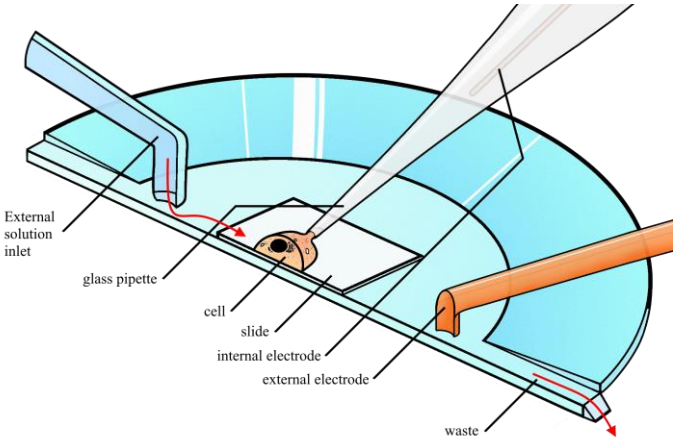

Figure 10. Manual whole-cell patch-clamp layout. The HEK293 cell transfected with the ion channel of interest is placed on a glass slide and its membrane sucked with a glass pipette to punch a hole in it after reaching giga seal conditions. External solution is constantly flowing in the sense of the red arrows. An electrode is placed inside the glass pipette for the internal medium while another electrode is placed in the extracellular medium. Both can be used to apply voltage and measure currents.

This formulation was used by Hodgkin and Huxley to optimally describe the potassium and sodium currents behaviors under controlled membrane potentials of a giant squid axon. This method is commonly known as voltage-clamp. It represents the most powerful technique to study ion channels and their dynamics. This is because of the ability to control the membrane potential of a cell, which is central to obtaining reliable results. Although there are many voltage-clamp versions[73], by far the most used configuration is the whole-cell patch-clamp[74].

As depicted by Figure 10, cells are carefully placed in a container filled with a solution of known ionic composition (external solution) where a microelectrode is also submerged. Then, a glass micropipette containing a solution that is similar to the cell's cytoplasm is carefully put in contact with the cell's membrane. Next, negative pressure is applied inside the pipette until it forms a very tight junction with the cell's membrane (a gigaseal). Finally, the membrane is slightly sucked into the pipette until it breaks, completing the whole-cell patch-clamp configuration. Here, the microelectrodes are in contact with two different milieus, the internal and the external solutions, separated by the cell's membrane, which contains the ion channel that is being studied[74].

To illustrate the procedures that are used and the results that can be obtained from whole-cell patch-clamp experiments, we will take on the example of the sodium channel.

Several gating properties have been identified, including activation, fast inactivation, and slow inactivation[31], key components of the sodium current's fast component. Fast and slow recovery from inactivation have also been identified. They play a key role in the refractoriness of the cardiac tissue and amplitude of the late sodium current. Other works have revealed the existence of two additional operation modes including "bursting" and "late scattered openings"[75,76], that are essential to the formation of the sodium current's slow component. Here, we will explore the fast activation and the inactivation dynamics since they provide a foundation that will facilitate the explanation of other more complex dynamics.

Activation and inactivation can be explained by the Hodgkin and Huxley formalism, who described activation as three "m" gates while inactivation was accurately described with only one "h" gate. Figure 11 represents the voltage dependent functions of m_∞ and h_∞, which are the steady state values of activation (panels B and D) and inactivation (panels A and C), respectively. To study sodium current dynamics, experimentalists apply a series of voltage commands to the cell's membrane designed to test the time course of the elicited current, which changes as a function of not only the applied potential but also depending on the duration and sequence of the commands. Activation is assessed by applying a series of pulses at test potentials (panel B).

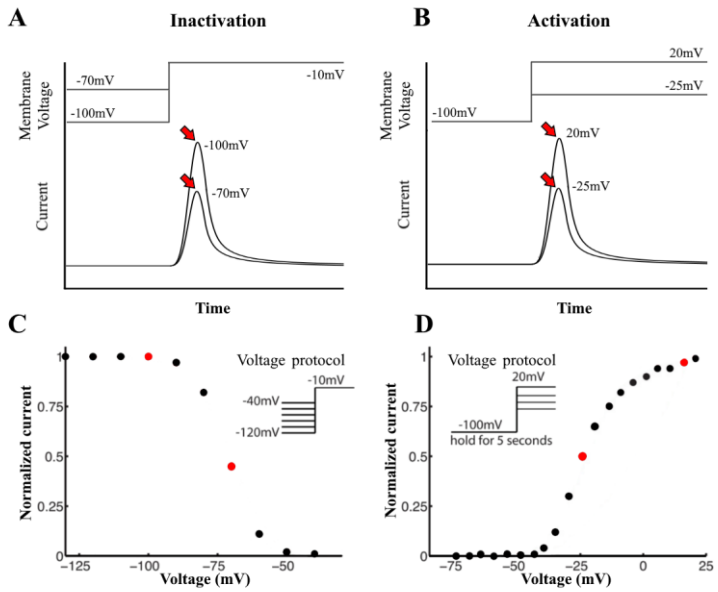

Figure 11. Representation of the activation and inactivation dynamics of I_{Naf}. Elicited current resulting of applying voltage steps to assess inactivation (A) and activation (B). Note that the two steps that are presented correspond to voltages that yield approximately 100% and 50% of the current. The red arrows indicate the point where the current would be measured (and normalized) in order to represent the corresponding red dots for the inactivation (C) and activation (D) curves. Insets in C and D illustrate the complete stimulation protocols that were used to obtain the curves. Panels C and D were adapted from Moreno and coworkers[77].

The channel activates quickly (within 2 ms), resulting in a peak sodium current provided an adequate voltage step is used. The closer the test potential is to the starting point, in this case the resting membrane potential, the lower the peak, until eventually no current can be registered. According to the Hodgkin-Huxley formalism, at resting membrane potential, m gates are closed, and h gates are open, therefore no current can flow through the channels. When exposed to more positive potentials, m gates quickly open allowing the current to activate. Both m and h gates "feel" the change in membrane potential, but h gates exhibit a slower closing rate (reflected by a greater τ at such potentials), which creates enough time frame for the current to flow before inactivating. Maximum peak currents are plotted as a function of pulse potential (panel D) to estimate m_∞ with a Boltzmann equation as the following

$$I(V) = G \cdot (V_m - E) \cdot \frac{1}{1 + e^{\frac{V_{1/2} - V}{k}}}$$

Boltzmann Eq.

$I(V)$ being the maximal current at voltage V, G the maximal conductance of the channel, E the sodium reverse potential, $V_{1/2}$ the half-activation voltage and k the slope factor. Therefore, m_∞ can be approximated by normalizing $I(V)$ and dividing by $(V_m - E)$. Note that the presence of three m gates in the sodium channel implies the observed conductance values are elevated by an exponent of 3. Hodgkin and Huxley determined the activation rate, τ, by testing which values gave the best fit to their results[71].

Inactivation is assessed by applying a series of pulses to variable test potentials for a fixed time that ensures steady state inactivation has been reached (panel A). Here, the current quickly activates and then inactivates according to the closing dynamics of the h gate (not shown). Then, a short 20 ms pulse to fixed high potentials of typically -10 mV is applied before going back to resting membrane potentials. The channels that inactivated during the first pulse cannot activate again during the second one, thus the current peak is the result of the channels that remain closed. The higher the voltage of the test pulse, the fewer the channels that are available for activation during the second pulse. Peak currents are then plotted as a function of test potentials and normalized to their maximum value to provide an approximation of the voltage dependent steady state inactivation (panel C), h_∞, while τ can be estimated for the activation gate[71].

In this PhD thesis, most of the ion channel models we used follow the Hodgkin-Huxley formalism. However, we also made use of Markov chain models for the sodium current because of their versatility towards reproducing complex dynamics.

2.6.2.2 The Markov chain models

Markov chain models, Markov models for short, first introduced in 1906 by Andrei Markov[78], are a useful representations of biophysical dynamics including cardiac ion channels. They quantitatively describe a stochastic process through a set of discrete states, coupled with rates that determine the transition velocities between them. The simplest Markov model contains two states (open and closed) and two transition rates (α and β), which is nothing but the representation of a gate in the Hodgkin-Huxley formalism[73,79,80]. States

are usually representations of specific conformations of the proteins that build the ion channels. According to the Markov property, transitions happen depending only on the currently occupied state, which is a feature of biologic systems that cannot be accounted for in the Hodgkin-Huxley formalism.

Like in the Hodgkin-Huxley formalism, Markov chain models of ion channels usually represent channel populations, therefore the addition of the occupancy probability of all states is 1. The system reaches steady state when the voltage is fixed during enough time so that the transition velocities between states equalize. The model has normally one or more open states representing the channel conformations that allow ions to flow through its pore. Channel conductance depends directly on the fraction of the channels that occupy these states.

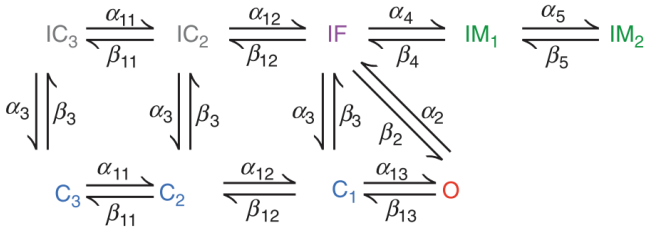

Figure 12. Representation of the Markov model of the SCN5A channel responsible for the I_{Na} current. Image obtained from Clancy and Rudy[81].

Markov models were required when more accurate representations of ion channels were necessary to explain the dynamics that Hodgkin-Huxley formulations could not. Study of the sodium channel revealed that its inactivation was faster in the open state[82,83], which is contrary to the concept of independent gates. A more detailed model of the sodium channel dynamics was created by Clancy & Rudy[81] to account for these new dynamics. In 2.2.1 we reviewed the structure of the sodium channel and highlighted the presence of several domains connected by linkers that modulate the channel's response to voltage changes. For example, each domain possesses a segment that functions as a voltage sensor which drives the channel's activation[84]. The III-IV linker appears to participate the fast inactivation of the current[85] which can be stabilized by the C-terminus[86], the final chain of the protein. These processes have been considered in the model structure (see Figure 12).

To represent the cooperativeness of the activation process, three closed states (C1, C2 and C3) were included instead of representing each voltage sensor separately. The inactivated state IF was added to reproduce fast inactivation

dynamics by the III-IV linker. IF was also connected O to reproduce its dependence on the open state. Stabilization of the inactivated state was modeled by including the IM1 state. Deeper, slow inactivation was taken into account by adding the IM2 state. Finally, the two closed inactivated states (IC2 and IC3) were included to represent the closed state inactivation. This model reproduces a fundamental property of the sodium channel, which is its rate dependence. While the states IM1 and IM2 remain almost unoccupied at slow rates, higher pacing rates shift the channel's conformations towards inactive states due to spending more time at depolarized potentials. Inactive channels take longer to recover before another pulse reaches the cell, which can lock them in that state thus reducing the total amount of current that gets triggered during the depolarization. This has direct effects on other currents' activations which plays an important role in the time course of the action potential and therefore in rate adaptation of the APD[87], among others. Many subsequent works have modified and improved this sodium channel formulation over the following years[77,88–91].

2.6.3 Cardiomyocyte action potential models

Cardiomyocyte modeling was first attempted in 1962[92]. From that moment, the scientific community has witnessed an authentic burst in number and variety of cardiac electrophysiological models helping understand the multiple mechanisms that shape the heart's function[93]. They have been developed from several species such as dog, guinea pig, rabbit, mouse, rat and, most importantly, human[94]. Some notable examples of the latter include the Ten-Tusscher[95], the Courtemanche-Ramirez-Nattel[96] and, more recently, the Grandi-Bers[97] and O'Hara-Rudy[98] models.

In 2.6.2.1, we introduced the cellular membrane and compared it to an electronic circuit with many variable resistors – the channels. We were able to do so by using the membrane capacity and the sum of all the currents that flow through the membrane. These concepts established the foundation for the action potential models.

Action potential models integrate information from several sources, which include electrophysiology models of ion currents studied in cardiomyocytes, cardiac tissue and transfected cells, as well as compartmental models based on imaging information of the sub-cellular structures. The study of the cell's individual components is sufficient to obtain an action potential model due to the multiscale nature of this modeling approach. The inherently modular nature of these models allows the reuse of some of its components. Consequently,

there are numerous examples of models combining ion currents whose data were obtained from different species[73].

Gates' condition in the Hodgkin-Huxley formalism and state occupancy in the Markov chain model formalism depend on membrane potential. The complexity of these models makes it impossible to resolve their evolution over time analytically, but they can be approximated using differential equations. However, the larger the number of gates or states, the larger the number of differential equations that have to be solved to describe the behavior of an ion current. Markov chain models like the I_{Na} and I_{Ks} models we reviewed in 2.6.2.2 are especially complicated for that reason. These mathematical problems are best solved numerically using ordinary differential equation (ODE) solvers provided in a wide variety of scientific software like Matlab (The MathWorks inc.), which we extensively used for the development of this PhD thesis.

These programs work under the principle that using short time steps (dt) in a system of differential equations turns it into an uncoupled system[99,100]. The system can then be solved by calculating every differential equation one at a time. Every time step, model states are updated by adding the amount resulting of their increment over the selected time interval. Of course, an initial set of states, which can be derived from the literature, must also be provided at the start of a simulation. An excessively large time step may trigger instabilities, whereby some states adopt incorrect values (for example, "not a number" or excessively large values) or fluctuate around a central value without ever stabilizing. Contrarily, excessively short time steps might delay the simulation's completion. While the latter case is not incorrect, adopting a time step leading to satisfactory results in the shortest time possible is advisable. Utilization of variable time steps is a very effective way of reducing the computational time that a model takes to perform a simulation. The phases of the action potential subject to rapid increments, such as phases 1 and 2, should be calculated at shorter time steps, but other phases with softer variations in membrane potential can be calculated at longer time steps, reducing the total number of computations that must be performed to complete the simulation.

2.6.4 Tissue models

Naturally, the next step after generating single cardiomyocyte action potential models (also called 0D models) is to bind them in several configurations. In the cardiac tissue, cells are interconnected through intercalated discs containing gap junctions, which behave much like ion channels. The same way there is a driving force between the exterior and interior of a cell, a driving

force exists between two neighboring cells. Therefore, it is possible to calculate the current from one cell to the other by using the same expressions as for individual ion channels. Assuming that a cell at position n is surrounded by two cells (n-1 and n+1), the existing gap junctions enable two currents, which are modulated by the gap junction conductance (G_{GAP}) as follows

$$I_{n,n-1} = G_{GAP} \cdot (V_n - V_{n-1}) \qquad \textbf{\textit{Eq. 8}}$$

$$I_{n,n+1} = G_{GAP} \cdot (V_n - V_{n+1}) \qquad \textbf{\textit{Eq. 9}}$$

The membrane voltage increment over time of cell n can be calculated with the following equation

$$\frac{dV_{m,cell\ n}}{dt} = \frac{I_{Ion} + I_{stim} + I_{n,n-1} + I_{n,n-1}}{C_m} \qquad \textbf{\textit{Eq. 10}}$$

Where I_{Ion} represents the membrane currents and I_{stim} a possible external stimulus current. Enabling coupling between cells implies that voltage differences between cells can now generate current flow. In fact, there is no need to stimulate all cells at the same time for a strand to be depolarized. Triggering a depolarization of one cell should trigger enough current in its neighbor to depolarize it as well in normal conditions, which is key to propagation. The gap junction conductance determines the delay between adjacent cell depolarizations. To calculate the conduction velocity, modelers identify this delay over a known distance, for example between a cell near the beginning and a cell near the end of a 1D strand (which is easier in models with homogeneously sized cells)[101].

To simulate a transmural section of the ventricular wall, strand models can be assigned layers of different cardiomyocytes. The configuration used by O'Hara and coworkers[98] used a strand of 165 cylindrical cells with 60 endocardial, 45 midmyocardial and 60 epicardial cells. Increase in dispersion of repolarization is one of the factors that affects arrhythmia generation (see 2.4), which can be simulated using these models.

Another parameter that can be calculated using a ventricular transmural strand is its pseudo-ECG. Works in the literature used a virtual electrode placed 2 cm form the epicardial end[90,98,102], where the spatially weighted addition of the voltage gradient was determined[101].

$$\Phi = \frac{\alpha^2}{4} \cdot \int (-\nabla V) \cdot \left[\nabla \frac{1}{x - x'}\right] dx \qquad \textit{Eq. 11}$$

Where Φ represents the unipolar potential of the electrode, α is the fiber's radius and $x - x'$is the distance from the electrode to any cell in the strand[103]. The resulting ECG does present a recognizable QRS complex and a T wave, but the P wave is generated by the atrial depolarization and therefore it cannot be present. Biomarkers as the pseudo-QT of the strand are useful in QT prolongation experiments, for example, under exposure to QT prolonging drugs.

2.6.5 Channel-drug interaction models

Channel-drug interactions are the core of arrhythmic and antiarrhythmic drugs, but they are far from the only mechanism. In this section, we will take on the main channel-drug interaction models that we used in this PhD thesis.

Drugs can bind to a wide variety of molecules including ion channels. A drug that enhances the response level of its receptor, in this case an ion channel, is called an agonist. The opposite definition of an agonist applies to inverse agonists, whose effect reduces the response level of their target. Finally, antagonists are drugs that bind to the same location of an agonist but produce no effect, thus effectively reducing the response level of the ion channel. Antiarrhythmic drugs block ion channels, which means they are inverse agonists, as they reduce their activity by binding to their proteic structure and changing the stability of their conformations[39].

While binding to the channel does not guarantee an effect, quantifying the response of a drug through receptor occupancy makes the basis in the law of mass action. A number n of ligands L and a receptor R can bind at a rate k1, creating L_nR, then dissociate at a rate k2, each depending on the amount of R, L_n and the complex L_nR, as described by the following diagram[39,104]:

$$R + L_n \underset{k_1}{\overset{k_2}{\leftarrow\!\rightarrow}} L_nR$$

At steady state, an equilibrium between both binding and unbinding velocities is attained. In that case,

$$[L_nR] \cdot k_2 = [R][L_n] \cdot k_1 \qquad \textbf{\textit{Eq. 12}}$$

K_A is defined as the equilibrium affinity constant:

$$K_A = \frac{k_1}{k_2} = \frac{[L_nR]}{[R][L_n]} \qquad \textbf{\textit{Eq. 13}}$$

K_d is defined as the equilibrium dissociation constant:

$$K_d = \frac{k_2}{k_1} = \frac{[R][L_n]}{[L_nR]} \qquad \textbf{\textit{Eq. 14}}$$

If R_0 is the total number of receptors,

$$R_0 = [L_nR] + [R] \qquad \textbf{\textit{Eq. 15}}$$

then it can be deduced that, for a number n of binding sites per receptor,

$$[L_nR] = [R_0] \cdot \frac{[L]^n}{[L]^n + {K_A}^n} = [R_0] \cdot \frac{[L]^n}{[L]^n + K_d} \qquad \textbf{\textit{Eq. 16}}$$

Where the concentration of L_nR complexes depends on the total amount of receptors R_0 (provided the number of ligands significantly exceeds the receptor concentration), the concentration of free ligands L, and the rates of dissociation and association k_1 and k_2. The number of binding sites (n) is also known as the Hill factor and should be considered a measure of molecularity and cooperativity. K_A describes the affinity of the ligand for the receptor. In the context of the agonist drug, previous equations can be reformulated to describe its characteristic concentration response curves as follows.

$$E = E_{max} \cdot \frac{C^n}{C^n + EC_{50}^n} \qquad \textbf{\textit{Eq. 17}}$$

This expression shows that the response to a concentration C of the agonist depends on the maximal response Emax and the half-maximal effect concentrations EC_{50}. The classical dose-response curves that can be described with this equation are depicted by Figure 13.

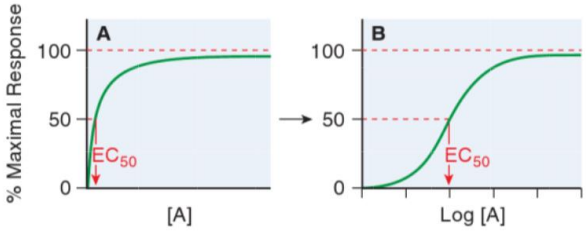

Figure 13. Typical response curves as a function of drug A concentrations. The dose-response curve shows a hyperbolic saturable dependence on concentrations of drug A, where the authors assigned 100% to Emax and an arbitrary value to EC_{50}. The shape of the curve turns into a sigmoid when represented in a semilogarithmic graph in panel B. Figure from Goodman and Gilman[39].

Eq. 17 can also be written as

$$E = E_{max} \cdot \frac{1}{1 + \left(\frac{EC_{50}}{C}\right)^n} \qquad \textbf{\textit{Eq. 18}}$$

Antiarrhythmic drugs usually decrease the activity of an ion channel, therefore acting as inverse agonists. Their effects can be described with half-maximal inhibition concentrations (IC_{50}) instead of EC_{50} with the following equation.

$$G = G_{max} \cdot \frac{1}{1 + \left(\frac{C}{IC_{50}}\right)^{H}} \qquad \textit{Eq. 19}$$

Where G, the conductance of an ion channel, depends on its maximal conductance (G_{max}), the concentrations of the drug (c), the half-maximal inhibitory concentration (IC_{50}) and H, the Hill coefficient (previously named n). This mathematical formula has been widely used to experimentally characterize drug effects on ion channel conductances, which has led to a widespread use in drug-channel modeling[58,65,66,69,90,91,105–108].

The Hill formalism is not the only description of the channel-drug interaction. In fact, as previously explored in 2.6.2.2, Markov chain models describe the ion channel dynamics in great detail and can also be extended to reproduce the effects of drugs on ion currents. This is done by including discrete states corresponding to drug-bound conformations of the channel[41]. Markov models have been widely used to describe channel-drug interactions[77,89–91,106,107,109,110].

Chapter 3. Development of an in-silico TdP biomarker for early proarrhythmicity detection

Romero, L., **Cano, J.**, Gomis-Tena, J., Trenor, B., Sanz, F., Pastor, M., et al. (2018). In Silico QT and APD prolongation assay for early screening of drug-induced proarrhythmic risk. J. Chem. Inf. Model. 58, 867–878. doi:10.1021/acs.jcim.7b00440.

*Romero L. and **Cano J.** contributed equally to the development of this work.*

3.1 Introduction

Ever since Torsade-de-Pointes (TdP) generation was found to be related to prolongations on the QT interval resulting from I_{Kr} block[39,48,49], this has been the main reason for drug withdrawal from 1990 to 2006[111]. Antiarrhythmic drugs can successfully prevent the incidence of lethal arrhythmias, but they can also be their cause. For example, amiodarone has shown great success treating atrial fibrillation and ventricular tachycardia prophylaxis[112], but it has also shown a high proarrhythmic potential[113]. It was attributed to its important off-target block of the key repolarizing I_{Kr} current[51] and marked QT interval prolongation[39]. There is a rising concern about proarrhythmic effects[114] since they are not restricted to antiarrhythmic compounds but span many drug types including antibiotics, antipsychotics and antihistamines[56]. This represents additional challenges in the drug development cycle. New compounds already take on average thirteen years to complete the required research and testing[115], during which the companies can spend anywhere from 50 to 2000 million dollars[116]. Current guidelines[14,15] expanded the required tests by including two new assays in order to test for proarrhythmic effects. The first is the hERG/I_{Kr} block assay, where the drug should not significantly reduce the I_{Kr} amplitude. Drug developers have commonly referred to an IC_{50} 1 μM as the lowest acceptable value. The second is the "thorough QT/QTc study", where the QT segment of healthy subjects under exposure to the new compound should not increase more than 5-10 ms compared to control conditions. A positive result in these assays could lead to removal of the compound from the development pipeline completely. To prevent drugs from being removed later in the development process, the industry routinely performs preclinical assays to assess APD prolongation or I_{Kr} block[117,118], thanks to which pharmaceutical companies can decide to preventively stop the compound's development in early phases an avoid unnecessary losses[102].

The current guidelines have successfully led to no drug-induced TdP among new drugs[118]. However, while this demonstrates that the assays that were proposed are sensitive, they have also shown poor specificity towards identifying TdP causing drugs[16]. First, the hERG channel (responsible for I_{Kr}) shows to bind to numerous structures. For that reason, its channel-drug interactions have been described as "promiscuous"[119–122]. In fact, up to 70% of the new compounds could block I_{Kr}[123]. Second, some drugs that strongly interact with it are paradoxically safe and have never produced Torsade-de-pointes, such as verapamil[48,65] or propafenone[65]. In fact, these drugs have shown block of other ion channels such as I_{CaL} or I_{Na}[58,65,66,124], suggesting that

other ion currents could modulate or even counteract the effects of I_{Kr} block. Third, the thorough QT/QTc cannot identify the cases where the prolongation arises from interaction with channels other than hERG. Consequently, current guidelines have prevented many potentially beneficial drugs from reaching the market[125,126].

The Comprehensive in vitro-in vivo Proarrhythmia Assay (CiPA) acknowledged these challenges and is currently developing a new paradigm for drug testing during development[17]. Their approach is based on the understanding of the fundamental mechanisms that drive the cardiac electrophysiology, which are rooted in the study of the ion channels. They proposed a list of "components" designed to evaluate the drug's effect on human cardiac ion channels and stem cell derived cardiomyocytes, together with more traditional clinical trials. Importantly, the CiPA project included an in-silico component aiming to develop a reference model to assess the compounds' effects on the cardiac electrophysiology using data from the in vitro tests, which highlights the importance of in silico modeling in modern TdP prediction. The proposed reference drug classification was the one from the Arizona Center for Education and Research on Therapeutics (AZCERT) website, today known as Crediblemeds (www.crediblemeds.org).

Several works in the scientific literature created biomarkers to attempt to predict drug TdP risk. A work that focused on the drug's I_{Kr} block potency found that a 30-fold margin between the effective free therapeutic plasma concentration (EFTPC) and I_{Kr} IC_{50} would ensure an adequate degree of safety[48], which highlights the importance of EFTPC. Mirams and coworkers[65] proposed a biomarker based on a linear discriminant analysis of the steady state APD_{90}. They tested several in silico models for risk predictions based on a 5-ms prolongation of the APD_{90} threshold for determining dangerous drugs. They found that the O'Hara-Rudy model of the human ventricular cardiomyocyte[98] performed the best, albeit under exposure to 100-fold the maximum plasma concentration (Cmax). Kramer and coworkers[58] tested several models including combinations of logarithmic differences between the I_{Kr} and other channel's IC_{50}s. They found that this value showed the best results when set between the I_{CaL} and I_{Kr} IC_{50}s, which underlined both the need for multi-channel block and the important role of I_{CaL} in TdP prevention. A previous work from our group[127] showed that classification of compounds could be improved by including their I_{Ks} block together with their I_{Kr} block.

It is also relevant to mention more recent works from other authors that were published while the study of the present chapter was being performed. Passini and coworkers[128] analyzed the occurrence of repolarization abnormalities in

populations of human AP models to create a classifier for TdP using a 62-compound list. They also showed that their classifier could perform similarly, or even better than studies in animals. Dutta and coworkers[107] found that combining the net charge flowing through six membrane ion channels during one beat (qNet) could correctly classify a list of 12 compounds in three different risk groups (low, intermediate and high). The authors validated the classifier with the 16-compound validation list from CiPA in a later work[105]. These results were obtained for concentration ranges from up to 25 times the free plasma concentration (called Cmax in their work). Parikh and coworkers developed classifiers for TdP risk stratification from direct features[129]. Abassi and colleagues also studied the early assessment of proarrhythmic risk of drugs using in vitro data and unicellular simulations. They reproduced the characteristics of the effects of drugs in AP duration and QT prolongation and TdP published 3D simulations, but with much smaller computational costs.

3.1.1 Objectives

To summarize, drug-induced arrhythmia represents a great challenge for companies, regulators, and patients. The abovementioned biomarkers were developed to answer the need to detect compounds with potential proarrhythmic effects and have shown good results. However, many of them rely on on-demand simulations with AP models, sometimes requiring several iterations or even populations of hundreds or even thousands of models. Additionally, the performance of QT intervals measured in tissue strand for the prediction of TdP potential has yet to be assessed. Therefore, to address this challenge, we ought to create a new easy-to-use biomarker for drug TdP potential prediction in early stages of their development. We split this chapter in three stages that will guide our work towards the consecution of our main goal. First, we ought to pre-compute a large number of simulations covering a wide range of three ion-channel block combinations (I_{Kr}, I_{Ks} and I_{CaL}), both in cellular and tissue models, to reduce the technical requirements. Then, we ought to create a biomarker that integrates the pre-computed multi-channel block results and therapeutic concentrations to predict the TdP potential of an extensive list of drugs. Finally, we ought to evaluate the performance of our biomarker on our drug dataset.

3.2 Materials and methods

3.2.1 Models

The O'Hara-Rudy (ORd)[98] (see Figure 14) model of the human ventricular cardiomyocyte was the state-of-the-art model when this study was conceived.

It was calibrated by studying the electrophysiological behavior of samples from more than 100 human hearts.

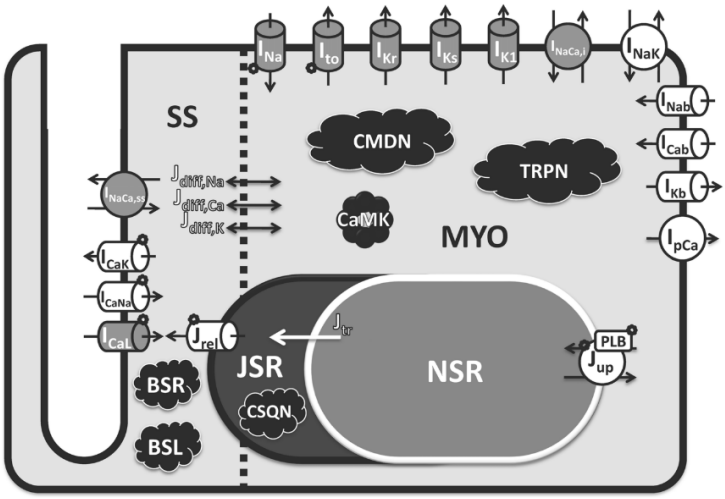

Figure 14. Diagram of the O'Hara-Rudy model of the human ventricular cardiomyocyte. Figure from extracted O'Hara and coworkers[98].

The ORd model reproduces the action potential (AP) time course of three cardiac cell-types (endocardial, midmyocardial and epicardial) by adapting several ion current conductances and parameters, thus making it easy to study the effects of external agents on three different cardiac cells.

The ORd 1D model consists of a transmural strand of 165 cells, divided into three sections. A first section of 60 endocardial cells represents the inner part of the cardiac ventricular wall and is followed by a 45-cell section of midmyocardial cells representing the core of the wall. The outer part of the wall corresponds to the last 60 cell section of epicardial cells. The ORd 1D model can also be used to calculate the pseudo-ECG. To do so, we used a virtual electrode 2 cm away from the last epicardial cell. To prevent boundary effects, the first and the last fifteen cells were omitted in the gradient calculation.

We stimulated the single cell ORd model delivering a train of square pulses of 0.5 ms duration and -80 pA/pF directly to the cell membrane. Each one caused an increase in membrane potential of approximately 1.5 times the one required to start the depolarization phase, triggered entirely by the fast sodium current

or I_{Naf}. Contrarily, the ORd 1D model required a train of -210 pA/pF, 0.5 ms duration, square pulses to the first endocardial cell. This was also 1.5 times the diastolic depolarization threshold and safely triggered the depolarization of the stimulated cell and propagated through the strand as abovementioned.

To study drug effects on the human AP and pseudo-ECG, we ought to create a precomputed matrix covering a wide variety of drug profiles. Precomputed matrices allow for fast and easy-to-use tools by avoiding long simulation times, which are done in advance, but need to cover a large portion of the simulation space. To do so, we introduced an extensive array of ion channel block combinations into the latter models by using the Hill equation or simple pore block model with a coefficient of 1. We tested drug effects in three currents belonging to three main ion channels, known to have an important role in AP repolarization, by applying the resulting fraction of unblocked channels of a set of concentrations and IC_{50}s to their maximal conductances. These were the fast and slow potassium rectifier currents (I_{Kr} and I_{Ks}) and the type-L calcium current (I_{CaL}). To cover a large range of drug types, we considered a three-dimensional array of $\log_{10}\left(\frac{D}{IC_{50}}\right)$ combinations and assigning one dimension to each channel. These values show the logarithmic distance between drug concentrations (D) and IC_{50}s for that channel. Negative values indicate that the IC_{50} is greater than drug concentrations. Positive values indicate the opposite, while a value of zero indicates that both parameters are identical. In the latter case, half of the channels are blocked thus reducing the conductance of the affected channel by a 50%.

We limited the I_{Kr} and I_{Ks} coordinate ranges to values from -3 to 1 (from nearly 0% to 90% block) while the I_{CaL} axis took values between -3 and 0 (from nearly 0% to 50% block), both in all three single cellular and strand models.

For single cellular models, we set the logarithmic resolution of all axis to 0.1. This means that a total of 206766 simulations, including controls, were necessary to populate all three arrays, one for each cell type. For 1D model simulations, coordinate axis resolutions were not uniform. It was due to the computationally intensive workload of simulating all the drug block combinations, which increases exponentially with finer resolutions. Specifically, I_{Kr} logarithmic resolution was set to 0.2 except for the ratios between -1.2 and -0.2, where it was set to 0.1. I_{Ks} and I_{CaL} logarithmic resolutions were respectively set to 0.25 and 0.2. Including controls, we performed 7072 simulations with the 1D model.

3.2.2 Drug dataset

We gathered a drug set combining the information found in several sources. First, we consulted the drug's proarrhythmic risk in CredibleMeds.org, the reference proposed by the CiPA project. Crediblemeds is dedicated to monitoring specifically compounds that exhibit risk of developing Torsade-de-Pointes (TdP), covering all drug structures and therapeutic targets. In the site's words, it "has developed a risk-stratification process – the Adverse Drug Event Causality Analysis (ADECA) – that includes monitoring and analysis of 1) scientific articles in the published medical literature, 2) information in the official drug label, 3) reports submitted to its website and 4) data in the FDA's Adverse Event Reporting System (AERS) using Oracle's Empirica Signal software". The risk stratification results in the inclusion of monitored compounds in one out of four risk categories as described by Table 2: class 1, compounds that show known risk of TdP; class 2, compounds with possible risk of TdP; class 3, compounds with conditional risk of TdP; and class 4, drugs that should be avoided by patients with congenital LQTS. The latter group gathered the drugs not belonging to groups 1-3.

Table 2. TdP risk classification proposed by the Crediblemeds website (www.Crediblemeds.org).

Risk of TdP	Description
Known risk	These drugs prolong the QT interval AND are clearly associated with a known risk of TdP, even when taken as recommended.
Possible risk	These drugs can cause QT prolongation BUT currently lack evidence for a risk of TdP when taken as recommended.
Conditional Risk	These drugs are associated with TdP BUT only under certain conditions of their use (e.g. excessive dose, in patients with conditions such as hypokalemia, or when taken with interacting drugs) OR by creating conditions that facilitate or induce TdP (e.g. by inhibiting metabolism of a QT-prolonging drug or by causing an electrolyte disturbance that induces TdP.)
Drugs to avoid in congenital LQTS	These drugs pose a high risk of TdP for patients with CLQTS and include all those in the above three categories (KR, PR & CR) PLUS additional drugs that do not prolong the QT interval per se but which have a Special Risk (SR) because of their other actions.

For our risk classifier, we binarized these categories into dangerous and safe drugs. Classes 1 and 2 were grouped into drugs that can or may prolong the QT interval on their own. Classes 3 and 4 were grouped into drugs that are safe. These drugs cannot produce TdP on their own or specific conditions must be attained to manifest proarrhythmicity. Although in many cases, reports of these drugs show a possible relationship with TdP, there is not enough evidence to support their causality. Nonetheless, some of the drugs in our list were not available in CredibleMeds.org, in which case they were automatically included in the fourth category and in our safe drug group.

We also searched for specific data to simulate their effect on the ORd human ventricular cardiomyocyte and strand models. Parameters that we extracted include IC_{50}s for I_{Kr}, I_{Ks} and I_{CaL} currents and therapeutic concentrations. We extracted free plasma drug concentrations, $[C]_{free}$, from total blood concentrations, $[C]_{total}$, by means of plasma protein binding fractions, f_b.

$$[C]_{free} = [C]_{total} \cdot (1 - f_b) \qquad \textbf{Eq. 20}$$

Free plasma concentrations can diffuse from blood plasma through the extracellular medium and interact with ion channels, contrarily to protein bound compound. Due to the size of soluble plasma proteins (mainly albumin), bound drug molecules get trapped and are not able to interact with ion channels in cardiac cell membranes.

When mass concentrations were available, plasma concentrations were calculated using molar mass to extract total blood concentrations.

$$[C]_{total} = \frac{[C]_{mass}}{Molar\ Mass} \qquad \textbf{Eq. 21}$$

Therapeutic concentrations are usually given as a range in which the drug shows an optimal balance between therapeutic and unwanted or side effects. We consistently selected the maximum value of the concentration range. Alternatively, when therapeutic ranges were not available, we selected peak plasma concentrations, either mass or molar concentrations, resulting from the

highest commonly used dosage form found in clinical trials inside FDA drug labels[130].

As for IC_{50} values, there is a variable amount of data for every compound and ion channel. Some well-studied compounds show large amounts of data obtained with different techniques, temperatures, and stimulation protocols. Tthese values are usually obtained through a whole-cell patch-clamp technique. Xenopus Oocytes, also known as frog eggs, have been commonly used to assess ion channel dynamics but they have proven to give altered IC_{50}s, thus we decided to avoid these systems. Only mammalian cell experiments were included in this work, either transfected or not.

We used all available IC_{50} data by calculating their median value. In this work, and in cases when multiple values of IC_{50} have been reported for the same compounds in the literature, we faced the need of summarize them in a single value. The median offers the advantage of being more robust to the presence of extreme values and outliers among the alternatives provided by Biostatistics for characterizing the central tendency of a set of experimental values.

IC_{50} values are often given in the form of pIC_{50} which can be calculated with the following equation:

$$pIC_{50} = -\log_{10}(IC_{50}) \qquad \textbf{\textit{Eq. 22}}$$

The databases that we consulted to obtain the required information include public databases such as Tox-Portal[131], DailyMed[130], PubChem[132] and Drugbank[133]. When data was not available in these resources, we searched in the scientific literature.

3.2.3 Simulation Protocols

Unless otherwise specified, we used a standard stimulation frequency of 1Hz for all our simulations, as it is widely used in human cardiac cell simulation[65,66,134–136]. Additionally, we performed simulations at 0.5 Hz and 2 Hz to test the frequency-dependent variability of our results.

We brought our models to steady state by pacing the single cellular models with 1000 pulses. Final states from these simulations were introduced into the ORd 1D model as initial conditions and we ran the latter model for 100 pulses to bring the strand model to steady state in control.

Drug effects were simulated in a similar fashion. This time, single cellular models with the initial conditions corresponding to the steady-state in control were paced with 1000 additional pulses after including drug-induced ion channel block. Final states from these simulations were used to start 1D model simulations maintaining drug effects on current conductances. We then simulated the ORd cell strand model for 100 beats to reach steady state under drug exposure.

We saved the last pulse of every simulation and analyzed the action potential duration at 90% repolarization (APD_{90}) using single cellular models and the pseudo-QT duration using the strand model.

3.2.4 Torsadogenic risk classification with Tx

We used 10% prolongation of the QT interval as our reference to calculate a new TdP risk, which we called Tx. We calculated Tx as the distance between EFTPC and the concentrations that produced a 10% prolongation of the QT intervals or APD, taking into account the block of all the channels of our dataset.

Receiver Operating Characteristic (ROC) curves are a tool that is commonly used in medicine to assess the performance of diagnostic tests[137]. The four possible outcomes of a diagnostic test depend on whether its result matched the actual condition of the patient (true cases) or not (false cases) and whether it indicated that the patient had the disease (positive result) or not (negative result). The amount of each of the outcomes varies depending on the threshold that is applied to the classifier. Eventually, there is a value that gives an optimal result, maximizing the true cases in both diseased and healthy patients. This value can be easily obtained using ROC curves. For that reason, we used them to evaluate the performance of Tx.

3.3 Results

3.3.1 APD and QT

Table 3. Characteristics of the 84-drug dataset. From left to right, the columns indicate the name of the compound (name), torsadogenic risk classification (Class), pIC_{50} values for I_{Kr}, I_{Ks}, and I_{CaL} (columns 3 to 5), effective free therapeutic plasma concentrations (EFTPC), fraction of protein-bound drug (f_b), molar concentration (Mol. C), molar mass (Mol. mass), maximum concentration in blood achieved during therapeutic treatment (C_{max}) and its corresponding units. The color-coded background of the first column corresponds to the following Crediblemeds classes: red (Class 1), orange (Class 2), bright green (Class 3) and dark green (Class 4). See section 3.6 in this chapter for references of these values.

Drug		pIC_{50}			Concentrations					
Name	**Class**	**I_{Kr}**	**I_{Ks}**	**I_{CaL}**	**ETFPC (nM)**	**f_b**	**Mol. C (nM)**	**Mol. Mass (g/mol)**	**C_{max}**	**Unit**
Ajmaline	1	5.98	-	-	1500					
Amiodarone	1	6.38	5.59	6.57	63.5	0.999	63535.20	645.3116	41	µg/mL
Astemizole	1	8.22	-	5.98	0.3					
Bepridil	1	7.16	5.10	6.08	33					
Chlorpromazine	1	5.81	3.00	4.15	66.4					
Cilostazol	1	4.86	-	4.04	162.4	0.95	3247.98	369.46068	1200	ng/mL
Cisapride	1	7.68	5.47	4.56	4.9					
Clarithromycin	1	4.06	-	-	4011	0.7	13369.82	747.95336	10	µg/mL
Disopyramide	1	5.00	4.09	4.96	4713	0.6	11782.92	339.47446	4	µg/mL
Dofetilide	1	7.75	-	-	2					

Drug		pIC50			Concentrations					
Name	Class	I_{Kr}	I_{Ks}	I_{CaL}	ETFPC (nM)	f_b	Mol. C (nM)	Mol. Mass (g/mol)	C_{max}	Unit
Domperidone	1	6.88	-	-	5.79	0.92	72.39	425.911	30.83	ng/mL
Donepezil	1	6.16	-	4.47	6.56	0.96	164.00			
Dronedarone	1	7.29	5.00	6.75	0.79	0.997	264.03	556.75646	147	ng/mL
Droperidol	1	7.22	-	5.12	16					
Flecainide	1	5.82	-	4.57	1448	0.4	2413.46	414.342719	1	µg/mL
Halofantrine	1	6.42	-	5.72	172					
Haloperidol	1	7.44	-	5.77	3.6					
Ibutilide	1	7.75	-	4.20	22	0.4	15.08	384.57644	14.4	ng/mL
Levofloxacin	1	3.37	-	-	30932	0.31	33483.92	361.367503	16.2	µg/mL
Methadone	1	5.46	-	4.43	507					
Moxifloxacin	1	4.11	3.80	3.40	6228	0.5	11209.89	401.431363	5	mg/L
Ondansetron	1	6.09	3.00	-	178.6	0.73	662.66	293.36296	194.4	ng/mL
Procainamide	1	3.57	-	3.41	35058	0.175	42494.36	235.32534	10	µg/mL
Quinidine	1	5.90	4.36	4.81	2960	0.84	18500			
Sotalol	1	3.29	-	-	18358					
Sparfloxacin	1	4.66	-	4.05	1766					
Tedisamil	1	6.66	5.19	-	85					
Terfenadine	1	7.30	5.36	6.51	9					
Terodiline	1	6.71	4.56	4.87	11.23					
Thioridazine	1	6.70	4.99	5.88	979					
Clozapine	2	5.64	-	5.44	70.8	0.97	2359.07	326.82326	771	ng/mL
Dasatinib	2	4.80	3.60	3.40	20.4					

Drug		pIC50			Concentrations					
Name	Class	I_{Kr}	I_{Ks}	I_{CaL}	ETFPC (nM)	f_b	Mol. C (nM)	Mol. Mass (g/mol)	C_{max}	Unit
Lapatinib	2	6.00	3.60	2.70	41.8	0.99	4182.03	581.057543	2.43	µg/mL
Nilotinib	2	6.90	3.40	3.70	60					
Ofloxacin	2	2.85	-	-	8656	0.32	12729.42	361.3675	4.6	µg/mL
Paliperidone	2	5.90	3.60	3.40	68.9	0.74	264.96	426.483883	113	ng/mL
Risperidone	2	6.63	5.01	4.14	6.96					
Saquinavir	2	4.77	-	5.72	334	0.98	16695.47	670.8408	11.2	µg/mL
Sunitinib	2	6.60	4.20	4.10	19	0.925	253.47	398.473783	101	ng/mL
Tolterodine	2	7.90	4.10	-	0.39	0.963	10.45	325.48764	3.4	ng/mL
Metronidazole	3	2.87	-	3.75	210336					
Nelfinavir	3	4.90	4.10	-	60.25	0.99	6025.11	663.88806	4	µg/mL
Paroxetine	3	5.72	-	5.41	12.7	0.94	211.62	329.365403	69.7	ng/mL
Quetiapine	3	5.42	-	4.98	461.9	0.83	2717.03	383.507	1042	ng/mL
Ranolazine	3	4.90	2.72	3.51	2311	0.62	6081.35	427.53652	2600	ng/mL
Solifenacin	3	6.60	4.50	5.20	3.47	0.98	173.53	362.46474	62.9	ng/mL
Voriconazole	3	3.31	-	3.38	5699	0.58	13569.59	349.31047	4.74	µg/mL
Alvimopan	4	3.10	4.30	5.30	5.17	0.8	25.86	424.53258	10.98	ng/mL
Ambrisentan	4	3.30	3.30	2.60	75.3					
Ceftriaxone	4	3.35	-	3.81	13704	0.9	137040.66	554.57992	76	µg/mL
Darifenacin	4	7.10	4.70	2.80	0.27					
Darunavir	4	3.80	3.50	-	862.5					
Deferasirox	4	2.40	-	3.00	1403					
Desvenlafaxine	4	3.60	-	-	3901					

Drug		pIC50			Concentrations					
Name	**Class**	**I_{Kr}**	**I_{Ks}**	**I_{CaL}**	**ETFPC (nM)**	**f_b**	**Mol. C (nM)**	**Mol. Mass (g/mol)**	**C_{max}**	**Unit**
Diazepam	4	4.27	-	4.52	29					
Diltiazem	4	4.88	-	6.12	120.6	0.75	482.49	414.51784	200	ng/mL
Doxorubicin	4	3.00	5.32	-	4646	0.75	18582.60	543.51926	10.1	µg/mL
Duloxetine	4	5.42	5.00	5.55	9.22	0.95	184.32	297.415	54.82	ng/mL
Ebastine	4	6.14	6.10	-	0.14	0.99	13.83	469.6576	6.495	ng/mL
Eltrombopag	4	6.20	-	-	158.9	0.99	15888.21	442.46658	7.03	µg/mL
Etravirine	4	3.80	2.90	-	3.38					
Everolimus	4	3.30	4.00	-	8.03	0.74	30.89	958.22442	29.6	ng/mL
Lamivudine	4	2.69	-	4.27	1446	0.36	2259.42	663.88806	1.5	µg/mL
Lamotrigine	4	3.60	3.80	2.80	19083					
Linezolid	4	2.94	-	3.98	24856	0.35	39721.82	337.346103	13.4	mg/L
Loratadine	4	5.22	-	4.94	0.4					
Maraviroc	4	4.40	4.20	-	415	0.76	1728.75	513.665546	888	ng/mL
Mibefradil	4	5.77	4.93	6.29	12					
Mitoxantrone	4	3.27	-	4.65	225					
Nebivolol	4	6.50	4.80	-	1					
Nifedipine	4	3.87	3.44	7.28	32.3	0.95	646.20	346.3346	223.8	ng/mL
Nisoldipine	4	4.64	4.40	7.10	0.10	0.99	10.30	388.4144	4	ng/mL
Palonosetron	4	5.70	4.30	3.40	1.04	0.62	2.73	296.40666	0.81	ng/mL
Pentobarbital	4	2.84	3.72	3.52	5171					
Phenytoin	4	3.83	3.00	4.66	3964	0.95	79280.77	252.26798	20	µg/mL
Propranolol	4	5.09	3.00	4.71	10.1	0.9	100.64	259.34344	26.1	ng/mL

Drug		pIC50			Concentrations					
Name	**Class**	**I_{Kr}**	**I_{Ks}**	**I_{CaL}**	**ETFPC (nM)**	**f_b**	**Mol. C (nM)**	**Mol. Mass (g/mol)**	**C_{max}**	**Unit**
Raltegravir	4	3.11	4.60	3.61	7000					
Ribavirin	4	3.02	-	3.21	15069	0	15069.33	244.20468	3680	ng/mL
Sildenafil	4	4.50	3.40	4.00	100					
Silodosin	4	5.10	3.60	3.10	11.2	0.97	372.93	495.53449	184.8	ng/mL
Sitagliptin	4	3.83	3.10	3.83	589	0.38	950			
S-oxybutynin	4	4.92	4.54	4.79	0.05	0.99	5.04	357.48644	1.8	ng/mL
Tadalafil	4	4.00	3.80	-	50.1	0.94	834.61	389.40396	325	ng/mL
Telbivudine	4	0.80	3.60	-	14731	0.033	15233.55	242.22856	3.69	µg/mL

We simulated the effects of 84 compounds, whose parameters can be consulted in Table 3, on three ion channels responsible for I_{Kr}, I_{Ks} and I_{CaL} currents, in four different models that include endocardial, midmyocardial and epicardial isolated cells, as well as a 1D tissue model of 165 cells with three sections containing the beforementioned cell types.

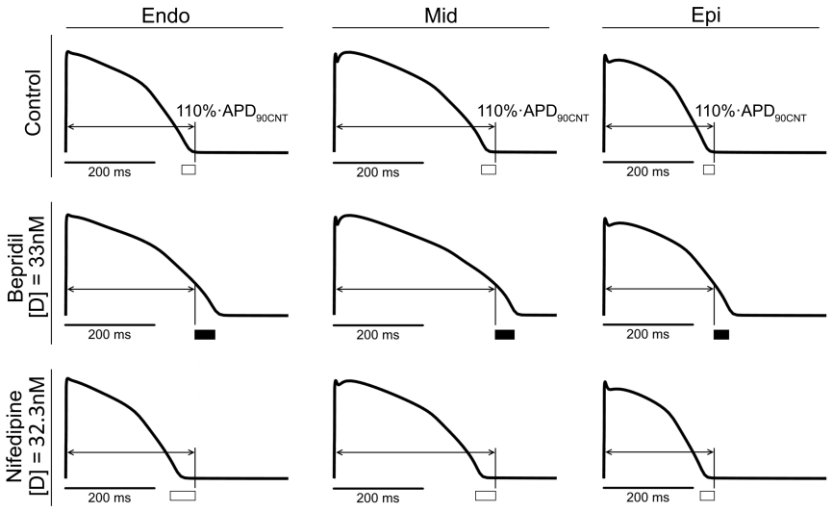

Figure 15. Simulated time course of the action potential obtained using the single cellular models. Endocardial (left column), midmyocardial (middle column) and epicardial (right column) action potential time courses. We simulated the models in control (top row) and under the exposure to therapeutic concentrations of bepridil (33 nM, class 1 drug, middle row) or nifedipine (32.3 nM, class 4 drug, bottom row). Vertical lines in each panel correspond to a 10% prolongation of the control APD_{90} (APD_{90CNT}).

Figure 15 depicts examples of drug effects on the action potential time course obtained using the single cellular models by bepridil and nifedipine, tested at their therapeutic concentrations (D) of, respectively, 33 nM and 23.3 nM. Bepridil is considered a dangerous compound (class 1 by Crediblemeds) while nifedipine belongs to the safe group (class 4). Controls were placed in the first row while simulations with drugs were placed in the second and third row. Columns were organized into cell types. From left to right, endocardial (Endo), midmyocardial (Mid) and epicardial (Epi) action potentials were shown. Vertical lines were added to indicate a 10% prolongation of the control APD_{90} (APD_{90CNT}). Squares show a comparison between the latter and the actual

APD_{90}, filled squares representing greater values and open squares representing lower values. Control APD_{90}s were 266.4, 330.3, and 223.8 ms for endocardial, midmyocardial and epicardial cells, respectively.In this figure, when exposed to 33 nM of bepridil, all single cellular models show marked prolongations of the APD_{90}, reaching 331.1 ms, 398.0 ms, and 278.0 ms, respectively, which correspond to 24.3%, 20.5%, and 24.2% increases, respectively, compared drug-free conditions. Exposure to nifedipine at 32.3 nM concentration caused the opposite effect by consistently reducing all APD_{90}s to 236.6 ms, 315.7 ms, and 216.1 ms, respectively, which corresponds to −11.2%, −4.4%, and −3.4% increases relative to drug-free conditions.

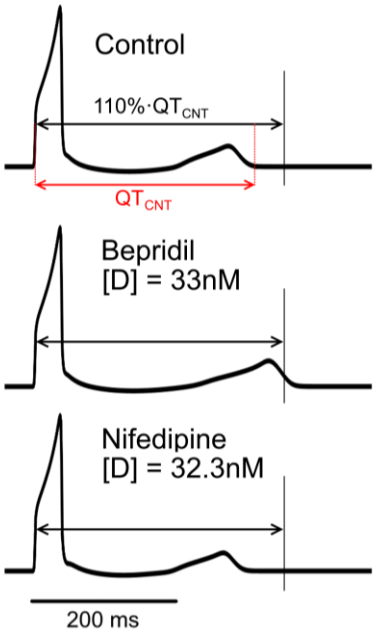

Figure 16. Time course of the ECG obtained using the transmural strand model. We simulated the model in control (top panel) and under exposure to therapeutic concentrations of bepridil (33 nM, class 1 drug, middle panel) and nifedipine (32.3 nM, class 4 drug, bottom panel). Black vertical lines indicate a 10% prolongation of the strand's control QT (QT_{CNT}).

In Figure 16, we combined the results of simulations with previous example compounds in the virtual transmural cell strand. From the 100 beats, we extracted the last one's pseudo-ECG in control (top), bepridil (middle) and nifedipine (bottom) at their therapeutic concentrations. Vertical lines represent

the 10% prolongation of the control QT interval, which was also indicated in red. Control QT interval was 313 ms. The effects of bepridil largely differed from those of nifedipine similarly to what we found in single cell simulations. While bepridil markedly prolonged the QT interval to 376 ms, corresponding to a 20.1% increase with respect to the control value, nifedipine exerted a shortening effect, resulting in a QT interval of 299 ms, corresponding to a 4.5% decrement.

These results can be explained by the compound's ion channel block profile. Our data on bepridil show an I_{Kr} pIC_{50} of 7.16 (approximately 70 nM), an I_{Ks} pIC_{50} of 5.10 (7.9 µM) and an I_{CaL} pIC_{50} of 6.08 (830 nM). At its therapeutic concentration of 33 nM, it is able to reduce the I_{Kr} conductance a 30% approximately while interactions with the other channels remains very unlikely. As we explored in 2.4, I_{Kr} impairment slows repolarization and thus contributes to maintaining the membrane potential during the plateau phase elevated longer. This is translated into an increase in the APD_{90}, which is also present throughout the 1D strand. Since the T wave also accounts for the repolarization of the strand, the later the repolarization, the later the T wave will appear and thus the resulting QT interval will be greater. In contrast, nifedipine mainly interacts with the I_{CaL} ion channel. With a pIC_{50} of 7.28 (52 nM), three points higher than the other channels pIC_{50}s, and a therapeutic concentration of 32.3 nM, it should block approximately a 38% of the I_{CaL} channels. Contrary to I_{Kr}, I_{CaL} plays a relevant role in maintaining the plateau membrane potential, thus repolarization is enhanced by reducing the amount of this current, which in turn generates shorter APD_{90}s and QT intervals.

Although at its therapeutic concentrations bepridil shows a preferential block of I_{Kr}, other compounds may not show the same selectivity and thus their effect on APD_{90} and QT values might increase in complexity, thus increasing the difficulty of predicting their proarrhythmicity. To facilitate this task, we created 3D matrixes for every model with multiple channel block combinations covering a wide range of possible drugs.

Figure 17 contains 3D representations of some results from the matrices obtained with the four models, namely, endocardial (top left), midmyocardial (top right) and epicardial (bottom left) isolated cells and transmural strand (bottom right). Coordinate axes represent the logarithmic distances between the drug's plasma concentration and the IC_{50}s for I_{Kr} (width), I_{Ks} (depth) and I_{CaL} (height). Matrices are filled with APD_{90}s (single cellular models) or pseudo-QT intervals (1D model), although the only values that are represented in the figure take the shape of the blue striped surface that marks the values corresponding to a 10% prolongation of the control QT or APD_{90} values.

Compounds that fall left to this surface produce greater prolongations while compounds that fall right to the surface prolong APDs and/or QT values less than a 10% or even shorten them.

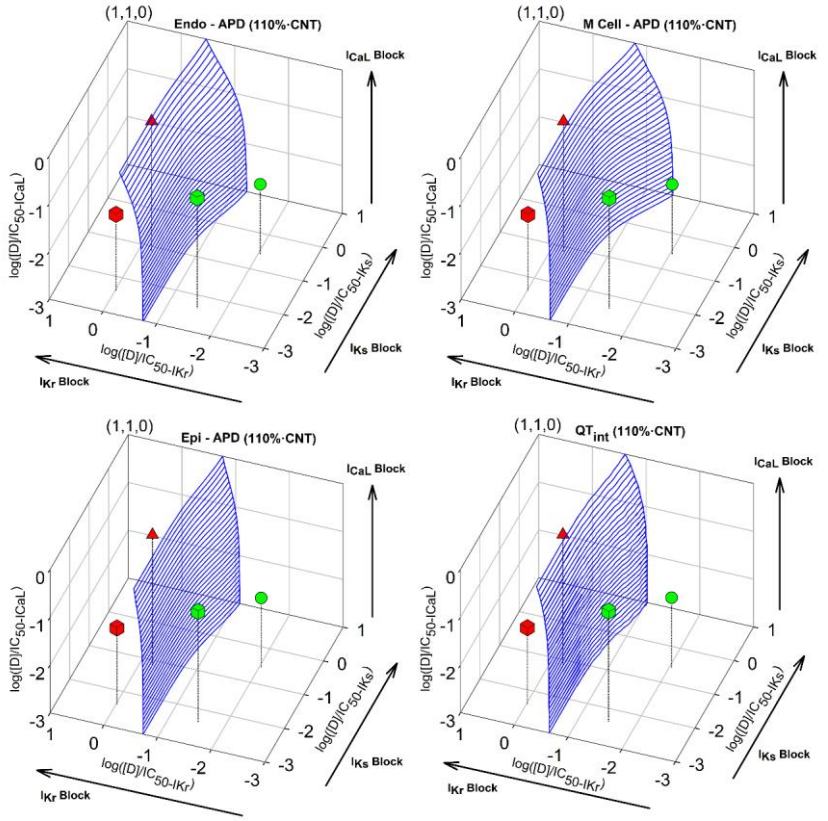

Figure 17. Three-dimensional representation of the surface (blue striped) corresponding to the 10% prolongation of the control endocardial (top left), midmyocardial (top right), and epicardial (bottom left) APD_{90}s and QT interval (bottom right). Symbols correspond to disopyramide (class 1 drug, red triangle), bepridil (class 1 drug, red cube), raltegravir (class 4 drug, green circle) and phenytoin (class 4 drug, green cube). Coordinate axes represent the logarithmic distance between drug concentration and IC_{50} of each channel ($\log_{10}([D]/IC_{50})$).

Four examples of drugs are illustrated in the figure, where known proarrhythmic drugs disopyramide (red triangle) and bepridil (red cube) at

therapeutic concentrations fall in the left side, while safe drugs raltegravir (green sphere) and phenytoin (green cube) at therapeutic concentrations are in the right side of the cubes.

Overall, blue surfaces exhibit similar patterns, bending towards the right (to more negative I_{Kr} pIC_{50}s) when I_{Ks} is blocked due to the synergic effects of blocking both potassium repolarizing currents, although the importance of such phenomenon is more pronounced in the midmyocardial cell model. Contrarily, the surfaces bend towards the left (to more positive I_{Kr} pIC_{50}s) when I_{CaL} conductance is reduced, showing the opposite nature of this current, its depolarizing role and the effect of drugs that can block it.

3.3.2 Proarrhythmicity assessment

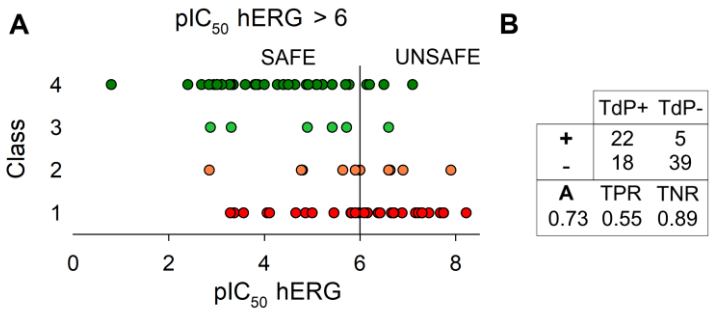

Figure 18. Classification of the 84-drug dataset according to the hERG pIC_{50} > 6 criterion. A: hERG pIC_{50} values grouped by Crediblemends class. A black vertical line indicates the threshold separating the two possible outcomes of the test, namely, safe compounds (-) that fall left and unsafe (+) compounds that fall right. B: confusion matrix summarizing the results of panel A. Classes 1 and 2 were considered "TdP+" while classes 3 and 4 were considered "TdP–".

Figure 18 shows the result of classifying the proarrhythmic effect of the 84-drug list using a threshold of 6 in the I_{Kr} pIC_{50}. Panel A depicts the distribution of pIC_{50} values grouped by CredibleMeds drug class, which we binarized by considering classes 1 and 2 (red and orange, respectively) as dangerous and 3 and 4 as safe (lime and green, respectively). The vertical line marks the position of the threshold. According to this criterion, compounds in the left side were considered safe while those in the right side were considered unsafe. Results from this test can be found in panel B, where the performance of the classifier is evaluated with a 2-by-2 confusion matrix in which columns

("TdP+" and "TdP-") describe the Crediblemeds reference and rows (plus and minus signs) indicate the results of the classifier. Whenever the classifier matched the reference it was called either true positive (TP) or true negative (TP) outcome (top left and bottom right cells in the 2-by-2 table, respectively). False positive (FP) and false negative (FN) outcomes correspond to drugs that were wrongly classified (top right and bottom left cells in the 2-by-2 table, respectively). According to these values, hERG pIC_{50} of 6 and above yielded 22 true positives, 5 false positives, 18 false negatives and 39 true negatives. True positive rate was calculated as the rate of true positive outcomes over the total amount of positive references, while true negative rate was calculated as the rate of true negative values over the total amount of negative references. Finally, the accuracy (A) was calculated as the number of successes over the total amount of compounds (N).

$$sensitivity = TPR = \frac{TP}{TP + FN} \qquad \textbf{Eq. 23}$$

$$specificity = TNR = \frac{TN}{TN + FP} \qquad \textbf{Eq. 24}$$

$$accuracy = A = \frac{TP + TN}{N} \qquad \textbf{Eq. 25}$$

These values indicate how good the performance of a classifier is, and in this case, results showed a 55% sensitivity, an 89% specificity and an accuracy of 73%, with a large amount of false negative outcomes.

To improve these results while summarizing the effect of therapeutic concentrations on selected channels (I_{Kr}, I_{Ks} and I_{CaL}), we developed a new risk classifier that we called Tx and defined it as the ratio of a compound's concentration that produced a 10% prolongation in the APD_{90} or QT (D_{10}) over its effective free therapeutic concentration (EFTPC).

$$Tx = \frac{D_{10}}{EFTPC} \qquad \textbf{Eq. 26}$$

We calculated D_{10} by using our precomputed matrices while EFTPC were already available as part of our 84-drug dataset. Starting from the therapeutic concentrations, we extracted the compound's APD_{90} or pseudo-QT prolongation according to its IC_{50} profile from the matrices. Then, we iteratively and automatically tested multiple concentrations until the 10% prolongation of the corresponding metric was reached, always selecting the closest available in the simulated space. This would lead to concentrations that were either smaller or higher than the EFTPC depending on whether the drug did prolong APD_{90} or pseudo-QT values more or less than a 10% at therapeutic concentrations. Once both D_{10} and EFTPC were available, Tx was calculated using ***Eq. 26***.

As the reader may have already imagined, Tx relates the therapeutic concentrations with the concentrations that provoke a 10% prolongation of either APD_{90} (in single cell models) or pseudo-QT (in the cell strand model). High Tx values indicated that the therapeutic range is much smaller than such concentrations, while values of 1 or below are linked to drugs that exert notable prolongations at the therapeutic range.

We assigned a Tx value to every compound in our dataset and we then evaluated its performance by means of several receiver operating characteristic (ROC) curves. This method evaluates how sensitivity (TPR) and specificity (TNR) evolve while applying several Tx thresholds to classify the entire drug list. Thresholds are defined as the Tx values below and above which all drugs are considered dangerous and safe, respectively. For example, using an excessively high threshold would classify almost any drug as dangerous, leading to a high number of false detections, which in turn would lead to a very low specificity. In contrast, a very small Tx threshold would lead to many drugs being incorrectly classified as safe, resulting in a very small sensitivity. Eventually, a combination of both scenarios exists where a particular threshold attains a compromise between sensitivity and specificity at the cost of leaving misclassified compounds both in dangerous and safe groups. The area under the curve (AUC) of ROC adds up to the parameters that assess the performance of a classifier. AUCs can have values from 0 to 1. A value of 0.5 indicates that the classifier is unable to distinguish between tested groups, and values of 0.9 and above are characteristic of good classifiers.

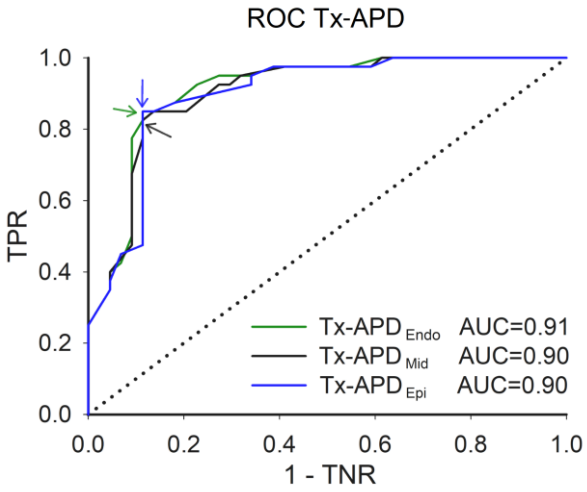

Figure 19. ROC curves illustrating the performance of the Tx-APD assays. Optimal cutoff points where sensitivity and specificity are maximal are indicated with color-coded arrows. Tx-APD cutoffs were 8, 8 and 6.4 for the isolated endocardial (green), midmyocardial (black) and epicardial (blue) models, respectively. A diagonal dotted line indicates the line of equality or random chance. Areas under the curve (AUC) were also included.

Figure 19 shows ROC curves corresponding to single cellular model matrices. We evaluated the performance of Tx for endocardial (green line), midmyocardial (black line) and epicardial (blue line) models. As usual, the sensitivity was represented as a function of "1 – specificity". Colored arrows indicate the corresponding optimal values where sensitivity and specificity are maximal. The dotted line indicates 0.5 AUC. All single cell models showed very similar performance, with very little differences in classified compounds. Optimal thresholds were 8, 8, and 6.4 for endocardial, midmyocardial and epicardial Tx values, respectively, and yielded similar AUCs of 0.91, 0.9 and 0.9 thus getting in the "good classifier" range. Overall, all models were in accordance with each other.

Figure 20 contains the results of applying the abovementioned thresholds to the 84-drug list. Panel A shows Tx values for all compounds grouped by Crediblemeds class. Here, results from single cellular models are represented as filled triangles, squares or circles for endocardial, midmyocardial or epicardial cells, respectively. Vertical lines depict the position of the optimal thresholds. Compounds in the left side of the lines were considered dangerous while compounds in the right side were considered safe. Panel B shows the

confusion matrices resulting from applying the classification criteria. Tx obtained with all models exerted a similar performance with 85% sensitivity, 86% or 89% specificity and accuracies from 86% to 87%. This means that 71 to 72 compounds out of the 84 were correctly classified, leaving 11 to 12 misclassified compounds equally distributed between false positives and false negatives.

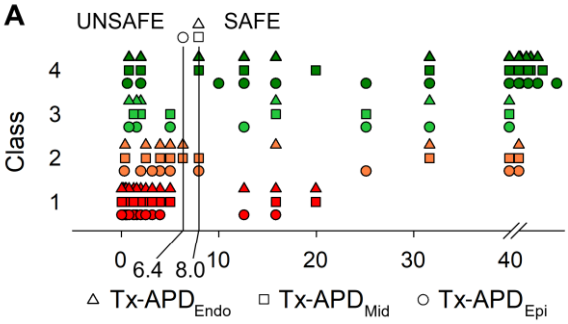

B

Endo		
Tx	TdP+	TdP-
+	34	5
-	6	39
A	TPR	TNR
0.87	0.85	0.89

Mid		
Tx	TdP+	TdP-
+	34	6
-	6	38
A	TPR	TNR
0.86	0.85	0.86

Epi		
Tx	TdP+	TdP-
+	34	5
-	6	39
A	TPR	TNR
0.87	0.85	0.89

Figure 20. Classification of the 84-drug dataset according to the Tx-APD thresholds derived from the ROC curves in Figure 19. A: representation of the single endocardial (filled triangles), midmyocardial (filled squares) and epicardial (filled circles) Tx-APD values grouped by Crediblemends class. Black vertical lines indicate the thresholds separating the two possible outcomes of the test, namely, safe compounds (-) that fall left and unsafe (+) compounds that fall right. B: confusion matrices summarizing the results of panel A. Classes 1 and 2 were considered "TdP+" while classes 3 and 4 were considered "TdP–".

Next, we ought to test whether simulation frequency could alter the results of Tx classification. Instead of performing all the simulations to generate the whole matrices again, we calculated the Tx for every compound, by directly simulating every iteration to get the resulting APD_{90} at two additional pacing

frequencies. We stabilized the model at 0.5 Hz and 2 Hz with a stimulus train of 1000 beats as in the 1 Hz simulation protocol. From this point, we simulated 100 beats after applying drug-induced ion channel block at the indicated pacing rate.

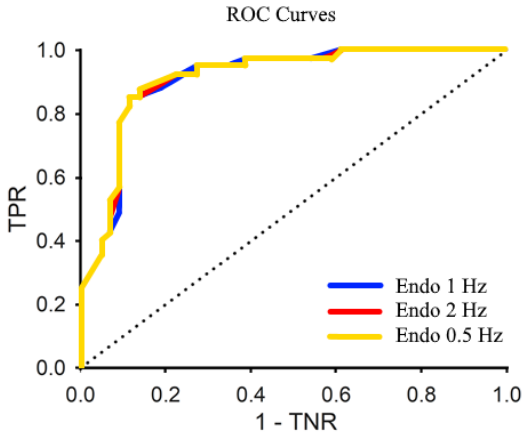

Figure 21. ROC curves depicting the performance of the Tx-APD$_{Endo}$ classifier at 0.5 Hz (yellow), 1 Hz (blue) and 2 Hz (red) pacing frequencies. The effects of the pacing frequency on the ROC curves in the isolated endocardial cell model were explored. The optimal cutoff points were identical at all pacing rates, as well as TPR and TNR. They were 8, 0.85 and 0.89, respectively.

Figure 21 depicts the Tx ROC curves obtained with the isolated endocardial model at three different pacing frequencies, namely, 0.5 Hz (yellow), 1 Hz (blue) and 2 Hz (red).

It shows that there are little differences in their shape, which translate into the optimal threshold of 8 across all tested frequencies. Results show the same sensitivity of 85% as well as 89% specificity. Thus, we concluded pacing rate did not significantly modify the outcomes.

We also evaluated the performance of Tx values obtained using the transmural strand model via pseudo-QT prolongation. Similar to the Tx obtained with single cellular models, a 10% prolongation of the pseudo-QT was used as the reference value to calculate Tx.

Figure 22 describes the classification of the 84-drug list obtained with Tx calculated from pseudo-QT values. Panel A illustrates the ROC curve used to

select the optimal cut-off threshold, which resulted in a Tx of 9.2 and an AUC of a 90%, in agreement with the Tx obtained with cellular models. Panel B represents all compounds Tx values grouped by Crediblemeds.org class, the vertical line highlighting the selected threshold. Finally, panel C shows the resulting confusion matrix, where the test performance lead to an 85% sensitivity, an 89% specificity and an 87% accuracy, parameters that are indeed identical to performance of the Tx corresponding to the isolated endocardial model.

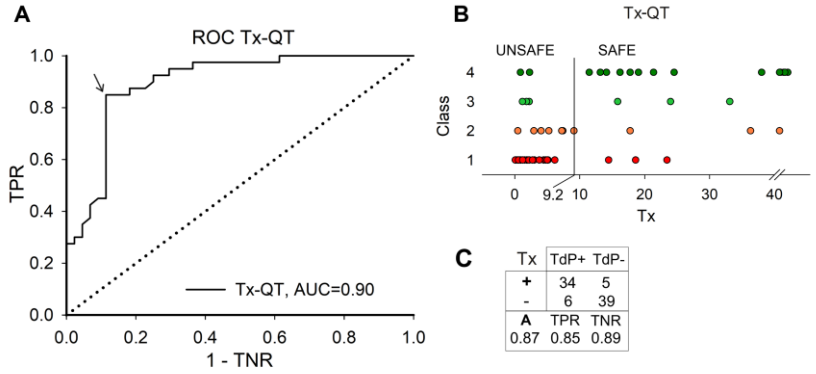

Figure 22. Results of classifying the 84-drug dataset according to the Tx-QT classifier. A: ROC curve describing the performance of the Tx-QT assay at several thresholds. The optimal cutoff point 9.2 was indicated with a black arrow. A diagonal dotted line indicates the line of equality or random chance. The area under the curve (AUC) was also indicated. B: Tx of the dataset. The vertical line corresponds to the optimal threshold calculated in panel A. C: confusion matrix indicating the performance of the classifier.

Figures 23 to 25 contain bar plots representing the values assigned to every compound for several of the classifiers we have tested, namely, hERG pIC_{50} of 6 and above (Figure 23), Tx values obtained with the isolated endocardial model (Figure 24) and with the strand pseudo-QT model (Figure 25). In each plot, we grouped compounds by Crediblemeds.org class and then sorted the compounds by pIC_{50} or Tx value. The horizontal dotted line in the Figure 23 represents the standard classification parameter, where values above the line were considered dangerous and values below were considered safe.

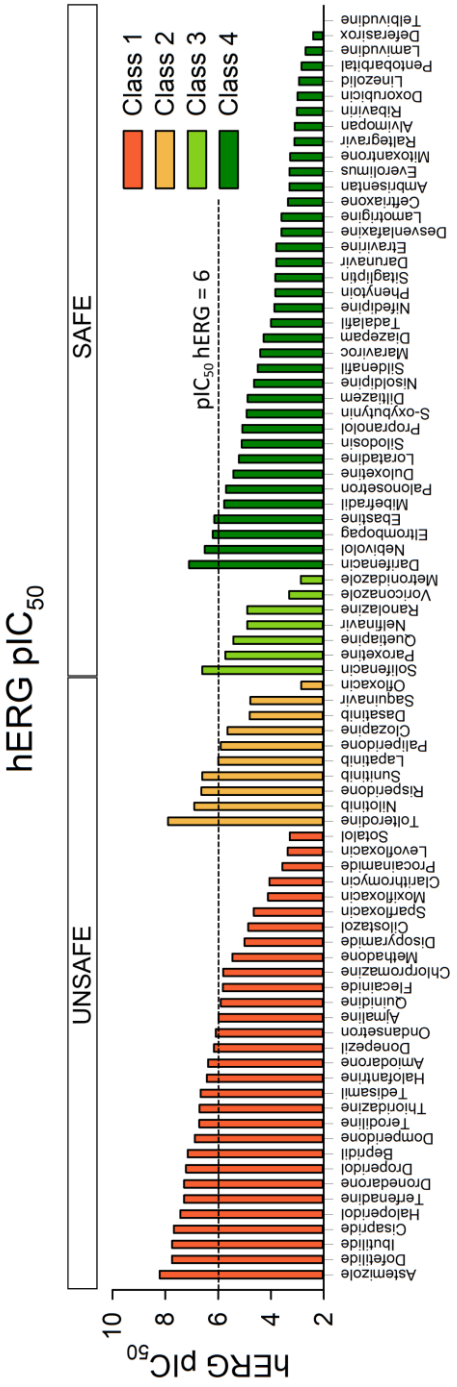

Figure 23. Torsadogenic risk classification of the 84 compounds. The classifiers that we used was pIC_{50} hERG > 6.

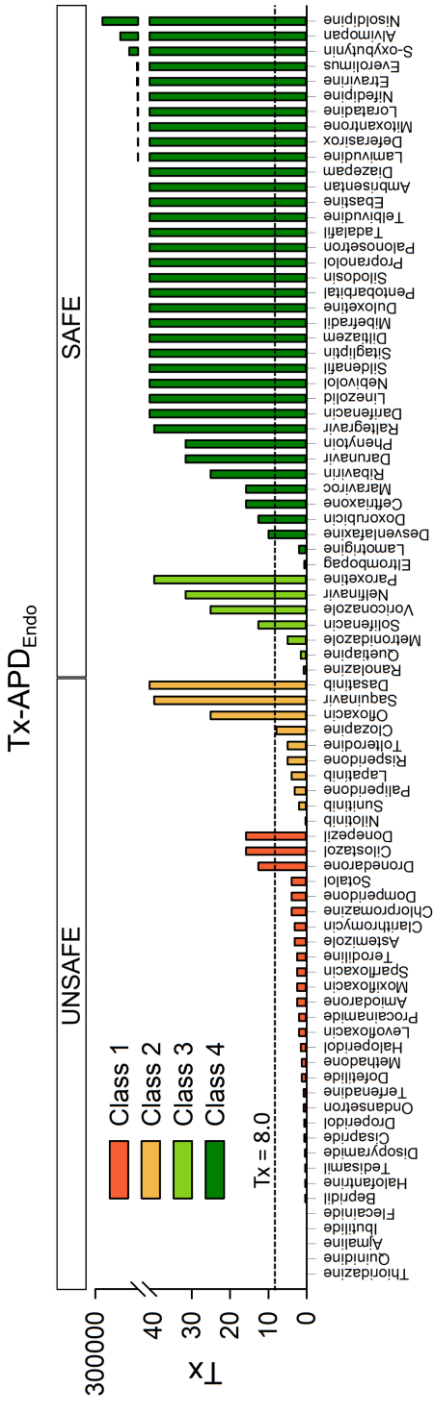

Figure 24. Torsadogenic risk classification of the 84 compounds. The classifiers that we used was Tx-APD$_{Endo}$ < 8.

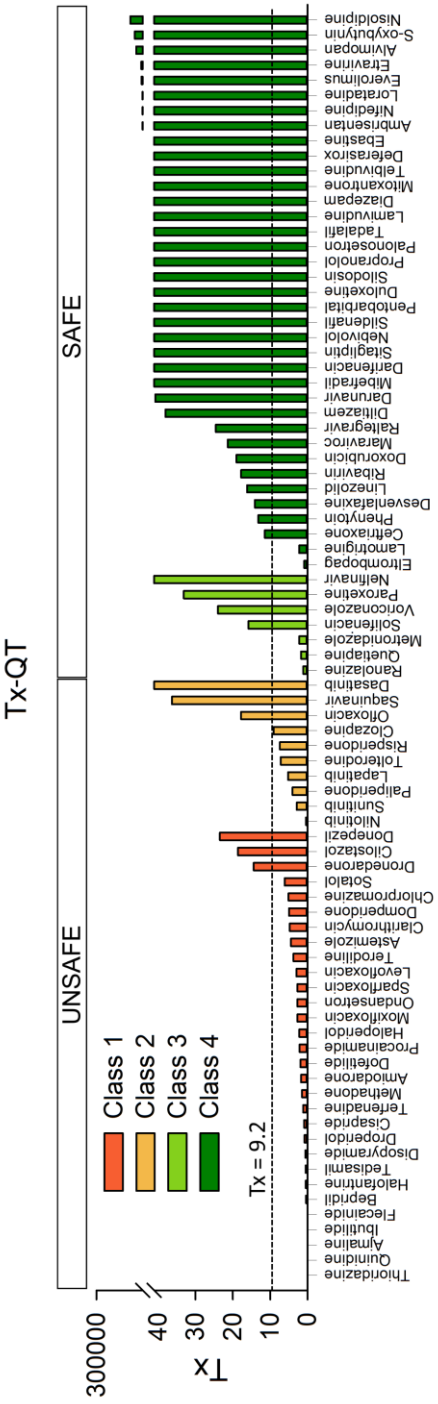

Figure 25. Torsadogenic risk classification of the 84 compounds. The classifiers that we used was Tx-QT < 9.2.

Horizontal dotted lines in Figures 24 and 25 represent the optimal Tx thresholds derived from previously constructed ROC curves. Contrarily to the hERG pIC_{50}, here Tx values above the line were considered safe, while values below were considered dangerous. These plots facilitate the identification of the false positive and false negative outcomes.

Tx obtained whether with single cellular or 1D strand models, misclassified 11 compounds compared to 23 from the standard hERG pIC_{50}. In fact, those compounds were the same when using all models and consisted of class 1 cilostazol, donepezil, and dronedarone, and class 2 compounds dasatinib, ofloxacin, and saquinavir, which were incorrectly considered safe, and of class 3 compounds metronidazole, quetiapine, and ranolazine, and class 4 compounds eltrombopag and lamotrigine, which were incorrectly considered dangerous. Additionally, we assessed the predictive power of the Tx classifier by means of a leave-one-out (LOO) cross-validation procedure. To do so, a number of drug-sets equal to the total amount of drugs was created by removing one of them in each set. We constructed ROC curves for each of the sets and found the optimal cut-off Tx values to finally try and classify the left-out drug (not shown). Results revealed, respectively for QT, endocardial, midmyocardial and epicardial models, values (mean ± SD) for Tx thresholds of 7.91 ± 0.32, 6.33 ± 0.18, 6.31 ± 0.00, and 9.10 ± 0.19, sensitivities of 0.85 ± 0.01, 0.83 ± 0.01, 0.85 ± 0.01, and 0.85 ± 0.01, specificities of 0.89 ± 0.01, 0.89 ± 0.01, 0.89 ± 0.01, and 0.89 ± 0.01, and finally AUCs of 0.91, 0.90, 0.90 and 0.90.

During the LOO cross-validation, the misclassified drugs did not differ from those found previously, with the exception of clozapine, which was sometimes misclassified due to the fact that it is very close to the frontier between safe and unsafe criteria, so that little variations in the optimal threshold could either leave it outside or inside the unsafe group. This happened for every Tx except for the one obtained with the isolated epicardial model. The overall misclassification rate was 14%.

We next built 3D Tx matrices. Figure 26 represents the Tx values of four selected drugs and optimal threshold appears as a blue striped smoothened surface. Axes, disposition and format are similar to , although now Tx values are represented instead of pseudo-QT or APD_{90} intervals. Again, we plotted the positions in space of known proarrhythmic compounds disopyramide (red triangle) and bepridil (red cube) as well as safe drugs raltegravir (green sphere) and phenytoin (green cube). Safe conditions were met when the compounds fell to the right side of the blue striped surface (Tx is greater than the optimal threshold), while unsafe compounds fell to the left side of the blue striped

surface (Tx is smaller than the optimal threshold). Here, the synergy between blocking I_{Kr} and I_{Ks} currents could easily be appreciated due to the way that the surface curves to lower $\log_{10}(D/IC_{50}\ I_{Kr})$ values when $\log_{10}(D/IC_{50}\ I_{Ks})$ values are high. In contrast, the protective effect of I_{CaL} led to the surface curving to higher coordinates for I_{Kr} and I_{Ks} when $\log_{10}(D/IC_{50}\ I_{CaL})$ is high.

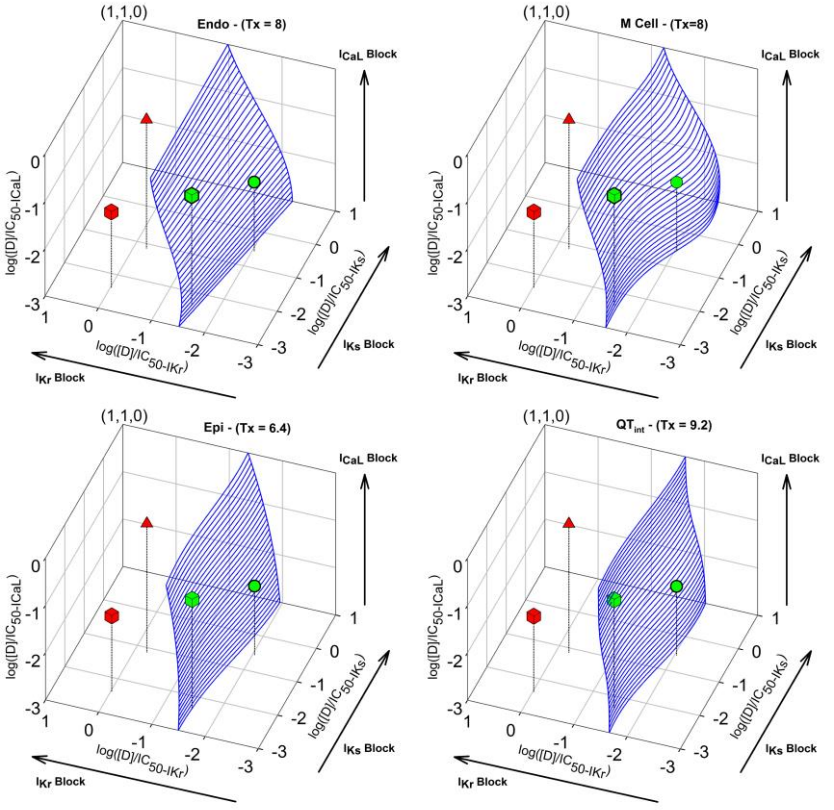

Figure 26. Three-dimensional representation of the surface corresponding to the optimal cutoff values for Tx-APD_{Endo} (top left), Tx-APD_{Mid} (top right), and Tx-APD_{Epi} (bottom left) APD_{90} and Tx-QT (bottom right). Symbols correspond to disopyramide (class 1 drug, red triangle), bepridil (class 1 drug, red cube), raltegravir (class 4 drug, green circle) and phenytoin (class 4 drug, green cube). Coordinate axes represent the logarithmic distance between drug concentration and IC_{50} of each channel ($\log_{10}([D]/IC_{50})$).

3.4 Discussion

3.4.1 Findings

In this section, we studied the effect of a wide range of drug-induced transmembrane ion channel block properties using a wild-type, state-of-the-art, cardiomyocyte and multiple cell strand human model, while also training a new parameter (Tx) meant to provide an easy-to-use tool for drug developers and regulators, capable of giving an early estimation of the proarrhythmic potential of experimental compounds. For that, we created four matrices that can be used as a convenient and quick way to get Tx results without the need of modeling experienced staff. We considered important factors such as multiple ion channel block and therapeutic concentrations. An 84-drug set was used to train Tx by constructing ROC curves using every model and selecting the optimal thresholds. Then, we compared its results to the actual hERG test. Tx improved upon the latter by reducing misclassified drugs by almost a 50% (from 23 to 11 misclassifications) while also showing an AUC of 0.91 with the Tx values obtained with the endocardial cellular model. When using hERG alone, our findings reveal a 55% sensitivity, 89% specificity and 73% accuracy of the $pIC_{50} > 6$ for hERG block in our 84-drug list, which are in agreement with previous works that have shown low performance[58,138].

As we already introduced earlier in this chapter, in a previous paper[127] our group showed that TdP risk prediction could be improved by including the slow potassium rectifier current to the block simulation using a guinea pig action potential model. Mirams and coworkers[65] obtained information about three channels (I_{Kr}, I_{CaL} and I_{Na}) and therapeutic concentrations of certain drugs and simulated their effects using a human ventricular action potential model. They improved the predictions made by Redfern et al. 2003. Their work was leading by including new concepts (multi-channel block and therapeutic concentrations) in the paradigm of proarrhythmicity prediction. In fact, Redfern et al. showed that a safety factor of 30 (calculated as the I_{Kr} IC_{50} over the plasma free therapeutic concentrations) could improve arrhythmic risk prediction in a 52-drug list resulting in 87.5% sensitivity, 68% specificity and 77.4% accuracy). Similarly, a factor of 45 was proposed by Gintant in 2016, although envisioned towards usability during thorough QT studies. In comparison, our factors were smaller (approximately 6 to 10) but showed a similar performance. In 2014, Mirams and coworkers[66] studied the performance of several mathematical models for the TdP assessment using a 31-drug set. They unveiled that the O'Hara-Rudy model of the human cardiomyocytes[98] had the best performance with sensitivity, specificity and

accuracy values of 71%, 100% and 88% when taking into account a wide variety of concentrations (including 100-fold the EFTPC). A recent paper by Lancaster and Sobie[136] showed a that better scores can be obtained (95.9% sensitivity, 81.1% specificity and 89.5% accuracy) in an 86-case list composed of 68 different compounds, some of which were introduced twice by using different data references. In their work, they found that proarrhythmic risk is linked to intracellular calcium transient concentrations as well as action potential parameters. Passini and coworkers[128] based their classifier in the occurrence of repolarization abnormalities (EADs) using a population of models with conductance distributions similar to the human population. They obtained 96% accuracy and 92% specificity in a 49-compound reference list. However, the goal was to discriminate high risk and no risk drugs (TdP classes 1 and 4 in our work), showing slightly different results (89% accuracy and 92% specificity) when considering all risk categories (62 compounds). Dutta and coworkers[107] demonstrated that qNet could correctly classify a 12-compound list distributed in three risk groups.

In summary, we extended previous studies by using a larger dataset while taking into account already well-known factors such as multi-channel block and therapeutic concentrations. Tx showed improved results over the standard method involving solely the hERG pIC_{50}. Its classification results (accuracy of 87%) were similar to each other (endocardial, midmyocardial, epicardial, transmural strand) and also to previous methods by Kramer and coworkers[58] (90.9%), Lancaster and Sobie[136] (89.5%), Passini and coworkers[128] (89%) and Mirams and coworkers[66] (88%), albeit with a larger dataset (84 compounds compared to 55, 68, 62 and 34, respectively).

We selected the state-of-the-art model of the human ventricular action potential at the time of this work to perform our simulations to specifically test drug's proarrhythmicity in humans. Several in silico cellular models have already been used to study drug proarrhythmicity since human cells are very difficult to obtain for modeling purposes. Commonly used animal cellular models for arrhythmicity evaluation include action potential models from dogs, rabbits and guinea pigs[127]. QT studies could be found in rabbit models[69]. In fact, a paper from Beattie and coworkers[69] found that simulating drug effects the rabbit left ventricular wedge to obtain prolongation of the QT yielded a 78% accuracy when predicting the experimental results. Nonetheless, some important differences between cellular models have been revealed, including lack of some currents, such as the guinea pig's absence of rectifier transient outward potassium current (I_{to}) and larger slow component of the potassium

rectifier current (I_{Ks})[139], or the rabbit's larger late component of the sodium current (I_{NaL}) and smaller I_{Ks} with increased basic TdP risk[140].

Our results in proarrhythmicity prediction with the O'Hara-Rudy model[98] indicate that the most important factor is I_{Kr} blockade, dominating the position of the 10% prolongation surface in our 3D matrixes. I_{Ks} blockade influenced APD_{90} and QT prolongations with notably less importance than I_{Kr} blockade, which is consistent with its small amplitude in humans[140] and with other simulation studies[66,98], but its synergistic effect with I_{Kr} blockade can be decisive as the 10% prolongation can be reached much easily by blocking I_{Kr} when I_{Ks} is reduced or absent. Contrarily, I_{CaL} blockade showed a more marked APD_{90} reduction effect, although still weaker than I_{Kr} block. This suggests that effects of pharmacological compounds on I_{Ks} are not as relevant as I_{CaL} or I_{Kr} effects. This is in agreement with a Kamer and coworkers' study[58], where inclusion of I_{CaL} blocking potency did in fact improve the TdP prediction performance dramatically when compared to the hERG assay alone (96.9% sensitivity, 82.6% specificity and 90.9% accuracy).

Our work feeds from the advances achieved by the aforementioned works. We were able to build a prediction tool for companies and regulators to test their compounds in early stages of development without the necessity of qualified staff, since all simulations have already been performed and saved for a wide array of combinations. Compounds for which an estimate of the therapeutic concentrations is available can we directly tested, otherwise, the user can obtain an estimate of a maximum safe concentration for the compound by using our matrices according to its IC_{50} values for I_{Kr}, I_{Ks} and I_{CaL}. Tx notably reduced the number of misclassified compounds compared to the hERG test but there are still compounds that could not be correctly identified and stayed as false positives or false negatives. This comes to show that there are some limitations to this study that must be addressed.

3.4.2 Limitations

The human body is a complex system in constant balance. Most of the drugs we introduce enter the bloodstream after being ingested and are absorbed through the gut. While this is a phenomenon that we could take into account by obtaining peak plasma concentrations and protein bound fractions, there are other mechanisms that play important roles in determining how much of the drug actually reaches the ion channels in the heart and also how much of its effect is actually due to a drug-channel interaction. For example, donepezil is known to downregulate hERG channel trafficking, which contributes to further decreasing the I_{Kr} conductance by reducing the number of channel proteins that

reach the cell membrane[141]. Channels can also be blocked in many ways. For example, Flecainide enters the channel from the cytoplasm side of the membrane, binds low into the pore and gets trapped in it, contrary to other drugs with more direct binding dynamics[142]. Other targets can exist with similar effects to channel blockade in TdP generation. For example, Cilostazol inhibits the PED3 (phosphodiesterase 3), which has been related to increase in intracellular cyclic AMP, calcium unbalance and early after depolarizations[143]. Drugs also transform due to metabolism. While this mechanism is typically responsible for a reduction in compound potency, sometimes metabolites with similar or decreased blocking potency towards the same target can appear. Dronedarone's N-butyl-metabolite has one third of the parent's potency which can also contribute to TdP generation[144]. A particular combination of metabolites for ranolazine was theorized to be the cause of an apparent hERG IC_{50} of 35 μM instead of the more commonly found 12 μM from the literature in a paper by Moreno and coworkers[90]. Additionally, distribution of the compounds throughout the human body can sometimes be complex, meaning that some tissues can be prone to accumulating greater concentrations of the drug than others, such is the case of saquinavir[145]. All these phenomena can interfere with the correct simulation of drug effects. Despite their existence, information about these is scarce and certainly unavailable for some of the compounds that we included in our list. Other misclassified drugs show important effects on ion channels that were not considered in this work, such as lamotrigine, ranolazine and quetiapine, which show interactions with the sodium channel. Finally, it is worth noting that eltrombopag showed high variability of its IC_{50} and its classification was uncertain as there is a lack of strong evidence for placing it in any QT risk category[57].

We selected a large dataset to calibrate Tx because it offers a more realistic scenario where prediction errors can appear. Nonetheless, scarcity of data was patent among many of the compounds we tested and IC_{50} values for I_{Ks} or I_{CaL} were sometimes not available. In these cases, we assumed that interaction with those channels was negligible as in previous studies[65,66]. We also gathered data from various sources whose methods are often very heterogeneous. Protocols can deeply affect the resulting IC_{50}s as can be seen by the variability of the reference data, but major sources of error were screened by selecting mammalian cell lines, consistently discarding data from frog eggs (Xenopus Oocytes). Our approximation to this problem was to consider data as a distribution of values, from which we picked the median (central value) as a way of summarizing all data in one single IC_{50}. By doing so, we ought to avoid extreme values, which are prone to greatly modify the value of the average.

Sodium channel block and, in particular, block of the late component of its slow component (I_{NaL}) has recently been found to greatly affect the action potential duration and shape. In this work, we have not considered I_{NaL} block, which might have contributed to misclassification of several compounds such as ranolazine (see Chapter 4).

To simulate drug-channel interactions, we used the standard simple pore block model through the Hill equation, which also includes a Hill coefficient that governs the slope of the sigmoidal dose-response curve. In our work we simplified the model by assuming all coefficients as 1, based on the studies that suggested that using hill coefficients could give little benefit[15,16,31].

Binding kinetics were not taken into account although they have been found to play an important role in differentiating safe from unsafe drugs[146]. Complete drug-channel interaction state models are available only for a few well-studied compounds and often require complex testing and simulation.

Our TdP risk classification reference comes from Crediblemeds, which relies on clinical data to give a 1 to 4 class to each of the compounds that it includes. Nevertheless, as proven by Wisńiowska and Polak[147], a number of compounds have already been classified by several methods with varied results, which raises the need of a common classification protocol. Amiodarone, clarithromycin, clozapine, domperidone, donepezil, lapatinib, moxifloxacin, or ranolazine are among the compounds that show inconsistencies in their classifications by different methodologies.

In our work, we decided to binarize the classes to safe or unsafe compounds. Recently, the paradigm has shifted towards classifiers that are able to quantify more or less the TdP potential of drugs, being able to at least show three classes, namely, low, intermediate and high risk[148]. We did not account for TdP risk levels, but the nature of Tx does not make it impossible to show better risk stratification in a possible future iteration.

3.4.3 Implementation

There were several requirements to implement the approach to modeling we covered in this chapter. First, general knowledge about pharmacokinetics/pharmacodynamics were necessary to calculate EFTPC values when they were not provided directly. These could be derived from other parameters such as dosage, C_{max}, molar mass and protein-bound fraction. Second, programming skills were necessary to write and automatize the required code, as well as to retrieve the results and analyze the large amount of data. The initial implementation investments consisted of bibliographic

research and code writing and preparation. Pharmacokinetics/pharmacodynamics data are usually obtained during clinical testing to refine the range of therapeutic concentrations, which makes it more readily available for research. Code writing and preparation during the initial phases is time-consuming, but some parts can be re-used due to the repetitive nature of the simulations. Our objective was to generate matrices covering a wide range of drug effects on three ion channels. The simulations that we performed to obtain the matrices were the limiting factor during their generation and took most of the initial implementation time. To speed up the process, we parallelized the required simulations in a cluster with several computing cores. Nevertheless, when simulations are complete, testing new compounds on the model becomes very fast, as the user does not need to wait for the simulations to be over.

As for the reusability and expandability of the code, this is highly modular approach that allows for easy and fast modification of some components. For example, simulations can be performed for four channels instead of three by including an additional parameter indicating drug block for an additional channel. Likewise, more parameters can be extracted from the already available simulations by further analyzing the action potential time courses, such as APD_{50}, maximum upstroke velocity or specific ion current time courses, among others. The cellular action potential model can also be swapped for another version. However, the simulations must be performed again with the corresponding time cost.

All in all, we conclude that the approach that we implemented in this chapter is a modular, easy-to-implement and effective way to study the TdP risk of a wide range of drugs. The initial implementation proved time-consuming, although the upgradability and re-usability of the code makes for a very useful tool with numerous possibilities. As standardized high throughput systems such as Qpatch[66], PatchXpress[108], IonWorks/FLIPR[69] improve their functionality, we could expect more data with higher quality on channel IC_{50}s, which support the use of approaches like this one.

3.5 Conclusions

In this chapter, we have studied a wide range of drug effects using the state-of-the-art human action potential cell and tissue models. Large arrays of APD and pseudo-QT prolongations, combined with an 84-drug set including information about therapeutic concentrations and IC_{50} values for three ion channels (I_{Kr}, I_{Ks} and I_{CaL}), were the means to calibrate a new in silico TdP risk

classifier (Tx) with improved performance over the hERG test, albeit maintaining a reduced complexity. hERG block has unquestionably a high influence on QT prolongation but was accompanied with therapeutic concentrations and two additional channel IC_{50}s to build upon previous works. We confirmed that these parameters are very important in TdP risk classification. In silico models will play an important role in drug safety, as stated by the CiPA initiative[17], and we also contributed creating a more accurate tool for this purpose. We found that, since all four tested models gave very similar results, Tx obtained with the human endocardial isolated cellular model enables TdP risk prediction with good results. Although therapeutic concentrations are not available in early stages of the drug research, a maximum safe concentration could be obtained by analyzing the IC_{50}s of a test compound for I_{Kr}, I_{Ks} and I_{CaL}, giving an estimate of the concentrations that do not unreasonably prolong the APD or QT.

3.6 References of the drug dataset

Table 4. Drug data references. Name (1st column) and references for the IC_{50} values for I_{Kr}, I_{Ks} and I_{CaL} (2nd to 5th column). A dash in the IC_{50} boxes means that no value was found in public databases neither in the scientific literature. The color-coded background of first column corresponds to Crediblemeds' torsadogenic classification: red (Class 1), orange (Class 2), bright green (Class 3) and dark green (Class 4). References are PubMed IDs (PMIDs). Drug labels, where the EFTPC values were obtained, can be visited through provided links.

Name	Ref. I_{Kr}	Ref. I_{Ks}	Ref. I_{CaL}	Ref. ETFPC
Ajmaline	21300721	-	-	21300721
Amiodarone	25127758, 15272206, 21489024, 15936217, 21158687, 11238279, 23812503, 19673885, 10991917, Okada 2015, 22303293, 15541373, 15950494, 18006430, 18587422, 20493497	11238279, 15817093, 15817093, 15817093	21300721	http://dailymed.nlm.nih.gov/dailymed/drugInfo.cfm?setid=b0eb6c22-7553-4e3f-a06d-20a186ced99a
Astemizole	25127758, 15272206, 15936217, 15172012, 21158687, 23812503, 19673885, Okada 2015, 23137660, 18701618, 22303293, 8001268, 21675869, 15740727, 12388285, 15950494, 10376921	-	23812503, 26601174	23812503
Bepridil	9765513, 14975710, 15936217, 19616638, 15172012, 21158687, 15385083, 23812503, 19673885, Okada 2015, 22303293, 15950494, 16843688, 26616666.	9765513, 10588929	14975710, 2420970, 21300721, 19367686	21300721
Chlorpromazine	21158687, 16051556, 23812503, 23137660, Tie 2000/Tie 2002	15071359, 14530219	23812503	21300721
Cilostazol	23812503	23812503	23812503	http://www.accessdata.fda.gov/drugsatfda_docs/label/2015/020863s023lbl.pdf

Name	Ref. I_{Kr}	Ref. I_{Ks}	Ref. I_{CaL}	Ref. ETFPC
Cisapride	14975928, 25127758, 23201772, 9223557, 15272206, 10407390, 15574182, 23103500, 9445174, 11961040, 23651875, 23934164, 14975710, 15306208, 15936217, 19616638, 15172012, 21158687, 15385083, 23812503, Lacerda 2001, 15967876, 15076220, 18034998, 20172036, 9374794, Okada 2015, 12729675, 18701618, 22303293, 11714889, 9395068, 17531263, 21675869, 15740727, 17928736, 10510456, 12388285, 15950494, 18587422, 16843688, Yamazaki 2014	1520765X	15067213, 14975710	21300721
Clarithromycin	12065733, 10219239, 17531263, 14674677	-	-	https://dailymed.nlm.nih.gov/dailymed/drugInfo.cfm?setid=8a56f36f-4e45-43f6-842b-5c2d319aaaec
Disopyramide	[19], 21989164, 23137660, 16842817, 15272206, 11162661, 15950494	[19]	[19]	http://dailymed.nlm.nih.gov/dailymed/drugInfo.cfm?setid=11a68e26-d2e4-48f6-ba0f-9bdd5778f25a
Dofetilide	22391528, 1501123, 21224008, 9501201, 15574182, 23103500, 21489024, Frederiksen 2001, 20071423, 15936217, 15172012, 22074238, 21158687, 8417848, 14711935, 23812503, 14525949, Lacerda 2001, 22609836, 17042915, 18493243, 19673885, 20172036, 25087753, Okada 2015, 12729675, 18701618, 22303293, 9395068, 9694935, 21675869, 8649354, 11927665, 7882490, 26616666, 4722980	21224008	21224008	21300721
Domperidone	15640612, 11034933, 19673885, 15950494	-	-	21883386
Donepezil	23812503	-	23812503	http://dailymed.nlm.nih.gov/dailymed/drugInfo.cfm?setid=11ac01f4-d26e-47b2-9660-d514ab097fdb
Dronedarone	15541373, 21777565	12548079	12548079	https://pubchem.ncbi.nlm.nih.gov/compound/208898#section=Absorption-Distribution-and-Excretion
Droperidol	23812503	-	23812503	23812503
Flecainide	23812503	-	23812503	http://dailymed.nlm.nih.gov/dailymed/drugInfo.cfm?setid=72595783-e6a0-6b7a-f428-9ca03d707794
Halofantrine	23812503	-	23812503	23812503
Haloperidol	19673885, 15076220, 23137660, 12729675, 22303293, 18587422, 16843688, 25127758, 10407390, 11961040, 23651875, 20862641, Frederiksen 2001, 15936217, 19616638, 21158687, 16278312, 15385083, 23812503	-	21300721	21300721
Ibutilide	23812503	-	23812503	https://pubchem.ncbi.nlm.nih.gov/compound/60753#section=Absorption-Distribution-and-Excretion
Levofloxacin	16474415, 20662825, 11125032	-	-	http://dailymed.nlm.nih.gov/dailymed/drugInfo.cfm?setid=8962eb50-3366-1eec-44f9-170e686d2d66
Methadone	23812503	-	23812503	23812503
Moxifloxacin	16474415, 16158069, Thomsen 2006, 19673885, 22289150, 17054943, 16474415, 11040340, 21224008, 11125032, 14512100, 15076220, 18587422.	25087753	23812503, 25087753, Okada 2015	http://dailymed.nlm.nih.gov/dailymed/drugInfo.cfm?setid=71b02da1-3175-1db8-192a-c0a8a6cd98a5
Ondansetron	11046096	11046096	-	http://dailymed.nlm.nih.gov/dailymed/drugInfo.cfm?setid=2edc0788-dc38-4d21-ba8e-71f159e2d3b1
Procainamide	23812503	-	23812503	http://dailymed.nlm.nih.gov/dailymed/drugInfo.cfm?setid=17e47845-daad-434c-a784-6d3875b0d704

Name	Ref. I_{Kr}	Ref. I_{Ks}	Ref. I_{CaL}	Ref. ETFPC
Quinidine	15936217, 21362439, 16842817, 11561091, 18701618, 18587422, 15385083, 21996251, 17042915, 17042915, 17042915, 17042915, Wang, 21224008, 21996251, 17604185, 15172012, 21158687, 15385083, 15385083, 15385083, 12086981, 15950494, 11927665, 19617705, 19617705, 10648647, 15821840, 15821840, 15821840, 12695533, 12695533, 15189761, 10028924	11561091	21300721, 21224008, 12180412	http://dailymed.nlm.nih.gov/dailymed/drugInfo.cfm?setid=11d14362-8f69-4c30-b487-5d05f6462bd7
Sotalol	19673885, 18701618, 18587422, 15385083, 22074238, 23137660, Wang, 21224008, 17604185, 15172012, 15385083, 15385083, 15385083, 16757186, 15821840, 15821840	21224008	21224008	Danda Hilal-Dandan, Laurence L. Brunton, Goodman & Gilman's Manual of Pharmacology and Therapeutics 2nd Edition, McGrawHill. P. 513.
Sparfloxacin	23812503	-	23812503	23812503
Tedisamil	21300721	15579009	-	21300721
Terfenadine	25127758, 9690857, 21224008, 10407390, 10604956, 15574182, 16782359, 11961040, 14975710, 20071423, 15936217, 15172012, Helson 2012, 21158687, 16278312, 15385083, 23812503, Lacerda 2001, 17042915, 22300168, 19673885, 15076220, Okada 2015, 23137660, 12729675, 18701618, 22303293, 9395068, 8001268, 21675869, 15740727, 12388285, 15950494, 18587422, 16843688	1520765X	14975710, 21300721, 21224008, 9242181	23812503
Terodiline	19673885, 21158687, 17110801	10454521	10454521	7830238
Thioridazine	15936217, 19673885, Tie 2000/Tie 2002, 16051556, 12176106, 15385083, 23137660, 17056009, 16278312, 21224008, 11961040, 21158687, 15950494.	10027867, 21224008	21300721, 21224008	21300721
Clozapine	11961040, Frederiksen 2001, 19616638, 21158687, 23812503, Tie 2002	-	23812503	http://dailymed.nlm.nih.gov/dailymed/drugInfo.cfm?setid=d5c8a456-6f3c-4963-b321-4ed746f690e4
Dasatinib	25087753	25087753	25087753	25087753
Lapatinib	25087753	25087753	25087753	http://dailymed.nlm.nih.gov/dailymed/drugInfo.cfm?setid=63319b01-cad6-4d0a-c39b-938fa951a808
Nilotinib	25087753	25087753	25087753	20807552
Ofloxacin	11125032	-	-	https://dailymed.nlm.nih.gov/dailymed/drugInfo.cfm?setid=1d19a6db-6da5-e7de-f929-2d18bdfa2cf5
Paliperidone	25087753	25087753	25087753	http://dailymed.nlm.nih.gov/dailymed/drugInfo.cfm?setid=9089db76-aa50-417d-bf62-3674df161e9a
Risperidone	19673885, 12775973, 12176106, 14975710, 21224008, 11961040, 21158687, 15950494.	1520765X	14975710, 23812503, 21300721	15496222
Saquinavir	23812503	-	23812503	http://dailymed.nlm.nih.gov/dailymed/drugInfo.cfm?setid=c00d1607-ac36-457b-a34b-75ad74f9cf0a
Sunitinib	25087753	25087753	25087753	http://dailymed.nlm.nih.gov/dailymed/drugInfo.cfm?setid=43a4d7f8-48ae-4a63-9108-2fa8e3ea9d9c
Tolterodine	25087753	25087753	25087753	http://dailymed.nlm.nih.gov/dailymed/drugInfo.cfm?setid=2cad3579-d197-4019-ae94-460525b6a8d9
Metronidazole	23812503	-	23812503	http://dailymed.nlm.nih.gov/dailymed/drugInfo.cfm?setid=a9987047-9c99-45a5-829b-ae8b189cbfd4
Nelfinavir	25087753	25087753	25087753	https://pubchem.ncbi.nlm.nih.gov/compound/64142#section=Pharmacology-and-Biochemistry

Name	Ref. I_{Kr}	Ref. I_{Ks}	Ref. I_{CaL}	Ref. ETFPC
Paroxetine	23812503	-	23812503	http://www.accessdata.fda.gov/drugsatfda_docs/label/2014/020031s071,020710s035lbl.pdf
Quetiapine	12176106, 21158687	-	21300721	16390352
Ranolazine	15302796, 23010360, Okada 2015, 18520952, 15950494, 19592609	15277312	15277312	http://dailymed.nlm.nih.gov/dailymed/drugInfo.cfm?setid=8d442b8c-97a8-40a9-8603-f9cd0542cedc
Solifenacin	25087753	25087753	25087753	http://www.accessdata.fda.gov/drugsatfda_docs/label/2013/021518s016lbl.pdf
Voriconazole	23812503	-	23812503	http://www.accessdata.fda.gov/drugsatfda_docs/label/2015/021266s038,021267s047,021630s028lbl.pdf
Alvimopan	25087753	25087753	25087753	http://dailymed.nlm.nih.gov/dailymed/drugInfo.cfm?setid=77a67dc6-35d3-48ff-9d18-292d4d442f70
Ambrisentan	25087753	25087753	25087753	20807552
Ceftriaxone	23812503	-	23812503	http://dailymed.nlm.nih.gov/dailymed/drugInfo.cfm?setid=2dd1be9e-74cc-48e8-bf02-f34a78d80fda
Darifenacin	25087753	25087753	25087753	20807552
Darunavir	25087753	25087753	25087753	20807552
Deferasirox	25087753	25087753	25087753	20807552
Desvenlafaxine	25087753	25087753	25087753	25087753
Diazepam	23812503	-	23812503	23812503
Diltiazem	23812503	-	23812503	http://dailymed.nlm.nih.gov/dailymed/drugInfo.cfm?setid=d6a81f9f-3a51-4e86-aeb3-8352186b3528
Doxorubicin	19703166	19703166	-	https://pubchem.ncbi.nlm.nih.gov/compound/31703#section=Absorption-Distribution-and-Excretion
Duloxetine	23812503	25087753	23812503	17380590
Ebastine	9103502, 19673885	9103502	-	15752381
Eltrombopag	25087753	25087753	25087753	http://dailymed.nlm.nih.gov/dailymed/drugInfo.cfm?setid=616224ff-a925-4b38-9ca2-00fbf669380f
Etravirine	25087753	25087753	25087753	20807552
Everolimus	25087753	25087753	25087753	http://dailymed.nlm.nih.gov/dailymed/drugInfo.cfm?setid=e082a024-7850-400b-a5c2-2a140612562a
Lamivudine	23812503	-	23812503	https://pubchem.ncbi.nlm.nih.gov/compound/60825#section=Absorption-Distribution-and-Excretion
Lamotrigine	25087753	25087753	25087753	20807552
Linezolid	23812503	-	23812503	http://www.accessdata.fda.gov/drugsatfda_docs/label/2015/021130s030,021131s029,021132s034lbl.pdf
Loratadine	23812503	-	23812503	23812503
Maraviroc	25087753	25087753	25087753	http://dailymed.nlm.nih.gov/dailymed/drugInfo.cfm?setid=a94a9a2b-337b-4c13-8622-fc392194dc21
Mibefradil	23812503	9765513	23812503	23812503
Mitoxantrone	23812503	-	23812503	23812503
Nebivolol	25087753	25087753	25087753	20807552
Nifedipine	22074238, 23812503, 19673885, 19673885, 10924918	10924918	10900233, 10900233, 9098694, 17173968, 9846638, 19367686	2288835
Nisoldipine	14530219	14530219	14530219, 9846638	2054280
Palonosetron	25087753	25087753	25087753	http://dailymed.nlm.nih.gov/dailymed/drugInfo.cfm?setid=bd06f321-bb42-4748-92f3-d59626b540e0
Pentobarbital	23812503	11862331	23812503	23812503
Phenytoin	23812503	21224008	23812503	http://dailymed.nlm.nih.gov/dailymed/drugInfo.cfm?setid=78b38e7b-1460-4adc-b738-320ffa6259c2
Propranolol	21224008, 19616638, 16314852, 23137660, 16150441, 16843688.	21224008	21224008, 21300721	http://dailymed.nlm.nih.gov/dailymed/drugInfo.cfm?setid=2d9d9660-ef3a-4abf-c291-db8d844ff658

Name	Ref. I_{Kr}	Ref. I_{Ks}	Ref. I_{CaL}	Ref. ETFPC
Raltegravir	23812503	25087753	23812503	23812503
Ribavirin	23812503	-	23812503	http://dailymed.nlm.nih.gov/dailymed/drugInfo.cfm?setid=35f99f76-f2ef-4a81-91ff-285419664be3
Sildenafil	25087753	25087753	25087753	20807552
Silodosin	25087753	25087753	25087753	http://dailymed.nlm.nih.gov/dailymed/drugInfo.cfm?setid=a21163d6-e1b9-4490-bce3-751e0823797c
Sitagliptin	23812503	25087753	23812503	http://dailymed.nlm.nih.gov/dailymed/drugInfo.cfm?setid=f85a48d0-0407-4c50-b0fa-7673a160bf01
S-oxybutynin	10991917	10672870	10672870	http://dailymed.nlm.nih.gov/dailymed/drugInfo.cfm?setid=c5950dba-d92b-46a0-993f-af9f9ddb52bf
Tadalafil	25087753	25087753	25087753	http://dailymed.nlm.nih.gov/dailymed/drugInfo.cfm?setid=ebddb745-81f9-4b25-8739-b2886032ed26
Telbivudine	25087753	25087753	25087753	http://dailymed.nlm.nih.gov/dailymed/drugInfo.cfm?setid=0664309d-1342-4a63-ba5f-4b899cdf3bec

Chapter 4. Study and Modeling of a Channelopathy and Testing of Specific Treatments

Cano, J., Zorio, E., Mazzanti, A., Arnau, M. Á., Trenor, B., Priori, S. G., et al. (2020). Ranolazine as an alternative therapy to flecainide for SCN5A V411M Long QT Syndrome type 3 patients. *Front. Pharmacol.* 11, 1854. doi:10.3389/FPHAR.2020.580481.

4.1 Introduction

In previous chapter, we used modeling and simulation to assess drug safety. For that purpose, we created a new biomarker for high throughput early identification of possible proarrhythmic drugs relying on a large volume of high throughput data to train a classifier. The industry already performs ion channel block assays routinely and several high throughput solutions for automatic patch-clamp have already hit the market. This means that IC_{50} data are readily available for many compounds. However, using only one set of IC_{50} data could sometimes be insufficient towards correctly characterizing a drug's interaction with a channel. In a work from our group[149], we demonstrated that IC_{50}s were highly dependent on the drug's binding dynamics.

Conditions that arise from ion channel dysfunctions are called channelopathies[150]. When these affect cardiomyocytes' channels, they alter their electrophysiological behavior and thus pose patients at high risk of arrhythmia and sudden death. Mutations of the genes that code such channels are a common cause of channelopathies, but their effects highly depend on their location in the protein[9,151–153].

Consequently, considering that both drugs and mutations have their particular ways of modifying a channel's electrophysiology, it is natural to conclude that drugs that are not beneficial in some patients might be recommended in others[154]. However, to shed light into this, first we must study the electrophysiological properties of both the drug and the channelopathy in detail.

As we already introduced in 2.6.2.2, Markov models of the ion channels are a useful tool to reproduce ion channel dynamics in great detail. There are many examples of their implementation[90,91,106,155–157], including drug-channel interactions, but their complexity means they are available only in a few well-studied cases.

Herein, in this chapter, we ought to model precise channel-drug interactions by using Markov models. We ought to reproduce a channelopathy and test several treatments with drugs showing similar antiarrhythmic properties. By doing so, we ought to highlight the potential of this approach to assess drug efficacy using modeling and simulation of the cardiac electrophysiology.

4.1.1 Long-QT syndrome and SCN5A V411M mutation

As we introduced in 2.3.2, the long QT syndrome (LQTS) is characterized by an exceptionally large elongation of the QT segment of the ECG, which is

caused by electrophysiological abnormalities in the cardiac tissue. These abnormalities increase the chance of syncope and lethal arrhythmias like Torsade-de-pointes[158–160], possibly triggered by EADs[161] (see 2.4, where we reviewed the subjacent mechanisms). If left untreated, the mortality rate of this condition is around 71%[5]. A patient that showed deafness and QT prolongation and who suddenly died from arrhythmia in 1967 lies among the first cases that have been reported[162]. One of the first attempts to treat the condition was the unilateral ganglionectomy[163], an approach that was intricate and invasive, and that was certainly not exempt of unwanted consequences. Fifty years later, we have now greatly expanded our knowledge about this condition up to the atomic level.

Patients suffering from LQTS can show elongated QT segments corrected by heart rate (QTc), meaning their value is greater than 470 ms or 480 ms in men and women, respectively. The use of QT as a diagnose tool for LQTS is nevertheless insufficient due to the wide variety of QT segment values in the healthy population[164]. A study that explored 18 maternity hospitals and almost 45 thousand white infants revealed an overall prevalence of approximately 0.4‰ (1:2534)[2]. The authors screened infants for seven of the twelve genes known - at that time - to induce LQTS. New mutation sites and new genes have been identified since then. By 2017, fifteen LQTS classes have been discovered (LQTS type 1 to 15) depending on the gene that was affected[9] (See Table 5 for more details). These increase to seventeen provided we include the two syndromes described by Jervell and Lange-Nielsen[5], but they both affect genes that are already considered in the fifteen-subtype classification. This extensive classification of the LQTS shows how a simple parameter can be altered by many factors that will determine which treatment to recommend and which to avoid, as opposed to an all-purpose QT-shortening drug.

Seventy percent of the cases arises from a loss-of-function of one of the potassium rectifier channels (LQTS types 1 and 2), while 5%-10% are due to a gain-of-function of the sodium channel (LQTS type 3), the other ones contributing less than a 1% of the cases each[5,165].Therefore, SCN5A mutations are the third most important cause of LQTS. The incidence of lethal events is higher in this group compared to the other major LQTS types[158]. Furthermore, while those events happen in response to stress in LQTS types 1 and 2, during episodes of elevated heart rate, the LQTS type 3 shows increased incidence at rest[152], which is related to greater sodium current at low pacing frequencies.

Table 5. Subtypes of LQTS. Names (first column), name of the gene containing the mutations (second column) and affected current (third column). Reproduced from Bohnen and coworkers[9].

LQTS type	Gene	Effects
LQTS type 1	LCNQ1	Decreased I_{Ks}
LQTS type 2	KCNH2	Decreased I_{Kr}
LQTS type 3	SCN5A	Increased I_{Na}
LQTS type 4	ANK2	Multiple modifications
LQTS type 5	KCNE1	Decreased I_{Ks}
LQTS type 6	KCNE2	Decreased I_{Kr}
LQTS type 7	KCNJ2	Decreased I_{K1}
LQTS type 8	CACNA1C	Increased I_{Ca}
LQTS type 9	CAV3	Increased I_{Na}
LQTS type 10	SCN4B	Increased I_{Na}
LQTS type 11	AKAP9	Decreased I_{Ks}
LQTS type 12	SNTA1	Increased I_{Na}
LQTS type 13	KCNJ5	Decreased I_{KAch}
LQTS type 14	CALM1	Multiple modifications
LQTS type 15	CALM2	Multiple modifications

Despite more than 400 mutations of the SCN5A gene have been identified so far, only a fraction of them leads to one of several possible main outcomes. These consist of mainly Brugada Syndrome[166], Long QT Syndrome[167], cardiac conduction disease[168] or sick sinus syndrome[169], and other diseases that are not related to cardiac conduction defects. While Brugada Syndrome is caused by a loss-of-function of I_{Na}, LQTS type 3 is caused by a gain-of-function[153] of I_{Na}. Several mechanisms have been identified that lead to an increased I_{Na} activity and that are related to modifications of the channel's dynamics.

For example, the S216L mutation produces a left shift of the activation dynamics, leading to earlier activation which turns to an increased peak amplitude of INa. The R568H mutation produces a right shift of the inactivation dynamics, hampering inactivation which makes the channel remain active for longer, and the A993T mutation slows inactivation, both leading to the same result[170]. Faster recovery from inactivation can also lead to LQTS type 3, as is the case of mutations E1784 K[171] or P2006A[172]. The ΔKPQ[90] mutation shows a combination of faster recovery from inactivation and non-inactivating current. Therefore, there are many mechanisms that can produce seemingly the same phenotype but radically differ in their effect on I_{Na} dynamics.

The V411M mutation of the SCN5A gene, in its heterozygous form, causes an LQTS type 3 with elongated QT segments and episodes of atrioventricular block. It has recently been described in three case-reports[173–175]. Untreated patients reportedly have a high risk of developing severe arrhythmia and Torsade-de-pointes, putting their life at risk[174,175]. Treatment of one of the patients with lidocaine did not produce the expected reduction in QTc, similarly to mexiletine which also showed gastrointestinal intolerance, therefore requiring installation of a double chamber pacemaker[173].

To the best of our knowledge, there is still no Markov model available in the literature for the V411M mutation of I_{Na} and its mechanism has yet to be confirmed. Since electrophysiological characterization of the mutated channel has been already performed in detail[173], it represents a suitable target to model.

4.1.2 The late component of the sodium current (I_{NaL})

The late sodium current has been called by many names, including "persistent", "non-inactivating", "sustained" or "window" sodium current, but these concepts must not be confused[176]. Maltsev and coworkers[75,176] explain in their works that the "window current" results from the crossover of the activation and inactivation curves, where a portion of the channels remain available for activation during the repolarization, and that it cannot account for the whole I_{NaL}. They studied the sodium channel kinetics in single channel mode and discovered that the sodium channel has several gating modes that prevail over different membrane potentials and time scales. The authors found that the late sodium current was determined by opening bursts that lasted a few milliseconds combined with random single openings, although the contribution of the latter was more important. They conveniently called them "bursting" mode and "late scattered" mode, respectively. The former is produced when sodium channels fail to inactivate during phase 0 of the action

potential, while the latter arises from voltage-dependent sudden openings that make for the ultra-slow inactivating dynamics of I_{NaL} in patch-clamp experiments. Therefore, I_{NaL} exists due to a combination of a sub-population of bursting channels, ultra-slow inactivation dynamics, and the "window" current, which is formed by a small reactivation of I_{Naf} during repolarization.

I_{NaL} plays an essential role in determining the restitution of the APD in cardiac cells in normal conditions, which is fundamental for heart rate adaptation[177]. Specific cardiac conditions have been related to altered I_{NaL} dynamics[172,176]. A review by Moreno & Clancy found that during hypoxia, for example as a consequence of heart failure or myocardial infarction, I_{NaL} increases by two to four-fold[51]. This was shown to be a cause of EADs[51]. Trenor and coworkers analyzed the role of I_{NaL} using computer simulations and revealed that cardiomyocyte remodeling induces EADs through increased sodium accumulation and greater APD reverse rate dependence[178], along with calcium overload[172,179]. Since I_{NaL} appears to have different magnitudes depending on the cell type, it can produce a severely increased heterogeneity of the cardiac tissue's electrical properties when altered, leading to an arrhythmogenic substrate[172]. Therefore, I_{NaL} is a fundamental current in both healthy and altered cardiac tissue.

Late I_{Na} is a small current and poses technical problems when trying to measure it. The use of I_{NaL} enhancers such as anemone toxin (ATX-II) is a common practice to increase its amplitude above measurable thresholds. Traditionally, a pulse from negative potentials around -90 mV to around 0 mV would be applied for 200 to 350 milliseconds to completely inactivate the transient I_{Naf}. The remaining non-inactivating current at the end of this pulse would be measured as I_{NaL}[180–183]. However, another approach has recently been used to characterize it. The authors of works using self-AP clamp techniques claimed they are better at capturing the current's dynamics and role in arrhythmogenesis[184–186]. Briefly, cardiomyocytes are paced, and their action potential time course is recorded and saved to later be applied as a voltage command under exposure to I_{Na} blocker tetrodotoxin (TTX), which enables calculation of the time course of I_{NaL} by comparison of the membrane current with and without the drug. This protocol considers the non-equilibrium processes that happen during an action potential such as the "window" current, which cannot be assessed with a simple voltage step, especially during repolarization. Furthermore, the experiments were conducted on ventricular myocytes, which naturally include all the necessary currents, proteins and enzymes that cooperate to produce the normal action potential time course, as opposed to cells transfected with the sodium channel. Therefore AP-clamp

techniques offer more information about the real time course of the current compared to traditional step pulse techniques.

Moreno and coworkers modeled the ΔKPQ mutation[90] using a Markov model of I_{Na}[89]. As the authors suggested in a more recent work[77], their I_{Na} model can be used as a template to create and optimize mutation and drug models. To test the effectiveness of ranolazine on the ΔKPQ phenotype, they substituted the I_{Na} formulations of both the ORd[98] and the Grandi-Bers[97] with Soltis-Saucerman[187] human ventricular action potential models by their own I_{Na} formulation. Then, they computed the action potential time courses in wild-type, mutation and under exposure to therapeutic concentrations of ranolazine.

Figure 27 shows a comparison between I_{NaL} time courses from several in-silico and in-vitro sources (highlighted in red). Panel A shows the I_{NaL} time course resulting from including Moreno and coworkers' Markov model of I_{Na} in the ORd model (A) and the Grandi-Bers with Soltis-Saucerman model (B)[90]. The time course shows a current surge of a few milliseconds which corresponds to I_{Naf}. This current cannot be correctly represented in this figure due to the vast differences in duration and magnitude compared to I_{NaL}. Then, the current decreases to values close to zero and remains in that state during approximately 50 ms. To this state follows a gradual reactivation of the current that culminates in a peak, which corresponds to I_{NaL}'s activation and maximum value, respectively. Finally, the current drops quickly marking the end of I_{NaL}. In panel C, we highlighted the BCL 1000 ms I_{NaL} time course obtained using the ORd model of the human endocardial action potential model[98] among other time courses obtained at different BCLs. In panel D, we highlighted I_{NaL} among the registered currents in guinea pig cardiomyocytes by Horvath and coworkers[184] using self-AP clamp experiments. Panel E shows the results of similar experiments by Hegyi and coworkers[185]. Contrary to panels A and B, I_{NaL} time courses in panels C to E show a smaller slope after the I_{Naf} upstroke that progressively leads to a maximum value (peak I_{NaL}). Then, the current quickly diminishes matching the end of the action potential (not shown). The time course of I_{NaL} in panels A and B shows a current whose effect is focalized on the later portion of the repolarization. However, panels C to E show currents whose amplitude difference between the plateau and repolarization phases is small. Hence, we ought to integrate new self-AP clamp data into the Moreno and coworkers' model of I_{Na} to improve I_{NaL}'s time course, increasing its contribution to the plateau phase and reducing the differences between peak and plateau current amplitudes.

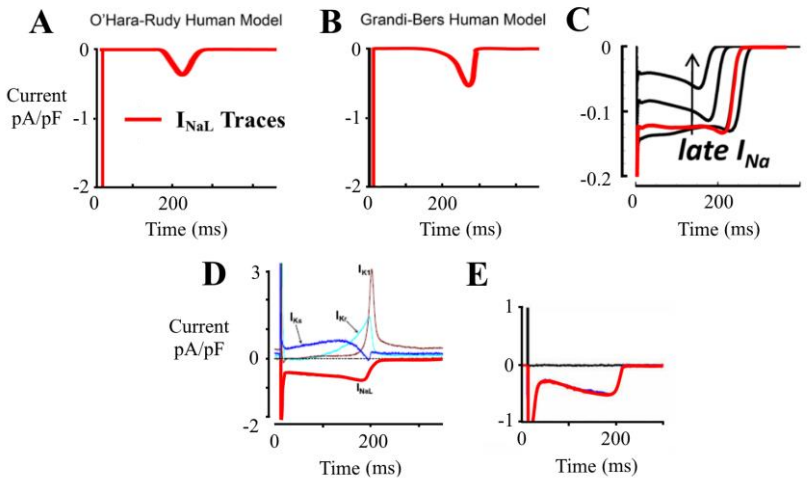

Figure 27. Comparison of in vivo and in vitro I_{NaL} time courses during the action potential. The relevant time courses were highlighted in red. Panels A and B: I_{NaL} time courses of the Moreno and coworkers[90] Markov I_{Na} model in the O'Hara-Rudy model (A) and the Grandi-Bers with Soltis-Saucerman model (B). Panel C: time course of the O'Hara-Rudy model's Hodgkin-Huxley formulation of I_{NaL}. Panels D and E: I_{NaL} time course obtained through self-AP clamp in guinea pig cardiomyocytes from Horvath and coworkers[184] and Hegyi and coworkers[185], respectively. Figures were modified from their original papers[90,98,184,185].

4.1.3 LQTS type 3 therapy

Treatment of the LQTS type 3 with β-blockers was initially not recommended, but a significant albeit incomplete reduction in cardiac events was found[188], especially for nadolol[189]. Despite there is evidence that LQTS type 3 patients could be harmed while treated with β-blockers[190], these remain the first line treatment for LQTS patients[7,191,192]. Given this syndrome is characterized by an increase in I_{Na}, it is natural to think that drugs that specifically block the sodium channel can be useful in treating the condition (see 2.5.1). Among them, ranolazine, flecainide, lidocaine and mexiletine are examples that have already been used clinically in LQTS treatment[173,193–196]. As we have already explored in 4.1.2, the sodium current shows two components (I_{Naf} and I_{NaL}) resulting from different modes of the same channel[75] which can be specifically targeted by sodium channel blockers (see 2.5.1) that have a preferential binding to certain conformations of the channel[197]. This makes sodium channel blockers

suitable since they apparently target the same channel but show different effects. The effects of the abovementioned I_{Na} blockers will be reviewed below.

Mexiletine's effects on LQTS type 3 have been tested in 34 patients[193]. Thirteen of them showed symptoms derived from their prolongation of the QTc before receiving the drug. During treatment with mexiletine, almost all of them (33) showed a reduction in QTc and 10 out of 13 were symptom-free. This supports the fact that I_{Na} block induced by mexiletine can prove useful in LQTS by reducing QTc prolongations. Nonetheless, the cohort population was not uniform, combining infants and adults and several mutation loci, avoiding further conclusions due to a lack of detail about the mechanisms that enhance I_{Na} in each patient. In a case-report, mexiletine was administered in a patient carrying the heterozygous V411M mutation[173]. According to the authors, mexiletine was unable to attenuate their patient's QTc prolongation.

Researchers used lidocaine in 25 patients and gathered data about their ECG parameters in an attempt to unmask possible LQTS type 3. The 9 patients who possessed the malignant mutation E1784K showed a greater reduction of the QTc than their wild type variants. However, the small population calls for further research to confirm its usefulness[196]. In another work, a patient with the I1768V mutation, which increases I_{NaL}, was administered lidocaine and resulted in a successful reduction in QTc[198]. This indicates that lidocaine could be helpful in treating this mutation's phenotype, but they were unable to determine the subjacent mechanism was due to a lack of electrophysiological characterization. Similar to mexiletine, lidocaine did not prove beneficial in the treatment of a patient carrying the heterozygous V411M[173].

Ranolazine was tested in a long-term clinical evaluation in 8 patients carrying the D1790G mutation increasing I_{NaL} and thus prolonging the QT interval[194]. It resulted in a significant decrease in QTc without causing Brugada syndrome[194]. Ranolazine is a relatively new antiarrhythmic (class IB) useful in treating angina[130]. Although it is still being tested, its usefulness in treating patients carrying the SCN5A D1790G mutation suggests it could be useful in other LQTS type 3 patients. However, it has yet to be tested in patients with the V411M mutation.

Flecainide has proven its effectiveness in treating cardioversion and maintaining sinus rhythm in atrial fibrillation[199] since its commercialization in 1982, due to its selective block of the sodium channel. Flecainide's effects were tested in 30 patients carrying the D1790G mutation. It successfully reduced the QTc value in all patients, leaving only 13% above clinically dangerous values, but none of them had cardiac events during the treatment.

The authors conclude that flecainide is a relatively safe treatment for this mutation[200]. Electrophysiological characterization was available for flecainide[201] (as well as for ranolazine[194]) in naïve and in mutation conditions, but the mutation had already been subject of mathematical modeling[202]. However, these results suggest that flecainide treatments could prove beneficial in other LQTS type 3 patients.

While Horne and coworkers[173] did not use flecainide on their patient, they hypothesized it could prove beneficial. Carrasco and coworkers later reported that treatment of a patient carrying the *de novo* heterozygous V411M mutation with a combination of flecainide and β-blockers (propranolol) resulted in a complete disappearance of the LQTS phenotype with no further cardiac events[175]. Blich and coworkers[174], learning from these findings, reported the same results in a very similar patient with the *de novo* mutation. Therefore, there is evidence that flecainide can safely treat the V411M phenotype, although the exact mechanism has yet to be found.

Other I_{Na} blockers such as GS967, F15845 and eleclazine have not yet been tested clinically in LQTS patients, although their effectiveness is currently being tested in vitro[203–206]. This leaves flecainide and ranolazine as excellent candidates to model and test in the presence of the V411M mutation phenotype.

4.1.4 Objectives

To summarize, the V411M mutation of the SCN5A gene belongs to an important group of gain-of-function mutations that can cause arrhythmia and death through increased I_{Na} during repolarization. We ought to create a new model for the mutation to test the effectiveness of an alternative treatment with ranolazine using computational simulations.

To achieve our goals, we split this chapter in three specific stages with specific objectives. First, we ought to create a model of the SCN5A V411M mutation reproducing experimental and clinical data. Second, we ought to update flecainide and ranolazine models to account for new discoveries. Finally, we ought to evaluate the effects of both drugs on the mutation dynamics and provide insights on their mechanisms of action. This could explain the beneficial effects of flecainide[174,175] while giving an answer to whether ranolazine could be used as an alternative treatment.

4.2 Materials and Methods

4.2.1 Clinical characterization

Four patients carrying the SCN5A V411M mutation from two channelopathies specialist clinics gave consent to enroll in a study of their condition. The local ethics committee analyzed and approved the study protocol. All patients underwent ECG measurements under exposure to β-blocker treatments with propranolol or nadolol and also in naïve conditions (no treatment). Their mean QTc intervals, corrected with the Bazzet formula, were obtained manually from resting twelve lead ECGs. Raw QT values were calculated using the tangent method[207] in at least three consecutive complexes from lead II. Two consecutive or three nonconsecutive complexes were used to gain accuracy provided the quality of the ECG or the presence of pronounced sinus arrhythmia made it reasonable, never looking for the longest or shortest QT intervals. In order to estimate the prolongation that was attributable to the mutation for each patient we used an online tool (www.QTcalculator.org). The inputs of this tool are the gender, the age and the QT interval and the outputs are the probabilities of the occurrence of that QT interval or a smaller value in control subjects and in LQTS patients. Taking a conservative approach, we selected the QTc value that covered 90% of the values in wild type (control subjects) and made it our wild type control. We utilized this reference value to estimate the prolongation that was attributable to the mutation for each patient.

4.2.2 Models

4.2.2.1 INa model

The Markov formulation of the wild type sodium channel created by Moreno and coworkers[90] was used as a basis to model the dynamics of flecainide[89], as well as ranolazine both in control and mutated channels. Figure 28 describes the structure of the model. The wild type model (black characters) consists of twelve states including one open (O), three closed (C), four inactive (I) and four bursting (B). The latter consist of three bursting closed (BC) states one bursting open (BO) state. Transition velocities between states are indicated on the side of arrows that show the possible transitions. Drugs can bind to specific states of the channel including the closed states, but only the neutral fraction of the drug can bind to the inactive states while the charged fraction can bind to the bursting states. The drug bound models (charged drug in red characters and neutral drug in blue characters) show their own modified versions of the wild type or mutated transition rates. The mutated version of the model can be used by adapting the transition velocities.

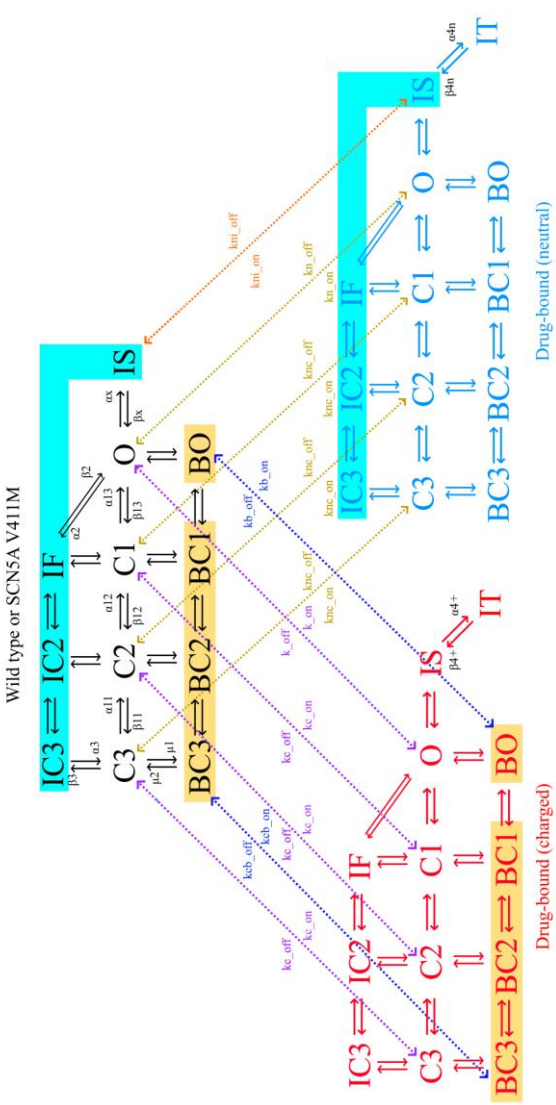

Figure 28. Markov model of I_{Na}. The model contains 36 states, 12 for each of the three drug-free, charged drug-bound and neutral drug bound versions. State transitions are marked with arrows along with their transition velocities. Parallel arrows use the same state transition velocities unless indicated. Charged drug and neutral drug bound models have their own versions of the state transition velocities that are shown in the drug-free model. Blue zones indicate binding and unbinding of the neutral drug to the inactive states. Orange zones indicate binding and unbinding of the charged drug to bursting states. Drug-free states are connected to their drug-bound counterparts through the indicated transition velocities.

This model is appropriate to create a new mutation model while also providing the framework to update both drugs. Therefore, our work started from the unmodified formulations of the Moreno and coworkers' sodium current in wild type[89] and under exposure to ranolazine[90] and flecainide, which was later updated to include bursting mode states[91]. All models were constrained by microscopic reversibility[208].

4.2.2.2 Action potential models

We integrated our particular formulations of the sodium current into the Grandi-Bers with Soltis-Saucerman electrophysiological model of the epicardial action potential, which was modified by Moreno and coworkers to simulate the effects of the ΔKPQ mutation. The authors created the Grandi-Bers with Soltis-Saucerman model by using the "*Soltis-Saucerman model as a template to replace each ionic currents with the Grandi-Bers model except for the L-type calcium channels*" and adjusting I_{CaL} and I_{Kr} conductances[90] (see the reference for more detail). We took this approach because it already constitutes the necessary framework that fit our simulation objectives. This epicardial model was used as a starting point to create two additional cellular models, endocardial and midmyocardial, which we would use later to create the tissue strand model. To do so, we applied scalar factors to several currents, matching the reported differences in conductance[98] (See Table 6).

The sodium current model was inserted twice to account both for wild type and mutated variants. The heterozygous configuration was simulated by including 50% of the former and 50% of the latter during simulations.

In Chapter 3, the Tx biomarker showed very similar results for endocardial and tissue strand models. The reason was that the prolongations that we registered in both models under exposure to the same drug set were very similar. Bearing this in mind and in order to reduce the computational demand of an already intensive workload, we used the endocardial APD_{90} prolongation as a surrogate value of the QT interval prolongation. Later, the QT prolongation was measured using a one-dimensional tissue model and compared with the reference.

The numerical method used to update the membrane potential was forward Euler. State occupancy probabilities in the sodium channel Markovian model were calculated by an implicit Trapezoidal numerical method. Unless specified, the models were paced at a 1 Hz rate, which is widely used in human cardiomyocyte simulation (as we did in Chapter 3) in the absence of β-adrenergic stimulation. These conditions would be equivalent to the exposure to a β-blocker drug.

A stimulus of 9.5 pA/pF and 5 ms duration of inward current was applied to trigger the depolarization.

Table 6. Scalar factors that were applied to current conductances to create midmyocardial and epicardial cell models. First column: conductance name. Second column: midmyocardial to endocardial relationship. Third column: epicardial to endocardial relationship.

Conductance	Midmyocardial	Epicardial
G_{Kr}	0.75	1.1
G_{Ks}	1.4	1
G_{CaL}	1.80	1.10
G_{NaK}	0.70	0.90
G_{to}	3	3
G_{K1}	1.3	1.2
G_{NCX}	1.4	1.1
G_{NaL}	0.9	0.6

4.2.2.3 Tissue strand model

We used a version of the tissue strand model provided by Moreno and coworkers[90]. We modified the model to include the same features as the model we used in Chapter 3, namely, we included three layers of 60, 45 and 60 endocardial, midmyocardial and epicardial cells[98] instead of the linear increase of G_{Kr} from endocardial to epicardial cells proposed by these authors. We placed virtual electrode 2 cm away from the epicardial end of the fiber to measure the ECG with the reaction-diffusion equation introduced in 2.6.4.

The integration method was Forward Euler with a fixed time step of 0.005 milliseconds due to the asynchronous activation of the 165 cells.

The strand model was paced in the absence of β-adrenergic stimulation, as the cellular models, at 1 Hz. A stimulus of 400 pA/pF and 0.5 ms duration of inward current was applied to the first endocardial cell to trigger its depolarization.

4.2.3 Optimization of the I_{Na} models

4.2.3.1 Optimization strategies

The complexity of mathematical models carrying a large number of unknown parameters, and specifically Markov models of ionic currents, makes nearly

impossible to manually find a combination that gives satisfactory results for all the channel dynamics. Therefore, automated search algorithms make of a very useful solution to this problem[209]. However, there are many strategies available in the literature to approach the parameter estimation problem, such as principal axis fitting[210], simulated annealing[211], maximum-likelihood estimation[212], particle swarm optimization[213,214] and genetic algorithms[215–217].

Automatic optimizations consist of algorithms that search to minimize a value determined by a cost function while progressively modifying the parameters that they are given. Naturally, the search space has the same number of dimensions as the number of parameters to be adjusted, thus increasing the complexity of the problem exponentially per additional parameter. A common challenge to these algorithms is that they often find a local, rather than global, minima of the cost function. To circumvent this problem, particle swarm optimizations and genetic algorithms rely on running several identical optimizations in parallel and considering the cost function spatial evolution, therefore taking a wider approach to the problem. However, this comes also with a high computational demand that can rend complex problems impossible to solve in an affordable time. Moreno and coworkers implemented the Nelder & Mead[218] direct search method, and used it to optimize their SCN5A wild type, drug and ΔKPQ mutation models[77,89,90]. This method does not need any information on the cost function derivative[219] while still benefiting from new technologies such as parallelization of the cost function capabilities[77], which speeds its computation considerably. The computational cost of this method is also lower than the other beforementioned strategies because a single parameter set can be optimized without the need of multiple points in the parameter space. Therefore, we chose Moreno and coworkers' methods to perform the required parameter optimizations.

We implemented the necessary code for optimization in Matlab (version 2014b, The Mathworks inc.), including main optimization functions, patch clamp functions, sodium currents and action potential simulation main files. The action potential models were programmed in C++.

4.2.3.2 Optimization protocols

In this Chapter we ought to create a model of the SCN5A V411M mutation using Markov chain models, as well as to test the effects of two treatments. To do so, we started from existing Markov I_{Na} models and progressively modified their parameters to optimize their electrophysiological response to several tests, including in silico patch-clamp and action potential simulations, to bring their results close to in vitro experimental data as well as clinical data from our patients.

First, we optimized the WT I_{Na} model to reproduce experimentally measured electrophysiological dynamics, namely, I_{Naf} steady state availability, activation, recovery from inactivation, recovery from use-dependent block, half-maximum activation Tau, Mean Opening Time (MOT) and I_{NaL} current-voltage relationship. The model was also constrained to reproduce experimentally measured endocardial APD_{90} data at BCLs of 300, 400, 500, 1000, 1500 and 2000 ms. I_{NaL} time course during endocardial simulations was also optimized to reproduce experimental data.

Then, we created a model for the SCN5A V411M mutation by reproducing the experimentally measured WT-to-mutant changes in several electrophysiological dynamics, namely, activation, inactivation, mean activation time constants and current-voltage relationship. These experimental data were taken from the scientific literature. Patient data were used to fit the APD_{90} prolongation produced by the heterozygous mutated phenotype during in silico AP simulations, which were further verified using the transmural strand model to assess QT prolongation.

To test the effects of flecainide and ranolazine on the heterozygous mutation phenotype, we first ought to optimize previously published models of these drugs as follows.

We optimized the flecainide model to reproduce experimentally measured electrophysiological dynamics, namely, I_{Naf} steady state availability, recovery from use-dependent block, and use-dependent block at three pacing rates of 0.2 Hz, 1 Hz and 3 Hz, as well as I_{NaL} IC_{50}. The flecainide-induced endocardial APD_{90} prolongation in WT was assessed during AP simulations, with the aim of matching the clinically observed QT prolongations using it as a surrogate value.

We optimized ranolazine model to reproduce experimentally measured electrophysiological dynamics, namely, steady state availability, tonic block, use dependent block, recovery from use-dependent block and frequency dependent use-dependent block.

Finally, we performed sensitivity analyses of the parameters of our models to reveal the ones that were key for the effects of the V411M mutation and the drugs on the action potential time courses. To do so, we evaluated the impact of each parameter of the V411M mutation individually on the I_{NaL} increment compared to the complete optimized model. In the case of ranolazine and flecainide models, we evaluated the effects of increasing each of their parameters individually by 10-fold on the APD_{90} reduction induced by the baseline drugs.

Full details on the optimization methods were included in the appendix of this document.

4.3 Results

4.3.1 QTc intervals of the patients

In Figure 29, we assembled example traces of the lead II ECGs that were used to measure QTc values for each of the four patients. Of note, the patients were undergoing β-blocker treatment according to the guidelines[7]. The action potential and tissue strand models were paced at 1 Hz, which is consistent to removing β-stimulation, as the formulation of this feature was not utilized in our models.

Table 7 shows the QT interval values calculated from the ECGs along with their corresponding reference wild type values. The average prolongation of the QTc resulted in a 19.9%, with maximum and minimum values of 28.1% and 8.5%, respectively, both belonging to patient four.

Table 7. Detailed QTc measurements. Two samples were taken from each patient under the specified β-blocker treatment.

Patient	Gender	Age (years)	β-blocker	QTc (ms)	QTc leaving 90% of control QTc below (ms)	QTc Increment (%)
1	Male	7 months	nadolol	542	434	24.9
				516	434	18.9
2	Female	29	nadolol	503	437	15.1
				498	437	14.0
3	Female	11	nadolol	555	434	27.9
				528	434	21.7
4	Female	2	propranolol	471	434	8.5
				556	434	28.1
					Average (%)	**19.9**

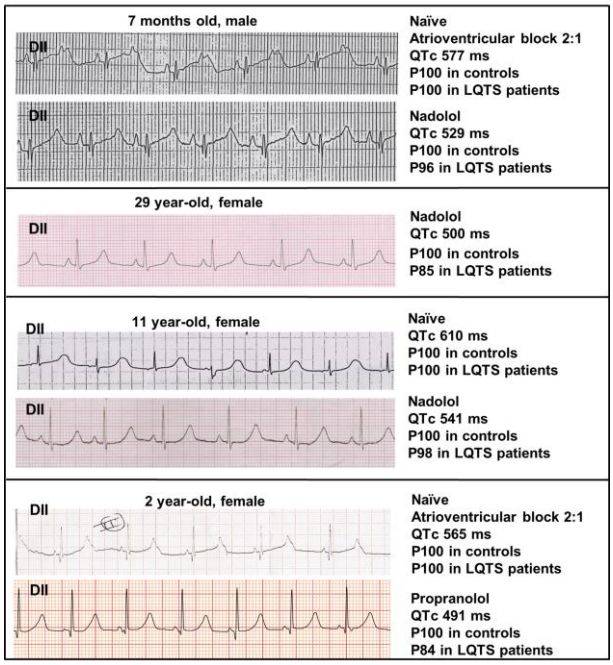

Figure 29. Patients characteristics, ECG traces (lead II) and QTc results. Percentiles of control and LQTS patients to which the QTc values belong are preceded by a "P".

4.3.2 Overview of the optimization program

Figure 30 shows the general flow of the optimizations. Initial parameters are provided to the main function as a vector, along with a vector of seeds for reproducibility. The main function creates a series of jobs in a server requesting as many cores per job as tests are in the optimization protocols, then assigning the optimization launcher function to them. Each job randomizes the parameter vector using the seed that has was assigned to it and launches the optimization by calling the fminsrchbnd function, providing it with the corresponding test batch function. Fminsrchbnd calls the latter to evaluate the performance of the current parameter vector, defined by the addition of its performance scores in various tests.

These include patch-clamp protocols and AP simulations in isolated cardiac cellular models including the I_{Na} formulation. To improve speed, the tests were computed in parallel using Matlab's parallel toolbox, assigning a test to each requested core. Every time the test batch function is called, it returns a score representing the performance of the parameter vector, which is then evaluated

by fminsrchbnd and compared with previous steps in order to modify the parameters towards a combination that could yield better results. When the termination parameters are met, fminsrchbnd stops the optimization and returns a parameter vector containing the parameters that yielded the best results in the parameter history. Otherwise, the optimization continues.

Every test batch function was manually crafted containing the protocols to be reproduced (see Appendix). The function that was in charge of patch clamp tests had the protocols built-in, consisting of a series of voltages and times matching the ones from their respective experimental protocols. The function that launched the AP models was coded in Matlab to manage all necessary commands and files needed to launch a C++ executable containing the AP model. However, both the patch-clamp results and AP time courses were analyzed inside the test batch function following the indications of the reference works, after the required protocols had concluded.

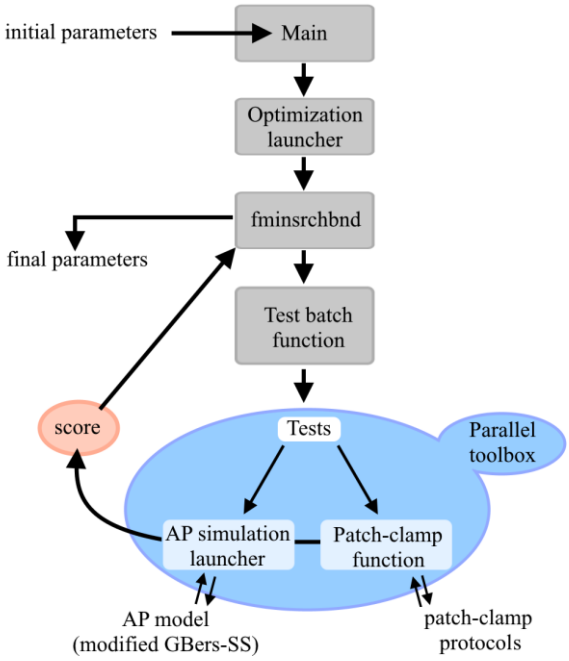

Figure 30. General flow chart of the optimizations. The blue zone indicates the components that were computed in parallel for the sake of speed.

4.3.3 Wild type I_{Na} model

The wild type I_{Na} model was optimized following a two-phase scheme designed to overcome the local minimum derived from previously optimized dynamics, which corresponded to the original Moreno et al. model[89]. It was obtained by introducing first whatever data was new to the model undoubtedly worsening the results in other tests. Then, this would be addressed by re-enabling the original tests.

Indeed, phase one was restricted to the endocardial APD_{90} restitution curve, I_{NaL} time course and current-voltage relationship, all tests bringing new data to the model. We fitted the maximum upstroke velocity to 250 V/s[98]. Once simulations belonging to this phase were completed, the resulting parameters were used again as initial conditions in a second optimization, phase two, where all tests were enabled to refit the original current dynamics.

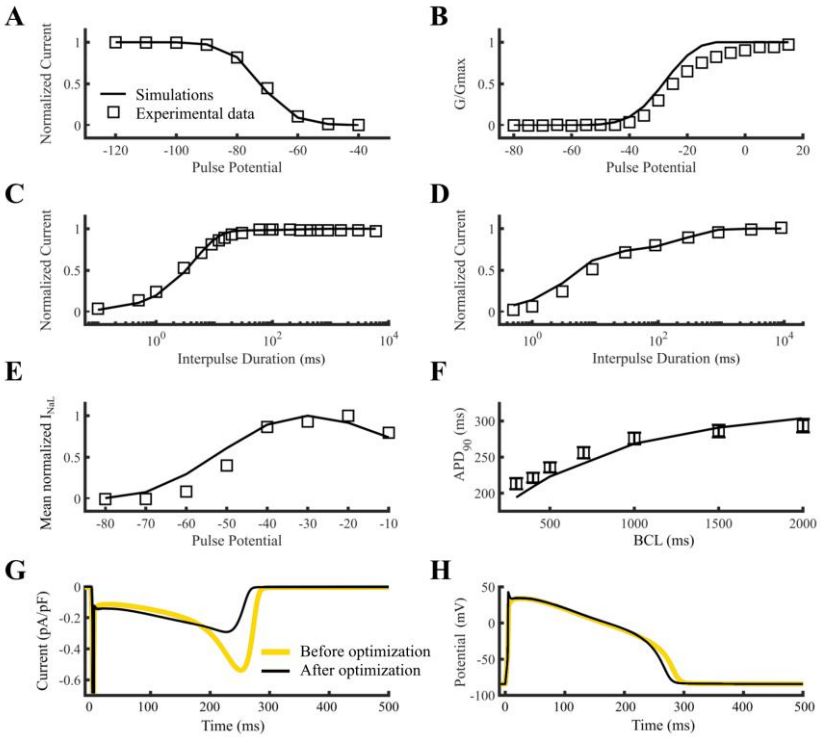

Figure 31. Wild type I_{Na} model optimization results. Steady state availability (A), steady state activation (B), recovery from inactivation (C), recovery from use-dependent block (D), I_{NaL} current-voltage relationship (E) and APD_{90} restitution curve (F). Lines are simulations and squares are target

experimental data (A-F). The time course of the last action potential obtained with the endocardial model elicited by a train of 40 pulses (H) and the corresponding I_{NaL} time course (G). They were obtained with both post (black lines) and pre-optimization (yellow lines) models. In panel G, I_{Naf} was cut in favor of a better representation of I_{NaL}.

Figure 31 depicts the results of the wild type I_{Na} optimization tests for the combination of parameters described in Table 8. In this figure, we compare the best selected optimization results (black lines) to the experimental data (open squares). We also illustrate the action potential time course (panel H) of the last of 40 beats at 1 Hz pacing rate before (yellow line) and after optimization (black line) and the corresponding I_{NaL} time courses (panel F). These panels show that the optimized current exhibits a smaller maximum I_{NaL} around 250 ms after peak I_{Na} compared to the previous formulation, corresponding to the repolarization phase of the action potential, but a slightly greater current during the plateau phase.

Table 8. Parameters of the wild type I_{Na} model. The first and third columns indicate the parameter index as described in Table A.1 (see Appendix), and the second and fourth columns describe their corresponding values.

Parameter	Value	Parameter	Value
p1	$6.59 \cdot 10^{-2}$	**p9**	$1.48 \cdot 10^{1}$
p2	$2.76 \cdot 10^{-1}$	**p10**	3.54
p3	$6.98 \cdot 10^{-2}$	**p11**	$3.81 \cdot 10^{1}$
p4	3.04	**p12**	$2.30 \cdot 10^{-2}$
p5	1.18	**p13**	$3.02 \cdot 10^{-2}$
p6	$8.06 \cdot 10^{-6}$	**p14**	$1.70 \cdot 10^{-7}$
p7	8.43	**p15**	$5.66 \cdot 10^{-4}$
p8	6.45		

This reduced the APD_{90} of the new model but increased the contribution of the current to phase 2 of the AP. I_{NaL} dome was reduced to 0.291 pA/pF, the valley-to-dome current proportion was 48% and the half time proportion was 59.3%. These results are in agreement with the reference experimental data (0.34 pA/pF[107], 59%[184] and 63%[184], respectively). With such I_{Na} characteristics, the endocardial model resulted in APD_{90}s of 194.2, 209, 223.1, 268.6, 290.9 and

303.9 ms for BCLs of 300, 400, 500, 1000, 1500 and 2000 ms, respectively. As can be deduced from the graphics, the results of the tests were satisfactory and in agreement with the reference data, but steady state activation (panel E) was slightly left shifted (10 mV), although the differences are in-line with the experimental data variability (see Figure 32 for a comparison with other experimental sources). Maximum upstroke velocity of the action potential simulations at BCL 1000 ms resulted in 289.9 V/s (not shown). The late to fast I_{Na} proportion was 0.08% (not shown).

4.3.4 Mutation model

The wild type optimization with the new I_{NaL} experimental data created the base model we later modified to reproduce the SCN5A V411M mutated I_{Na}. Here, we ought to incorporate the experimentally observed wild type to mutation changes in dynamics, specifically, shifts and slope alterations in activation, inactivation and current-voltage curves and time constants in addition to the prolongation of the QTc clinically observed. Contrarily to the wild type model, there is no need for several phases since the model was not previously fitted to these dynamics. The V411M optimization was performed in one phase including all tests for a total of 10 seeds.

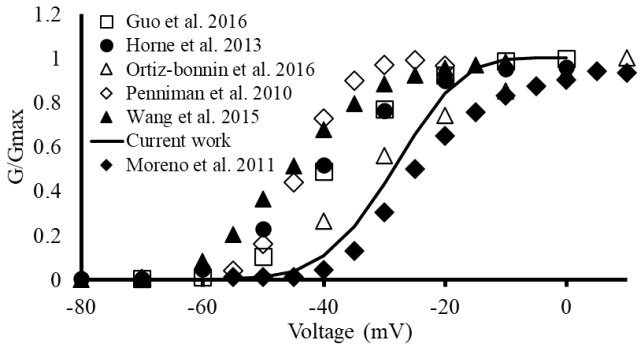

Figure 32. Comparison of the optimized wild type I_{Na} model activation curve (black line) to several experimental sources from the literature (symbols. References in the legend).

Figure 33 shows the results obtained with the selected model of the V411M mutated I_{Na} channel dynamics, whose parameters are described in Table 9. The simulations with the endocardial action potential model, which was set to heterozygous mode, show that the mutation (panel F, red trace) prolonged the APD_{90}, which was 311.5 ms, a 16% prolongation compared to wild type (panel A, black trace). It was caused by an increase in I_{NaL}, whose maximal value

raised from 0.29 pA/pF (panel E, black trace) to 0.75 pA/pF (panel E, red trace) during the repolarization. In panels A to D, we compared the simulation results (black lines) to reference data (open squares) reproducing the experimental changes attributable to the V411M mutation, as well as the wild type model results (black lines). The steady state activation curve (panel B) showed an 8.1 mV left shifted V1/2 compared to wild type, while the steady state inactivation curve (panel C) showed a smaller (6.1 mV) left shift of the V1/2. Both values were successful fits to the experimental data. The inactivation tau (panel D) diminished by halving its value overall, which is most apparent at negative potentials. Current-voltage relationship curves (panel A) showed an increase of the channel's conductance over the -55 mV to -5 mV range doubling and even tripling the wild type values for -40 mV and -35 mV, voltages that are common during phase 3 of the action potential, which explains the increment in I_{NaL} shown in its time course. Taking into account the abovementioned results, we considered that the fit was satisfactory for combining with drug models.

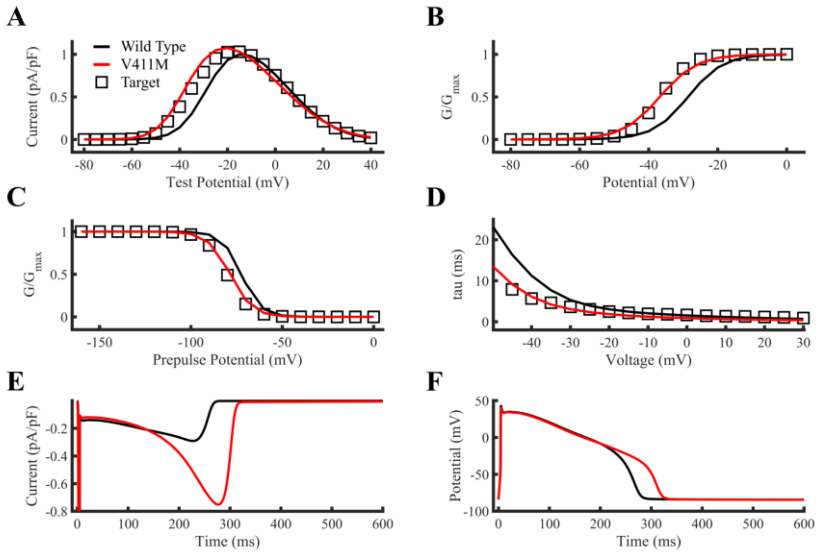

Figure 33. V411M mutated I_{Na} optimization results. The V411M mutated I_{Na} model was optimized using data from Horne and coworkers[173] by reproducing the alterations that the mutation produced to the wild type I_{Na} dynamics and the clinically observed QTc prolongation using the APD_{90} of the endocardial model as a surrogate. The tests consisted of current-voltage relationship (A), steady state activation (B) and inactivation (C), time constant of inactivation (D) and APD_{90} prolongation (F). The I_{NaL} time course (E) was added to illustrate the impact of the mutation on the current,

which explains the increase on the APD_{90} compared to WT. Simulation results (red lines) were compared to target data (open squares) and wild type (black lines).

4.3.5 Flecainide model

We used the Hill formula to both increase I_{K1} by a 51%[220] and reduce I_{Kr} by a 27.7%[221] at 1.5 μM free therapeutic plasma concentrations during simulations with the endocardial cell.

Flecainide's optimizations were divided in three phases sequentially performed. First, the neutral fraction of the drug (less than 1% at physiological pH) was optimized to dose-dependent use-dependent block and recovery from use-dependent block, following Moreno and coworker's methods. Then, neutral drug parameters not allowed to evolve before the second phase, where charged and neutral drug were optimized to steady state availability, recovery from use-dependent block and I_{Naf} IC_{50} use-dependence at 0.2 Hz, 1 Hz and 3 Hz[108]. Phase three added two more tests including I_{NaL} IC_{50} and APD_{90} prolongation in endocardial cells (set to maintain the APD_{90}). Affinities for the channel of the charged drug, but not diffusion, were allowed to change in phases 2 and 3 to account for the new I_{Naf} and I_{NaL} IC_{50}s.

Table 9. Parameters of the V411M mutation I_{Na} model. The first and third columns indicate the parameter index as described in Table A.1, and the second and fourth columns describe their corresponding values.

Parameter	Value	Parameter	Value
p1	$4.71 \cdot 10^{-2}$	**p9**	$1.67 \cdot 10^{1}$
p2	$2.52 \cdot 10^{-1}$	**p10**	7.01
p3	$5.65 \cdot 10^{-2}$	**p11**	$3.16 \cdot 10^{1}$
p4	2.99	**p12**	$2.08 \cdot 10^{-2}$
p5	$2.59 \cdot 10^{-1}$	**p13**	$5.51 \cdot 10^{-2}$
p6	$1.42 \cdot 10^{-5}$	**p14**	$1.70 \cdot 10^{-7}$
p7	9.48	**p15**	$5.66 \cdot 10^{-4}$
8	6.96		

Figure 34 shows the results of the best flecainide optimization, whose parameters are described in Table 10. Reference experimental data (panels A-E: open squares) were compared to simulation results (panel A: filled circles;

panels B-E, lines). Dose-dependent use-dependent block (panel A) and recovery from use-dependent block (panel B) of neutral flecainide showed very similar results to the original work[89], an so did charged flecainide tests, including steady state availability (panel C) and recovery from use-dependent block (panel D) of both charged and neutral flecainide. In panel D, we illustrated wild type results in grey symbols as a reference. I_{Naf} use-dependent block is represented in panel E, showing suitable fits to the experimental data. Panel F shows both the drug-free wild type endocardial action potential time course (black line) and under exposure to 1.5 μM flecainide, which produces a 1.2% increase of the endocardial APD_{90} compared to wild type. Finally, the model scored an I_{NaL} IC_{50} of 1.65 μM following Matsukawa and coworkers' patch clamp protocols[222].

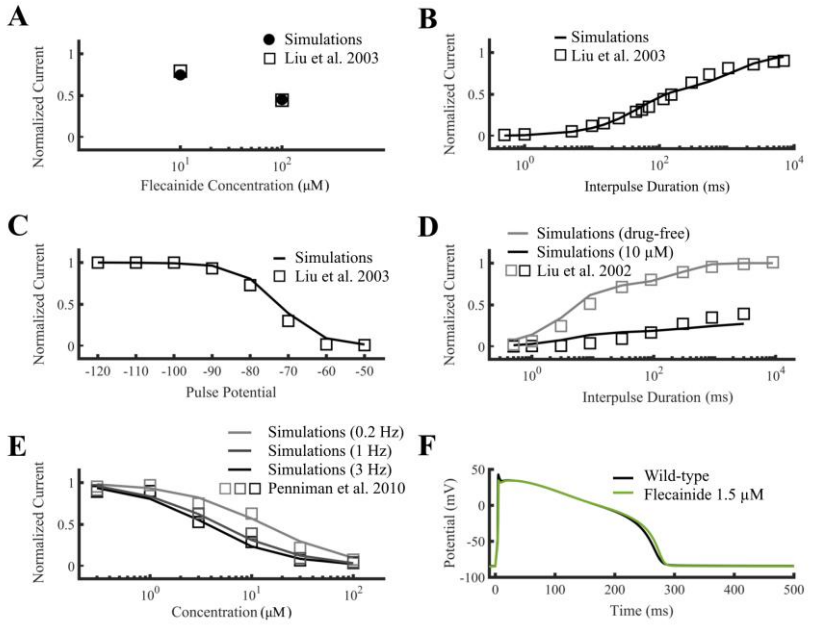

Figure 34. Flecainide optimization results. In phase one, neutral flecainide model was optimized first to dose-dependent use-dependent block (A) and recovery from use-dependent block (B). In phase two, steady state availability (C), recovery from use-dependent block under exposure to 10 μM flecainide (D, black, drug-free conditions were included in grey) and use-dependent block of I_{Naf} (E) at 0.2 Hz, 1 Hz and 3 Hz (light grey, dark grey and black, respectively) were added and both neutral and charged flecainide were optimized. Finally, in phase three, APD_{90} prolongation (F) and I_{NaL} IC_{50} (not shown) were included in the test pool. Filled circles (A) and lines (B-F) are simulations. Squares are target experimental data (A-E).

Table 10. Parameters of the flecainide model. The first and third columns indicate the parameter index as described in Table A.4 (see Appendix), and the second and fourth columns describe their corresponding values.

Parameter	Value	Parameter	Value
p1	$9.72 \cdot 10^{-5}$	**p9**	$1.54 \cdot 10^{-1}$
p2	$2.85 \cdot 10^{-8}$	**p10**	2.49
p3	$1.29 \cdot 10^{-3}$	**p11**	$4.03 \cdot 10^{1}$
p4	$2.93 \cdot 10^{3}$	**p12**	7.07
p5	$8.23 \cdot 10^{-9}$	**p13**	$1.12 \cdot 10^{-3}$
p6	$23.43 \cdot 10^{-7}$	**p14**	$4.30 \cdot 10^{-3}$
p7	3.24	**p15**	$2.15 \cdot 10^{1}$
p8	$3.27 \cdot 10^{-1}$	**p16**	$8.07 \cdot 10^{-1}$

Table 11. Parameters of the ranolazine model. The first and third columns indicate the parameter index as described in Table A.6 (see Appendix), and the second and fourth columns describe their corresponding values.

Parameter	Value	Parameter	Value
p1	$9.08 \cdot 10^{-5}$	**p9**	$1.54 \cdot 10^{-1}$
p2	$2.93 \cdot 10^{-8}$	**p10**	2.49
p3	$1.23 \cdot 10^{-3}$	**p11**	$4.03 \cdot 10^{1}$
p4	$2.92 \cdot 10^{3}$	**p12**	7.07
p5	$8.48 \cdot 10^{-9}$	**p13**	$1.12 \cdot 10^{-3}$
p6	$2.91 \cdot 10^{-7}$	**p14**	$4.30 \cdot 10^{-3}$
p7	3.00	**p15**	25.9
p8	$3.46 \cdot 10^{-2}$	**p16**	$8.03 \cdot 10^{-1}$

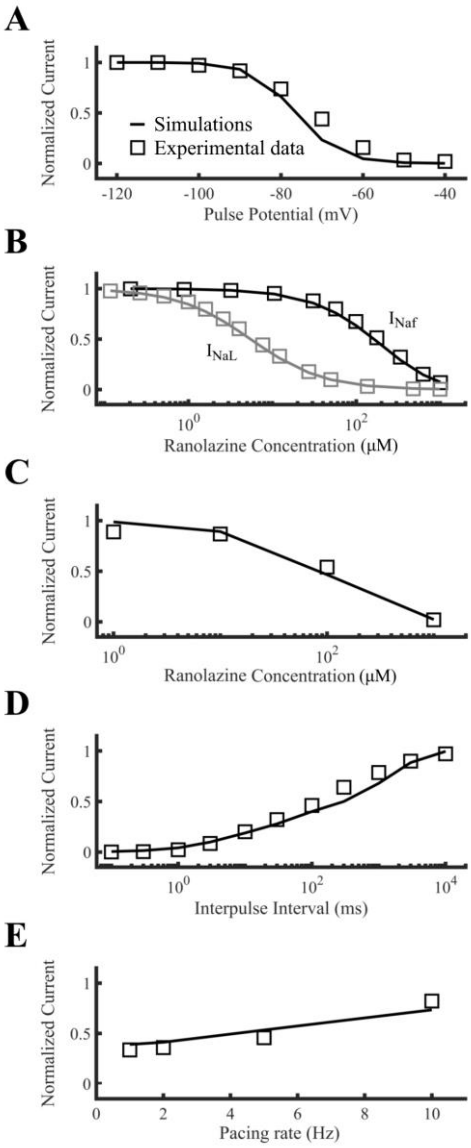

Figure 35. Ranolazine optimization results. All tests were run in parallel in one phase: steady state availability of 10 μM ranolazine (A), tonic block of I_{Naf} (black squares and lines) and I_{NaL} (grey squares and lines) (B), use-dependent block (C), recovery from use-dependent block of 10 μM ranolazine (D) and frequency-dependence of recovery from use-dependent block of 100 μM ranolazine (E). Lines are simulations and squares are target reference experimental data.

4.3.6 Ranolazine model

Ranolazine has shown affinity to sodium as well as for potassium channels. Moreno and coworkers[90] used a model of ranolazine to assess its effects on SCN5A ΔKPQ LQTS type 3. This mutation greatly increases – by five-fold – the proportion of sodium channels in bursting mode, to which the drug shows great affinity. Following the authors methods, we optimized ranolazine to steady state availability, use-dependent block, recovery from use-dependent block, frequency-dependence of recovery from use-dependent block and tonic block of fast and late sodium currents.

Figure 35 shows the results of the best ranolazine model (lines), whose parameters are described in Table 11. Parameters of the ranolazine model. The first and third columns indicate the parameter index as described in , and the second and fourth columns describe their corresponding values., compared to reference experimental data (open squares). In panel A, we evaluated the steady state availability of the channel under exposure to 10 μM ranolazine. Panel B shows the concentration dependence of tonic block of I_{Naf} (black lines) and I_{NaL} (grey lines), IC_{50}s being 153.4 μM and 5.46 μM, respectively. In this panel, open squares represent digitized results from Moreno and coworkers[90] but, due to the scarcity of data regarding these curves, we decided to use the original fitted model to reduce variability. The results are consistent with experimental data from several laboratories. Indeed, Antzelevitch and coworkers[223] obtained IC_{50}s of 296 μM and 6 μM, respectively, in canine ventricular cells. Crumb and coworkers[124] studied ranolazine's effects in 6 ion channels in transfected HEK cells and obtained 7.66 μM for I_{NaL} with no mention for I_{Naf} because it was outside the tested concentrations (upper boundary was of 69 μM). Panel C shows the steady state use-dependence of the channel under exposure to increasing ranolazine concentrations. Panel D illustrates the time course of recovery from inactivation resulting from the same protocol from panel C at 10 μM ranolazine concentrations. Finally, in panel E we show the frequency dependence of block under exposure to 100 μM ranolazine at 1, 2, 5 and 10 Hz pacing frequencies. The results from these tests were all very similar to the original work from Moreno and coworkers[90] and thus were considered them satisfactory.

4.3.7 Differences in flecainide and ranolazine mechanisms of action

Combination of the models was done to assess the effects of flecainide and ranolazine on the V411M mutation. For that matter, we ought to simulate the effects of therapeutic concentrations of both drugs on the isolated cell and tissue strand models. The epicardial and midmyocardial models were manually adjusted (see Table 6 for details on the final conductances) to fit their

respective steady state APD_{90} restitution curves, which were represented in Figure 36 (lines) compared to reference experimental data[98] (open squares + SD bars). The models were brought to steady state as described in methods, by running 300-second simulations at the indicated pacing rates and saving their last action potential for further analysis. The action potentials corresponding to the steady state wild type and heterozygous V411M models, both with or without exposure to flecainide or ranolazine, were examined and represented in Figure 37 to Figure 39. Their corresponding APD_{90}s were introduced in Table 12.

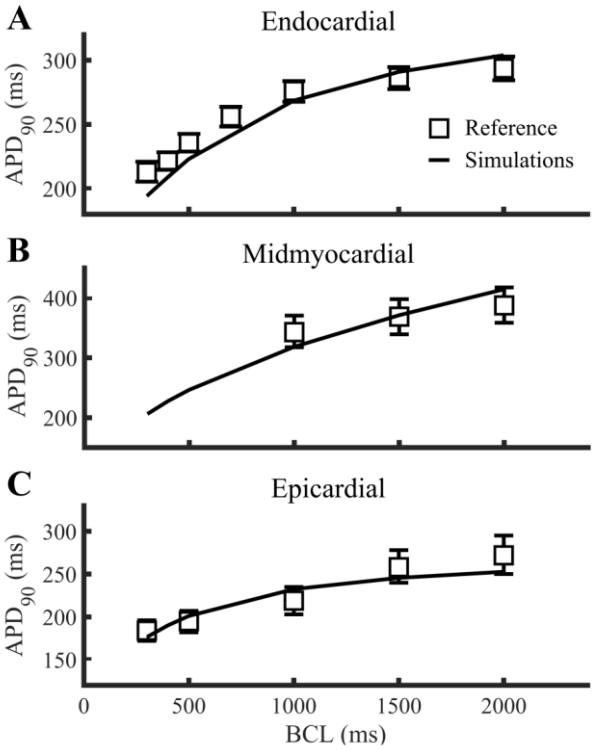

Figure 36. APD_{90} restitution curves of the isolated endocardial (top panel), midmyocardial (middle panel) and epicardial (bottom panel) cellular models in wild type. Simulation results (lines) compared to reference experimental data from O'Hara and coworkers[98] (open squares), represented as mean and SD.

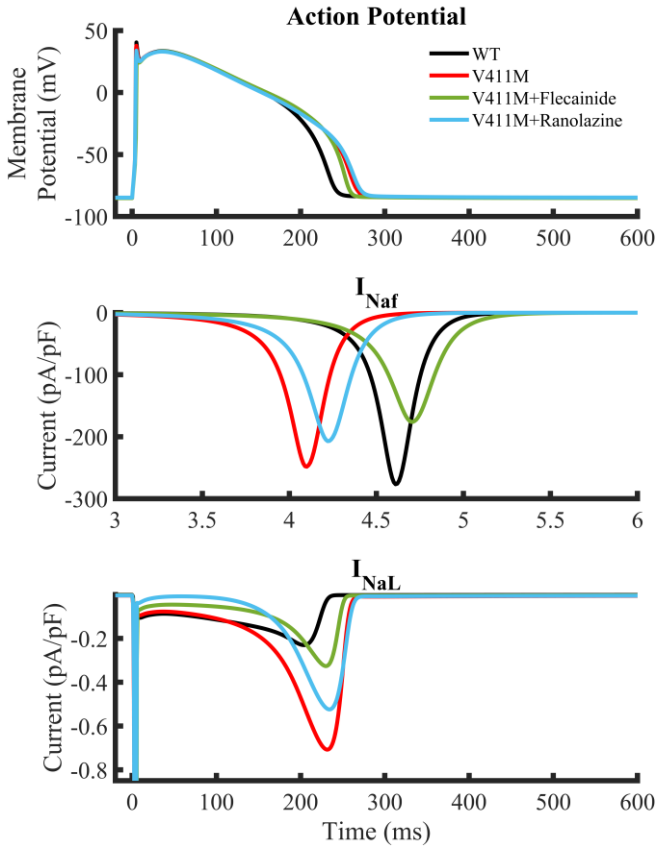

Figure 37. Effects of flecainide (green) and ranolazine (blue) on the heterozygous V411M mutation (red) in epicardial cells. Top panel: Action potential time courses. Middle panel: zoom of the I_{Naf} time courses. Bottom panel: I_{NaL} time courses. The WT action potential was included for comparison (black).

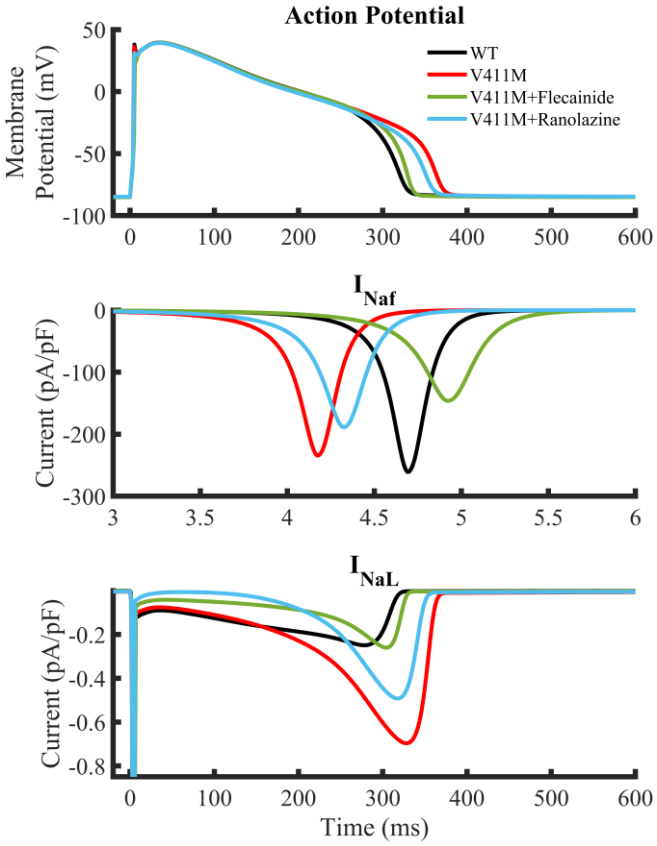

Figure 38. Effects of flecainide (green) and ranolazine (blue) on the heterozygous V411M mutation (red) in midmyocardial cells. Top panel: Action potential time courses. Middle panel: zoom of the I_{Naf} time courses. Bottom panel: I_{NaL} time courses. The WT action potential was included for comparison (black).

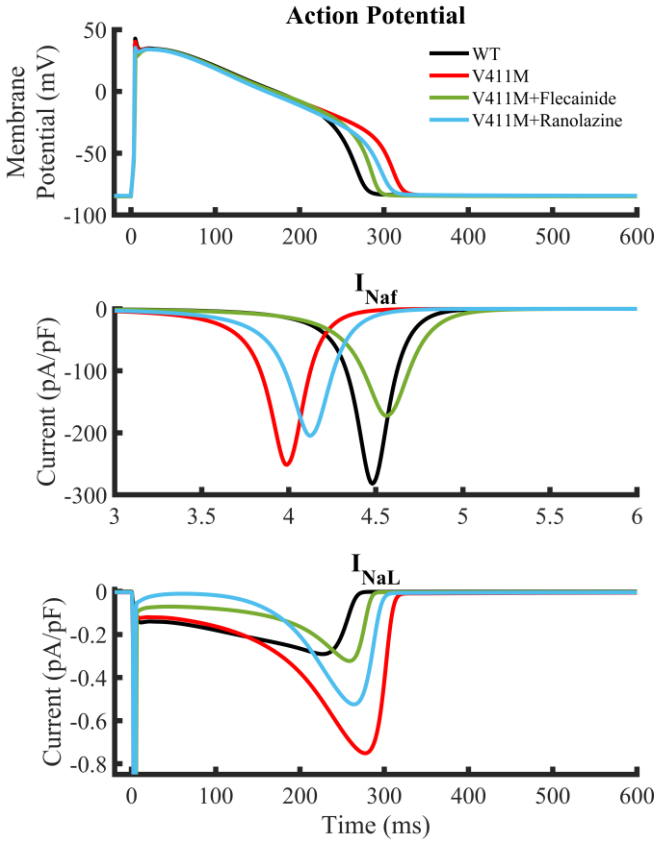

Figure 39. Effects of flecainide (green) and ranolazine (blue) on the heterozygous V411M mutation (red) in endocardial cells. Top panel: Action potential time courses. Middle panel: detail on peak I_{Naf} time courses. Bottom panel: I_{NaL} time courses. The WT action potential was included for comparison (black).

Table 12. Steady state action potential durations of isolated wild type and V411M mutated cells in the absence and under exposure to therapeutic concentrations of flecainide or ranolazine. The first column indicates the simulation conditions while the second, third and fourth detail the APD_{90}s of isolated endocardial, midmyocardial and epicardial cells, respectively.

	APD_{90} (ms)		
Model	Endocardial	Midmyocardial	Epicardial
Wild type	268.6	318.9	232.5
V411M^{o}	311.5 (+16.0%)	362.7 (+13.7%)	258.5 (+11.2%)
V411M + Flecainide*	284.5 (-8.7%)	326.9 (-9.8%)	250.4 (-3.1%)
V411M + Ranolazine**	298.0 (-4.3%)	350.3 (-3.4%)	262.3 (+1.5%)

^{o}: Percent change relative to wild type.
*: 1.5 μM. Percent change relative to V411M.
**: 10 μM. Percent change relative to V411M.

The heterozygous V411M mutation showed similar effects on the APD_{90}s of all ventricular cell types. The increase in I_{NaL} amplitude caused a delay in the late repolarization phase, but its magnitude depended on the cell type. In fact, the effects of the mutation were most apparent in endocardial cells with a 16.0% increase, while in midmyocardial and epicardial cells the effects were less intense yet very noticeable, with increases of 13.7% and 11.2%, respectively. Maximum I_{NaL} currents were very similar in all cases, reaching values of 0.75 pA/pF, 0.7 pA/pF and 0.71 pA/pF in endocardial, midmyocardial and epicardial cells, respectively.

Exposure to 1.5 μM flecainide partially countered the APD_{90} elongation produced by the mutation. It reduced the APD_{90} of endocardial cells by a 8.7% by targeting the mutation-induced I_{NaL} peak, a mechanism that was also present both in midmyocardial (9.8% reduction) and epicardial (3.1% reduction) cells. Exposure to 10 μM ranolazine also reduced the APD_{90} prolongation caused by the mutation in endocardial cells (APD_{90} was shortened by a 4.3%), midmyocardial cells (-3.4%) and, but produced a slight prolongation of the APD_{90} in epicardial cells (1.5%). Contrary to flecainide, ranolazine reduced I_{NaL} throughout the entire time course instead of targeting the specific increase

in late repolarization phase I_{NaL} due to the mutation. Peak I_{NaL} of simulated endocardial cells was 0.75 pA/pF in the presence of the heterozygous mutation. It was reduced to 0.32 pA/pF by flecainide but only to 0.52 pA/pF by ranolazine. By contrast, the plateau currents, measured at 100 ms after the pulse, was 0.16 pA/pF without treatment and became 0.080 pA/pF under exposure to flecainide and 0.018 pA/pF under exposure to ranolazine. Interestingly, the APD_{90} reductions caused by both drugs were similar in endocardial cells, suggesting that the total amount of charge that was blocked by either of them was also similar. However, it was not sufficient to compensate the prolongation caused by the mutation in both midmyocardial and epicardial cells.

Finally, both flecainide and ranolazine reduced peak I_{Naf} in endocardial mutated cells from 251.6 pA/pF to 172.6 pA/pF and 204.8 pA/pF, respectively, flecainide showing greater effects, a feature that is consisted with the greater affinity of flecainide for I_{Naf}. This trend was maintained throughout all cell types. In midmyocardial cells, peak I_{Naf} was reduced from 234.3 pA/pF to 146.3 pA/pF under exposure to flecainide and to 188.6 pA/pF under exposure to ranolazine. In epicardial cells, these values decreased from 248.3 pA/pF to 176.1 pA/pF and 207.1 pA/pF, respectively.

Next, we examined the impact of the drugs on the V411M mutation phenotype in endocardial cells at different BCLs (600, 1000, 1500 and 2000 ms) to study the differences that could arise during tachycardia or bradycardia. Figure 40 shows how low and high heart rates affect several biomarkers, namely, APD_{90} (A), qNaL (B), peak I_{NaL} (C) and peak I_{Naf} (D). The V411M mutation (red) increased peak I_{NaL} and qNaL evenly at all BCLs, which resulted in the observed prolongation of the APD_{90}s. Both drugs also slightly reduced peak I_{Naf} as we previously showed for BCL 1000 ms simulations. Flecainide and ranolazine similarly shrunk qNaL to levels close to WT at all BCLs (B). This effect was specially enhanced at shorter BCLs, where qNaLs reached values smaller than WT. Flecainide was more effective at reducing qNaL than ranolazine, a trend that was maintained at all BCLs. Flecainide also reduced the mutation-induced peak I_{NaL} to values close to WT, being more acute at shorter BCLs. Ranolazine was notably less effective in this case. As a side effect, both drugs impaired peak I_{Naf} at all BCLs, but flecainide's impact on this value was considerably greater, which is related to its lower I_{Naf} IC_{50}. Therefore, since ranolazine reduced qNaL to values similar to flecainide, we confirmed that flecainide had a greater and more specific impact on peak I_{NaL}, supporting the fact that both drugs have a different mechanism of action. Our

results also suggest that ranolazine could be beneficial in treating the V411M mutation owing to a significant decrease in total I_{NaL} during repolarization.

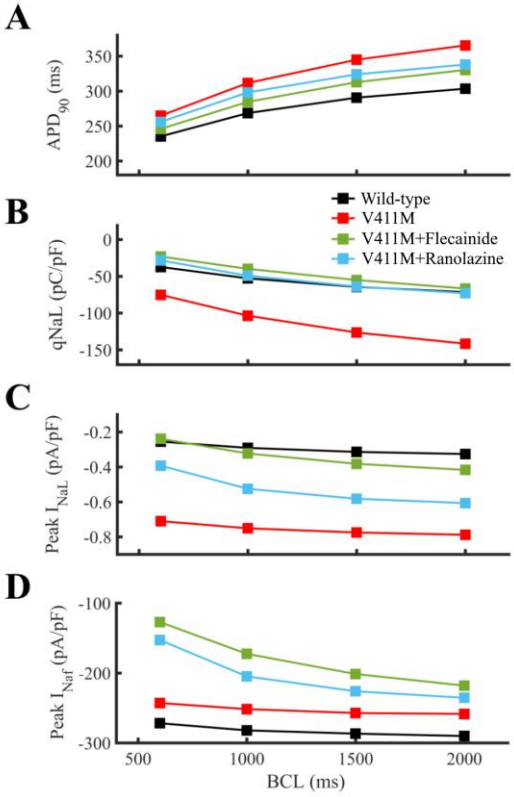

Figure 40. Simulated effects of 10 µM ranolazine (blue) and 1.5 µM flecainide (green) on the restitution dynamics of the APD_{90} (A), qNaL (B) and peak I_{NaL} (C) in isolated endocardial heterozygous SCN5A V411M mutated (red) cells. Drug-free WT (black) results were also included for comparison. qNaL, the total amount of electronic charge carried by I_{NaL}, was calculated as the area under the curve of I_{NaL}.

Steady states from the abovementioned model configurations were used to assess the effects of flecainide and ranolazine on the mutation in a tissue strand. We used them as initial conditions and performed 40-second simulations at 1 Hz pacing rate, saving the last action potential of cells in positions 16, 80 and 150 for further analysis. These were selected as representative cells of their layer bearing in mind that 15 cells from both ends of the strand were not counted for ECG calculation purposes. These positions are the ones that leave

the most distance between other cells therefore reducing the effects of cellular coupling from other layers in the characteristics of their action potential.

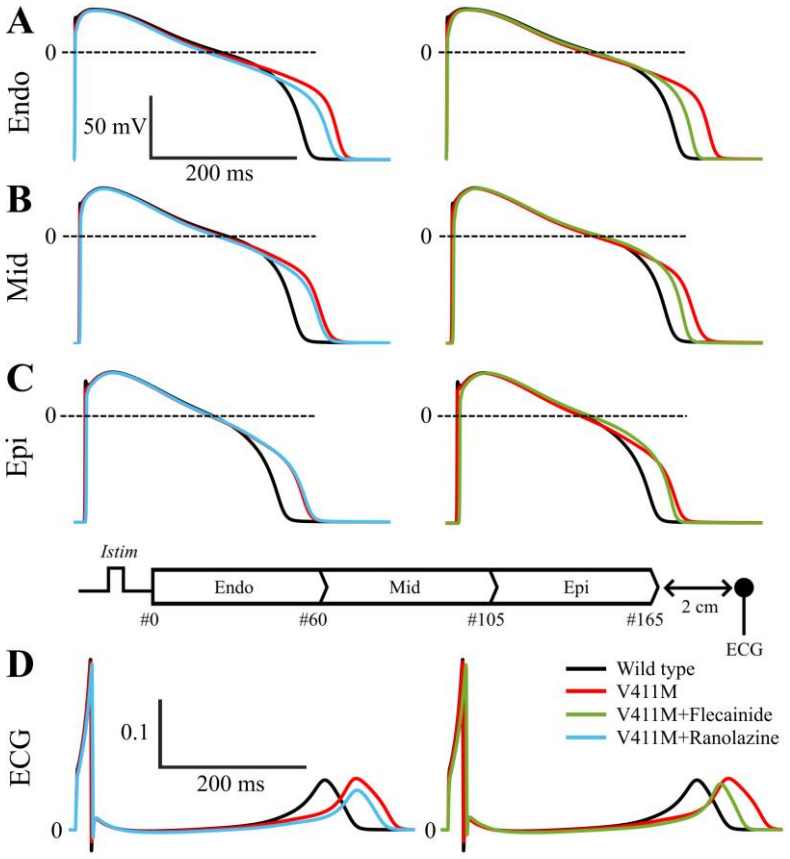

Figure 41. Effects of flecainide and ranolazine in the presence of the heterozygous V411M mutation in endocardial cells the simulated transmural strand. Panels A, B and C: Endocardial, midmyocardial and epicardial action potentials in selected positions of the strand. Panel D: diagram of the model and ECGs corresponding to the action potentials of other panels.

Model	APD_{90} (ms)			
	Endocardial	Mid-myocardial	Epicardial	QT
Wild type	328.8	310.7	279.6	336.8
V411M^{o}	377.1 (+14.7%)	350.7 (+12.9%)	314.5 (+12.5%)	384.8 (+14.3%)
V411M + Flecainide*	350.2 (-7.1%)	330.3 (-5.8%)	303.5 (-3.5%)	357.1 (-7.2%)
V411M + Ranolazine**	363.9 (-3.5%)	343.8 (-2.0%)	315.7 (+0.4%)	372.4 (-3.2%)

^{o}: Percent change relative to wild type.
*: 1.5 µM. Percent change relative to V411M.
**: 10 µM. Percent change relative to V411M.

Figure 41 shows the time course of the action potentials and the ECGs of the last of the 40 beats. The resulting APD_{90}s of representative endocardial, midmyocardial and epicardial cells were 379.6 ms, 310.7ms and 279.6ms, respectively, with a QT segment of 336.8ms. The presence of the heterozygous mutation increased the APD90s to 377.1ms, 350.7ms and 314.5ms, respectively, corresponding to 14.7%, 12.9%, and 12.5% prolongations. It resulted in a QT segment of 384.8ms, equivalent to a 14.3% prolongation, close to the target clinical value.

The exposure to therapeutic 1.5 µM concentrations of flecainide reduced the APD_{90} of all selected cells in the strand. The new endocardial, midmyocardial and epicardial APD_{90}s were 350.2 ms (7.1% decrease), 330.3 ms (5.8% decrease) and 303.5 ms (3.5% decrease), respectively, and the new QT segment value was 357.1 ms, corresponding to a 7.1% decrease compared to the V411M result. Interestingly, the effects of ranolazine on the transmural fiber selected cells were different compared to our previous results in isolated cell conditions, showing very similar to the effects of flecainide. Under exposure to therapeutic 10 µM ranolazine concentrations, the APD_{90}s were 363.9ms (3.5% decrease), 343.8ms (2.0% decrease) and 315.7ms (0.4% increase), with a QT segment value of 372.4ms (3.2% decrease).

Finally, the effects of I_{Naf} block were reflected on the QRS complex duration. Under exposure to both drugs, the duration of this feature increased from 18 ms in wild type to 20 ms with ranolazine, but to 22 ms with flecainide, as a consequence of the higher inhibition of the fast sodium current.

We performed sensitivity analyses of the model's parameters to shed light into the underlying mechanisms of the V411M mutation, ranolazine and flecainide. We represented the results of these analyses in Figure 42 in the form of bar plots. The analysis of the V411M model's parameters (A) suggested that the most important rates towards developing the qNaL and peak I_{NaL} increment (dark grey and light grey, respectively) were the decrease of β13, followed by an increase of α3. The former is modulated by p5, whose decrease produces an impairment in deactivation (transition from the open state to the closed states, as depicted by Figure 43 and Figure 44). The parameters p6 and p7, whose combined modifications induce an enhancement of recovery from inactivation (transition from the inactivated states to the closed states, as depicted by Figure 43 and Figure 44) also exert an influence on qNaL and peak I_{NaL}, although to a lesser extent. These changes are consistent with an increase in sodium channel availability during repolarization, whereby the channels would not only activate faster but also recover from inactivation sooner during the action potential. The fact that the transition rates that determine the proportion of channels in bursting mode (μ1 and μ2) was fixed also supports this hypothesis. Therefore, our simulations suggest that the V411M mutation-induced increase in peak I_{NaL} is due to an increase in the window current.

The sensitivity analysis of flecainide (Figure 42, B, and Figure 43) revealed that the most important transition rates for its attenuation of the mutation-induced increase in APD_{90} are β4n and α4n (neutral flecainide trapping), as well as the ones derived from its affinity for the bursting states. There was also a smaller yet noticeable dependence on β3+ and α3+ (charged flecainide recovery from inactivation). The first rates, β4n and α4n, are modulated by the parameters p13 and p14 and control the trapping mechanics of neutral flecainide. Interestingly, neutral flecainide's trapping into the sodium channel had the greatest impact on APD_{90} prolongation attenuation. The dependence on the drug's affinity for the bursting states (modulated by p16) suggests that flecainide is able to reduce the overall I_{NaL} by blocking the channels that cannot inactivate as well. Finally, flecainide's dependence on parameters modulating recovery from inactivation dynamics (p5 and p6) was small.

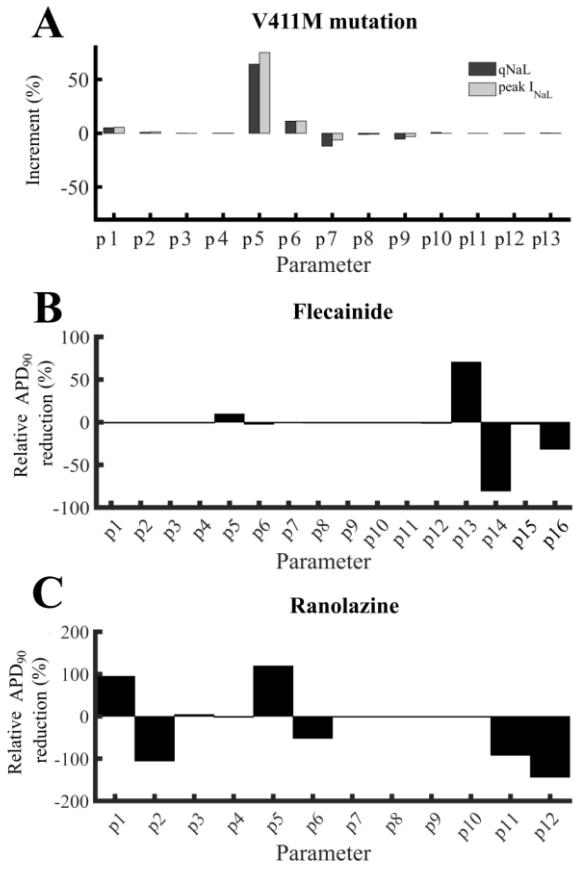

Figure 42. Sensitivity analysis of V411M I_{Na} (A), flecainide (B) and ranolazine (C) model parameters using the isolated endocardial cellular model. A: Peak I_{NaL} and qNaL increments normalized to the values obtained with the optimized model of the V411M mutation when only considering one parameter of the V411M model at a time. Parameters p1 to p13 are defined in Table 9. B: APD_{90} reduction relative to the one produced by the flecainide model in the presence of the V411M mutation when multiplying by 10 one of the optimized flecainide parameters at a time. For example, multiplying p13 by 10 further reduced the APD_{90} of the mutated cell by an additional 70.5% compared to the reduction exerted by flecainide. Parameters p1 to p16 are defined in Table 10. C: Ranolazine sensitivity analysis was performed in a similar way as flecainide's. For example, multiplying p2 by 10 prevented ranolazine from shortening the APD_{90} (around -100% effect). Parameters p1 to p12 are defined in Table 11.

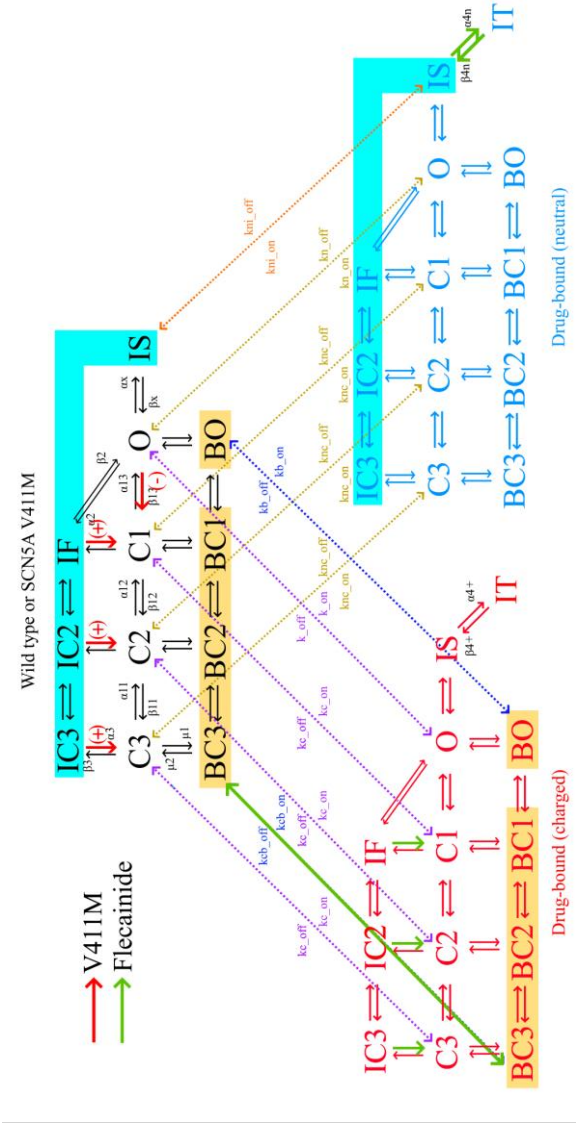

Figure 43. Most important rates defining the effects of flecainide (thick green arrows) on the sodium channel Markov model. The changes that were induced by the V411M mutation were also indicated as thick red arrows. A plus sign indicates an increase of the rate, while a minus sign indicates the opposite. See Figure 2 caption for more details about the diagram of the sodium channel Markovian model.

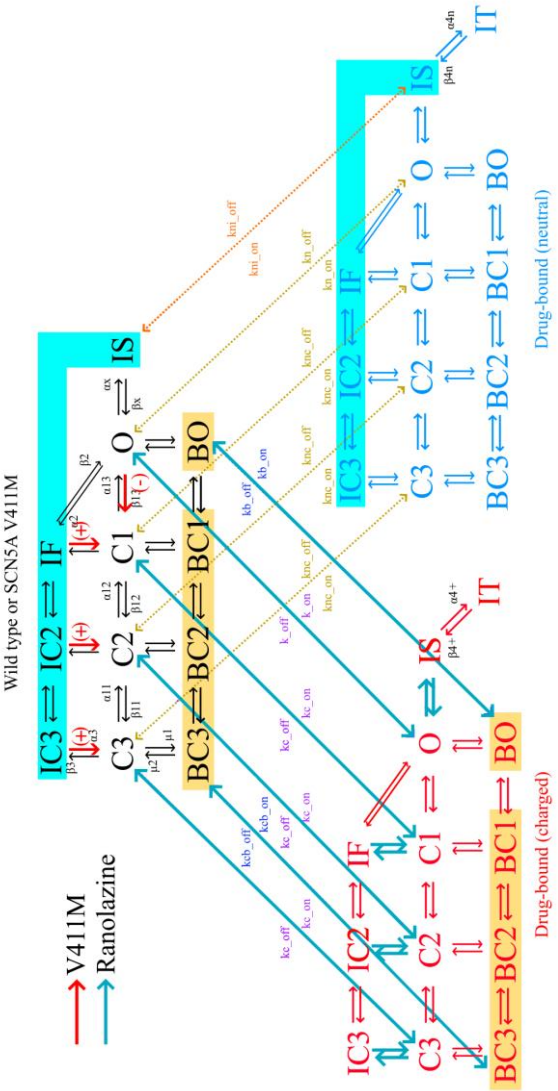

Figure 44. Most important rates defining the effects of ranolazine (thick blue arrows) on the sodium channel Markov model. The changes that were induced by the V411M mutation were also indicated as thick red arrows. A plus sign indicates an increase of the rate, while a minus sign indicates the opposite. See Figure 2 caption for more details about the diagram of the sodium channel Markovian model.

Ranolazine's attenuation of APD_{90} prolongation was determined by a combination of several mechanisms (Figure 42, B, and Figure 44), and highly depended on transition rates β3+ and α3+ (recovery from inactivation of the channels bound to charged ranolazine, parameters p5 and p6) as well as βx+ and αx+ (recovery from slow inactivation of the channels bound to charged ranolazine, parameters p1 and p2). While we did not optimize charged ranolazine's affinities for the normal and bursting modes (controlled by parameters p11 and p12), the sensitivity analysis showed that these were very important to the drug's effect on the APD_{90}. Contrarily to flecainide, ranolazine depended in a similar way to all the beforementioned transition rates. There was a high reliance on the affinity to bursting states, which is consistent with previous results on the ΔKPQ mutation. Importantly, since ranolazine did not show trapping dynamics, the drug-induced APD_{90} prolongation attenuation was determined by a decrease in recovery from fast and slow inactivation, which is contrary to the modifications introduced by the mutation. These results confirm that both drugs act through different mechanisms of action on the mutation-induced APD_{90} prolongation and suggest that ranolazine could in fact be beneficial to patients carrying the V411M mutation.

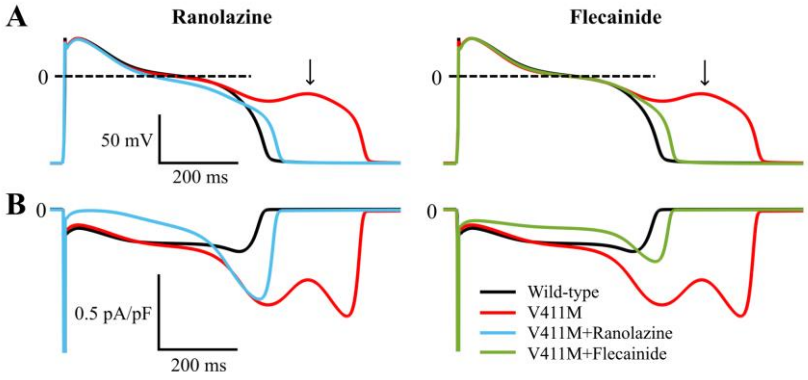

Figure 45. Simulated effects of 10 µM ranolazine (blue) and 1.5 µM flecainide (green) on EAD generation in slow paced (BCL = 3000 ms) isolated midmyocardial heterozygous SCN5A V411M mutated (red) cells. Drug-free wild type (black) is also included for comparison.

To determine whether ranolazine could be used as an alternate treatment to flecainide, we studied the effects of therapeutic concentrations of the drug in bradycardic conditions, which are known to favor arrhythmia triggers such as EADs, especially in LQTS type 3. For that matter, we paced a mutated midmyocardial cell at a BCL of 3000 ms to steady state. Figure 45 depicts the

action potential time course (A) and I_{NaL} time course (B) of the mutated cell (red), which developed EADs (black arrows). The WT action potential and I_{NaL} time courses (black lines) were added for comparison. The exposure of the mutated cell to 10 µM ranolazine (blue) normalized the action potential morphology, prevented EAD development and reduced the APD_{90} of the cell to values closer to WT. Exposure to 1.5 µM produced a similar effect and prevented EAD development. However, ranolazine reduced the plateau potential more than flecainide due to its effect on whole I_{NaL}, while flecainide's impact was focused on the mutation-induced I_{NaL} peak. This finding is consistent with previous simulations in endocardial cells. These results suggest that EAD generation could be avoided by both drugs due to a similar reduction in qNaL, and that ranolazine could be used as an alternate treatment to flecainide in patients carrying the SCN5A V411M mutation.

4.4 Discussion

4.4.1 Main outcomes

In this chapter, we explored a specific approach to personalized medicine consisting of developing custom ionic models for the cardiac sodium current. These included a wild type model, a mutation model and two drug models to test the effects of two treatments for the mutation. To achieve our goals, we created custom software that we used to update and optimize the wild type model with new data about I_{NaL}. Next, we created a new model for the SCN5A V411M mutation reproducing the tests from Horne and coworkers[173] as well as clinically observed prolongations of the QTc. The model of the mutation produced an increase in I_{NaL} peak due to reactivation caused by an increased window current, consistent with the authors' findings. We then updated and optimized a flecainide model with more recent I_{NaL} data and optimized a ranolazine model. Finally, we tested the effects of treatments with the drugs on the V411M model and found that both are capable to reduce the mutation-induced prolongation with similar results over a wide range of pacing rates, albeit via a different subjacent mechanism. In fact, flecainide targeted the increase in I_{NaL} peak during the repolarization phase while ranolazine reduced I_{NaL} during the entire time course. Nonetheless, both drugs could prevent arrhythmia triggers such as EADs in bradycardic conditions possibly owing to their similar reduction in qNaL.

4.4.2 Ranolazine, flecainide and LQT3

Ranolazine has shown effectiveness reversing the effects of several LQTS type 3 inducing mutations caused by an increase in I_{NaL}[194,224,225]. Moreno and

coworkers[90] hypothesized that ranolazine could be effective as a treatment of the SCN5A ΔKPQ mutation phenotype, a complex condition that includes LQTS type 3 but also conduction disease and Brugada syndrome[226]. Their results showed that ranolazine could prevent EAD generation by considerably reducing I_{NaL} in both isolated cardiomyocytes and tissue models. They reported more than a 50% reduction of the APD_{90} of mutated cells with therapeutic concentrations of ranolazine. By contrast, our results show a 4.3% reduction of the APD_{90} in the endocardial myocyte model with the heterozygous SCN5A V411M mutated channel. However, the ΔKPQ mutation is characterized by a five-fold increase in the proportion of channels in bursting mode, which greatly increases the overall I_{NaL}. On the one hand, ranolazine showed high affinity for the bursting states of the channel, which makes it even more effective in treating conditions that alter their proportion such as ΔKPQ. On the other hand, the APD_{90}s were measured during EAD episodes, which greatly increase their value. The abovementioned phenomena could explain the discrepancies between our work and Moreno and coworkers'. Therefore, ranolazine could be beneficial in V411M patients but its effects may not be as pronounced as in the ΔKPQ mutation.

In this work we updated the I_{NaL} blocking power of Flecainide due to discrepancies between the Moreno and coworkers' model[89] results and new experimental data (see below). This drug has a long history of nearly 30 years in the market[199]. Since the implantation of the ICH guidelines[14,15], it underwent trials to assess its proarrhythmicity. In fact, FDA drug labels[130] include a special mention to QT prolongations, and it appears to produce a small prolongation of the QTc values of an 8% in healthy patients. However, 60% to 90% of that prolongation is caused by an increase in the QRS complex duration (QRS widening), consistent with its I_{Naf} blocking properties[199] and contrarily to other QTc prolonging drugs such as dofetilide which does so by blocking I_{Kr} and delaying repolarization,. Flecainide's free therapeutic plasma concentrations are in the 0.4 to 2.5 μM[227], similar to the I_{Naf} and I_{Kr} IC_{50} range[199]. Reductions of I_{Kr} amplitude are associated with important prolongation of the APD_{90} and QT intervals as we previously explored in 2.4. Block of potassium channels by flecainide has been studied in the literature. Belardinelli and coworkers[182] studied the effects of flecainide in rabbit preparations at physiological temperature (36ºC) and obtained an IC_{50} of 1.5 μM. Ducroq and coworkers[228] performed a similar study but their model was HEK293 cells transfected with human hERG channels, yielding an I_{Kr} IC_{50} of 0.74 μM at room temperature (22ºC). Melgari and coworkers[227] obtained an IC_{50} of around 1.5 μM (CI: 1.27–1.74 μM) also in HEK cells at physiological temperature, the same conditions as Paul and coworkers[221] used in their work,

who obtained a value of 3.94 μM. I_{Kr} conductance reductions are therefore to be expected at therapeutic concentrations. However, flecainide does not delay repolarization in rabbit even shortening the APD in Purkinje fibers[146,228–231]. Additionally, Caballero and coworkers[220] found that flecainide enhanced I_{K1} which reduces the APD. Block of I_{NaL} does also produce a similar APD shortening effect and, combined with an I_{K1} increase, could represent a mechanism that compensates the effects of I_{Kr} block experimentally, but there is a considerable variability in the I_{NaL} IC_{50}s, ranging from 44 μM[181], to 19 μM[124] to 3.4 μM[182]. Recent works using a new protocol designed to mimic the action potential repolarization (phase 3 of the AP) found increasingly lower I_{NaL} IC_{50} values such as 1.9 μM[232]. Matsukawa and coworkers used the newest protocols for I_{Naf} and I_{NaL} IC_{50} assessment recommended by the CiPA project and found that the latter was 1.7 μM[222].

In combination with β-blocker treatment, flecainide was very effective in treating the heterozygous V411M mutation phenotype. In two case-reports, the drug was able to completely compensate the QT segment prolongation[174,175] while in one it was not administered [173]. Our simulations show that flecainide slightly prolonged the APD_{90} of the endocardial cell in wild type conditions (1.2%) and incompletely counteracted the APD_{90} prolongation produced by the presence of the heterozygous mutation. Flecainide effects seem to be slightly more positive in the clinical practice. As our I_{NaL} IC_{50} resembles experimental observations, this could be explained by *in vitro-in vivo* differences due to the mutant channel being transfected to HEK cells, lacking the interactions with native currents and signaling pathways. To account for this, we introduced the required prolongation of the APD_{90} in the mutation optimizations as a surrogate of the QT prolongation, which we simulated in the tissue strand model. Another possible reason could be that we had overestimated the I_{Kr} blocking effect of flecainide due to *in vitro-in vivo* differences in terms either of drug exposure or the values of the ionic current conductances in the action potential model, whose experimental measurement is subject to a high variability. Indeed, a smaller contribution of I_{Kr} to the action potential time course would result in a smaller impact on the repolarization reserve of the cell and a subsequent shorter APD_{90} prolongation, thus helping close the gap between clinical observations and the simulations with flecainide in the presence of the mutation.

To test this hypothesis, we simulated the effects of flecainide and ranolazine on the isolated mutated endocardial cell taking only into account the impact on I_{Na}. We suppressed the concentration-dependent modifications of I_{Kr} and I_{K1} conductances and paced the cells to steady-state.

Figure 46 shows that both drugs would counter the APD_{90} prolongation induced by the V411M mutation in endocardial and midmyocardial cells, while bringing the APD_{90} to values very close to WT in epicardial cells. Therefore, I_{Kr} block could be responsible for the small prolongations that can be observed during treatment with both flecainide and ranolazine.

Finally, we optimized our models to reproduce experimental APD_{90} restitution curves with success (see Figure 36) by applying the reported intercellular differences in channel conductances. As a natural consequence, isolated midmyocardial cells show the longest APD_{90}, followed by endocardial and epicardial cells. The same cells show different APD_{90}s in the transmural wedge model, where the endocardial cells show the longest APD_{90} followed by midmyocardial and epicardial cells. The intercellular electrical coupling of the cardiac tissue reduces the dispersion of repolarization[233] giving this characteristic APD_{90} distribution in models like the one we used in this chapter[89,90].

4.4.3 Personalized medicine

In this chapter, we took a more specific approach to drug effect prediction. Here, we explained the steps involved in developing models and testing them. For that matter, we used already existing models and improved them by including new data. In the I_{Na} wild type model, we included tests to specifically optimize I_{NaL} dynamics considering how crucial the current is to the APD restitution for the three cardiac cells. As for flecainide, we also included new I_{NaL} tests to ensure the drug was correctly reproducing its block dynamics. By contrast, ranolazine's model already took into account all the necessary dynamics that were consistent with the literature and therefore we optimized the model to the new wild type formulation. Finally, we created a new model for the V411M mutation using specific patch-clamp data obtained in transfected cells with the mutant channel. We explored specific channel-drug interactions that determine the effects of flecainide and ranolazine, two antiarrhythmic drugs that show affinity for the I_{NaL}[51,177]. Ranolazine and flecainide show a similar block potency for I_{NaL}, showing IC_{50}s of 6 μM[223] and 1.7 μM[222], respectively, compared to their therapeutic concentrations of around 10 μM[90] and 1.5 μM[234]. However, our results show that their mechanism of action is different, revealing that flecainide is more specific towards the V411M mutation induced late repolarization I_{NaL} peak, which represents an advantage compared to ranolazine. This could explain its success treating the condition[173–175]. All in all, our results represent an effort towards the development of personalized medicine for patients carrying the V411M mutation.

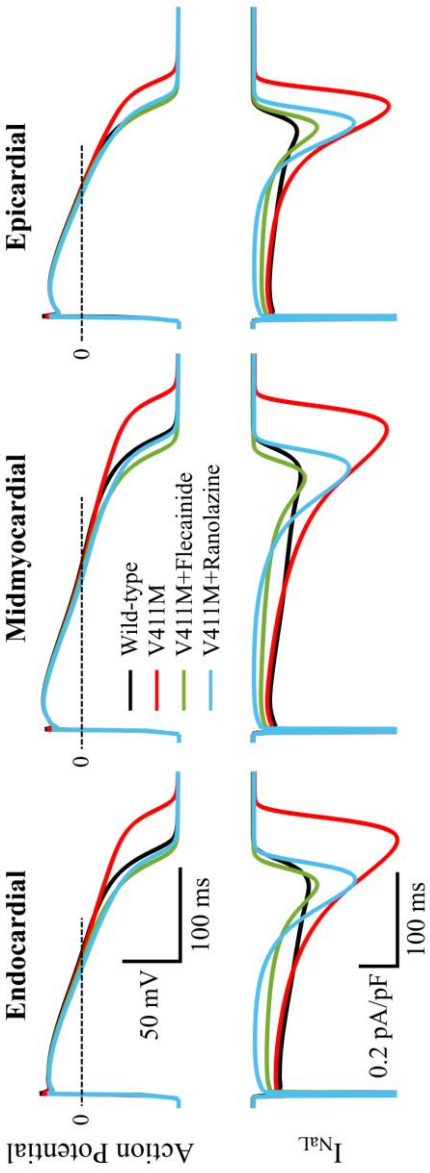

Figure 46. Simulated action potential (top row) and I_{NaL} (bottom row) steady-state time courses of the isolated endocardial (left column), midmyocardial (middle column) and epicardial (right column) cells under exposure to therapeutic concentrations of flecainide (green) and ranolazine (blue) without accounting for the effects on I_{Kr} and I_{K1}. The APD_{90}s of the action potential time courses under flecainide and ranolazine treatments in those conditions were, respectively, 257.5 ms and 263.3 ms for the endocardial cells, 303.7 ms and 315.5 ms for the midmyocardial cells, and 232 ms and 237.3 ms for the epicardial cells. The heterozygous V411M mutant (red) and wild type (black) time courses were also added for comparison.

4.4.4 Implementation

There were numerous requirements to take into account in the optimizations that we performed in this chapter. They include general knowledge about optimization protocols, which is useful to prevent the most common issues, such as avoiding local minima, preference to one test due to uneven error distribution, in addition to their complexity due to the number of parameters that have to be fit at once[77,235]. Knowledge about Markov models is also needed in order to avoid overparametrization of the model, which could confuse the optimization function, or underparametrization, which prevents the model from reaching an optimal fit to the references. Additionally, knowledge concerning manual and automatic patch-clamps is convenient to reproduce experimental protocols in in-silico models. Understanding of drugs and ion channels is also helpful towards understanding the microscopic interactions that happens during administration of a drug, which can be completed with pharmacokinetic and pharmacodynamics knowledge. Last but not least, good programming skills are also helpful towards developing fast and efficient code. Therefore, familiarization with numerous fields of knowledge is a requirement to implement these optimizations.

As for the initial implementation costs, apart from the time that a non-initiated has to spend to integrate the required knowledge, we would like to highlight the great amount of manual work that requires the individual reproduction of each patch-clamp protocol. From our experience during the elaboration of this work, this is a relatively high time-consuming task that requires the implementer to search through every experimental work for the necessary parameters, which will be then manually inserted into the code (there are of course several programming strategies to reduce the manual work to a minimum, which we have implemented). The amount of data that is required is also considerable, since to obtain good results the modeler must constrain the model with sufficient tests so that all the dynamics are covered. Additionally, voltage protocols have to be designed around each channel-drug combination to correctly assess their particularities. Therefore, implementation of this kind of personalized approaches is initially time and resource consuming.

Concerning the reusability of the code, every model is designed to reproduce the dynamics of a particular channel-drug interaction. Multi-channel block has proven useful explaining why some drugs are safe despite blocking I_{Kr} with high affinity[58,236]. Assessment of the effects of multi-channel blocker drugs would require model implementations for every channel that is relevant to the effects of the drug. Regarding Markov models, they could potentially be used

as a starting point for another mutation and another drug. Therefore, while reusability of these models is more limited, the framework that needs to be created for the optimization of one model can lay the groundwork for future optimizations.

All the above considered, we conclude personalized approaches such as the one we implemented in this chapter are useful in shedding light into particular phenomenon such as the dynamics of a dysfunctional ion channel or the differences between similar drugs that exert different effects.

As standardized high throughput patch-clamp devices such as Qpatch[66], PatchXpress[108], IonWorks/FLIPR[69] improve their functionality, the initial cost of the channel-drug interaction electrophysiological assessment could diminish considerably. Likewise, as new technologies make their way to the consumer, such as the access to graphics processing units (GPUs), computationally efficient code can be written to improve the calculation speed of Markov models, which has already been done in neuronal models[237,238].

4.4.5 Limitations

In this work, there are limitations that must be acknowledged. Markov models are known to be versatile and reproduce a wide variety of ion channel dynamics from several sources[41]. However, this fact does not forcedly mean that the subjacent mechanism is the actual explanation for the physical phenomenon it describes. There are nonetheless countless examples of models that were able to predict physical phenomena before they were able to be measured. Our model offers a possible mechanism to why flecainide has shown good results in V411M patients, as well as evidence supporting the potential benefits of using ranolazine. Future experimental and clinical confirmation of our findings would be beneficial.

Concerning the technical side of this work, we prioritized the computational cost reduction in detriment of wider reaching protocols for optimization. In fact, to compensate for using high computationally demanding Markov models, we used the implementation of the Nelder-Mead simplex implementation from Moreno and coworkers as in other studies[77,89–91] because of its ease to implement, speed, parallelization capability, and overall reduced computational requirements. This algorithm has shown a high likelihood of falling into local minima instead of global minima and a need for high number of iterations[77]. However, our optimizations were not intended to dramatically modify the dynamics of the whole sodium channel formulation. We aimed to improve the model by expanding some of its dynamics instead. To do so, we tried to overcome the local minimum by randomizing the initial parameter sets

with a 10% variability. Therefore, we could reduce the number of maximal iterations to 300 where the parameter increments were already low, reducing the computational cost.

Some optimizations were expanded with additional simulations using the endocardial cell action potential model, which we paced for 40 seconds at 1Hz. While it could be acknowledged that the model has not reached steady-state, we used this value to reduce computational cost and to provide a close enough approximation to the steady-state results. We confirmed this by comparing longer 300-beat simulations to the ones we performed during the optimizations in Figure 47. The former (continuous lines) were very close to the latter (dashed lines), being almost identical for the WT (black) and V411M models (red), and showing little differences in V411M under exposure to flecainide (green) and ranolazine (blue). Furthermore, we simulated the models to steady-state after the optimizations to elaborate the results we used to draw our conclusions.

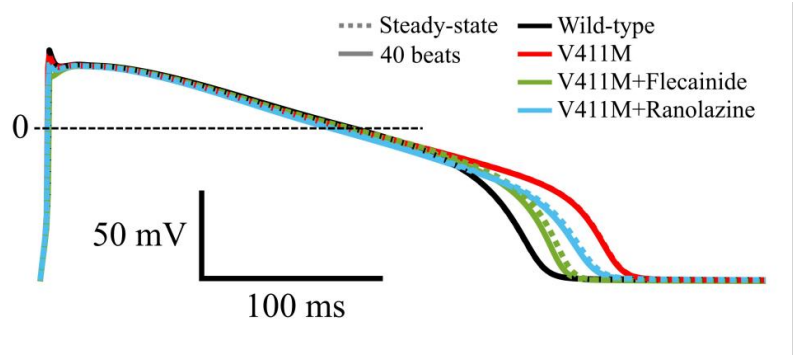

Figure 47. Comparison of the simulated action potential time courses for isolated endocardial cells after a train of 40 pulses (continuous lines) and at the steady-state (300 pulses, dashed lines). Wild type (black lines) and V411M mutated (red lines) cells in control and under exposure to therapeutic concentrations of flecainide (green lines) and ranolazine (blue lines). The very small differences between the simulated action potential time courses obtained with 40 and 300 pulses corroborate the validity of applying 40 stimuli to the isolated endocardial models in order to reduce the computational cost during the optimization procedure of the wild type, flecainide and mutation I_{Na} models.

In our work we used QTc values from patients undergoing β-blocker treatment, which are consistent with our simulations due to the lack of β-stimulation in our models. By contrast, reference control QTc values were taken from the general population.

Horne and coworkers[173] assessed the effects of the V411M mutation on the late repolarization phase with a ramp protocol similar the most recently recommended protocol for assessing drug block of I_{NaL}[222,239]. Our first attempts at reproducing this protocol were successful but the resulting increase in I_{NaL} was insufficient to reproduce the clinical APD_{90} and QT prolongations while hampering the fit of other protocols. A possible solution would consist of fitting the wild type model to the wild type curves that were provided by Horne and coworkers. Nonetheless, this would have needed a more dramatic modification of the model since some of them showed important differences with the original fit reference data[89]. Another reason for this discrepancy could arise from the fact that the channel was isolated and thus were lacking interaction with other currents and proteins, specifically from their β-subunit, which are known to modulate the response of channels[240].

Horvath and coworkers recently published a new work expanding their findings on I_{NaL} dynamics using the self-AP clamp technique[186]. They found that canine and human I_{NaL} had similar time courses, a characteristic decreasing amplitude over the duration of the action potential, as opposed to guinea pig, which showed an increasing current that was maximal during the late repolarization phase and ended quickly afterwards. Although in this chapter we fitted our current to the guinea pig time course, we aimed at reducing the late repolarization peak and increasing the contribution of the current during the whole action potential, similar to the state-of-the-art cardiomyocyte model[107]. Therefore, the current wild type model represents an improvement over the model before optimization.

Recent work on the effects of mexiletine, a sodium channel blocker like flecainide and ranolazine, has shown that the block impact of the drug on the action potential could depend on the mutation[241]. In fact, important modifications of the peptide chain that forms the channel can alter its affinity for some drugs due to alterations on the binding site[242]. In this chapter, the WT and V411M models use the same affinities for the drugs. To improve this aspect of the models, new experimental data would be needed.

Finally, it should be noted that the various I_{Na} models that we generated are dependent on both the action potential model and the particular dataset that we used to optimize them. We used the Grandi-Bers with Soltis-Saucerman model of the action potential, which had already been used to test the effects of ranolazine on the ΔKPQ mutation[90]. Our WT model was optimized to reproduce the human APD_{90} restitution curve. Other models might show different APD_{90} values due to differences in current conductances, and therefore the I_{Na} model would require to be optimized to reproduce the

experimental data again. Likewise, the parameters of our models are dependent on the dataset we used to optimize them. Using other datasets might result in quantitatively different outcomes, although they should remain qualitatively similar.

All in all, we think that the main conclusions that can be drawn from our results are not invalidated by these shortcomings.

4.5 Conclusions

In this chapter, we delved into a personalized medicine approach by assessing the effects of two drugs on a LQTS type 3 causing mutation. To do so, we improved a wild type sodium current model with better I_{NaL} dynamics and used it to create a custom model for the V411M mutation. Then, we improved a flecainide model and optimized a ranolazine model and tested their effects on the mutation in three isolated cardiomyocyte action potential models and a transmural strand ECG model. Both drugs were similarly effective at countering the mutation induced prolongation of the APD_{90} and QT segment prolongations, but their mechanism was different. While ranolazine reduced I_{NaL} over the complete time course of the current, flecainide was more specific of the late phase 3 repolarization peak that had been induced by the mutation. Additionally, both drugs were able to substantially reduce the APD_{90} of mutated cells paced at slow rates, preventing arrhythmia triggers such as EADs. This suggests that, while the mechanism of action for flecainide's and ranolazine's effectiveness was different, the former could be an alternative in these patients, especially when suffering from cardiac structural disease, where conduction slowness could represent a risk of arrhythmia.

In this chapter, we provided great detail and understanding of the mechanisms that determine the effects of the V411M mutation, as well as the effectiveness of two antiarrhythmic drugs that, despite targeting the same channel, have different mechanisms. We dove into a highly time-consuming approach to create personalized models for specific channelopathies in order to shed light on their subjacent mechanism. This approach could help to select a better treatment based on specific channel-drug owing to the reusability of the optimization tools that we used.

Chapter 5. General Conclusions

The main objective of this PhD thesis consisted of using electrophysiological models of the human ion channels and action potential to predict the effects of drugs on cardiac electrophysiology. We identified two scenarios with important challenges that would benefit from using such models and simulations. Therefore, we divided this PhD thesis in two chapters enclosing distinct modeling approaches, namely, the study of drug safety and efficacy. For the former, we sought to generate an easy-to-use tool for prediction of the arrhythmogenic potential in drug development. For the latter, we sought to provide an alternate treatment with ranolazine to patients carrying the SCN5A V411M mutation. Our results show the usefulness of modeling and simulation to tackle the challenges that arise from different areas by providing adapted solutions. Our main findings are summarized below.

Development of an easy-to-use tool based on cardiac electrophysiological models to detect potentially arrhythmogenic drugs in the early stages of drug development.

The first modeling approach sought to generate a biomarker (Tx) to improve the arrhythmogenicity prediction for newly developed drugs by creating a model based on a large number of compounds with known risk.

We pre-computed four matrices covering a wide range of ion channel block profiles. These matrices successfully removed the need for further simulations with the action potential and pseudo-QT models, effectively reducing the complexity of use.

This modeling approach made use of an extensive list of 84 drugs with known risk and translated their effects on human action potential models by applying reductions to three major currents that affect repolarization (I_{Kr}, I_{Ks}, I_{CaL}). Therefore, the tool was created upon a large number of drugs.

This approach was successful in detecting proarrhythmic drugs with a 90% AUC and an 87% accuracy and could be used to classify new compounds or to search for safe concentration ranges. The results of the isolated endocardial cellular and the transmural cardiac strand models provide the best performance while also showing very similar results.

Providing evidence for an alternative treatment to flecainide for long QT syndrome SCN5A V411M patients when its use is not indicated.

The second modeling approach was applied to a specific LQTS type 3 inducing mutation (V411M) of the SCN5A gene that had yet to be modeled. It sought provide evidence that supports the potential benefits of an alternate treatment

with ranolazine. This modeling approach was characterized by being focused on the dynamics of the drug-channel interactions using Markov models, which contrasts with our first IC_{50} based approach.

We conclude that this mutation increases I_{NaL} by reducing deactivation and consequently increasing the window current. The model was built and optimized by reproducing clinical and experimental data. Therefore, we successfully created a Markov model of the V411M mutation.

We optimized the models of flecainide and ranolazine by closely reproducing clinical and experimental data, which we expanded in flecainide's case to keep up with new discoveries. Therefore, we successfully simulated the effects of both flecainide and ranolazine on cardiac electrophysiology.

The effects of flecainide were focused on the specific I_{NaL} peak produced by the V411M mutation. Ranolazine reduced the whole I_{NaL} time course. Both drugs brought the qNaL values close to wild-type, which supports the therapeutic potential of ranolazine. Therefore, we successfully provided an explanation for the beneficial effects of flecainide and showed that ranolazine could be used as an alternate treatment.

All in all, this PhD thesis contributes to the improvement of current pharmacological treatments by using multiscale mathematical models of the electrical activity of the heart to assess the cardiotoxicity of drugs and the efficacy of antiarrhythmic drugs. This work exemplifies that modelling and simulation of drug action in virtual patients is a promising, efficient, cost-effective, and ground-breaking methodology that can reveal fundamental biological principles and mechanisms which can improve the design and development of drugs.

Chapter 6. Future work

The main objective of this PhD thesis is to predict the effects of drugs on cardiac electrophysiology using computational modeling and simulation. We were successful in creating a biomarker for drug risk assessment and optimizing four Markov models of the sodium current. The framework that we created to do so is not stiff and several modules can be swapped for more recent models.

For example, the model used to simulate the action potential time courses and measure APD_{90}s could be changed to create new matrices. Likewise, the channels that we considered could be expanded to cover the late sodium current block, which could potentially improve the performance of the Tx biomarker due to its importance in repolarization.

As for the Markov models, we used an approach that could be used to optimize multiple mutations. Using the appropriate error functions would lead to parameter combinations describing the dynamics of other LQTS types, including both gain-if-function and loss-of-function mutations. Likewise, this could be applied to optimizations of drugs interacting with the sodium channel, but also with other channels by setting another Markov model corresponding, for example, to the hERG channel.

All in all, future work could include:

- To make use of the latest human action potential model, which is currently being used by CiPA, to test the performance of the Tx biomarker.
- To expand the Tx biomarker by taking into account I_{NaL} and other parameters other than the APD_{90} and pseudo-QT.
- To model mexiletine and test it on the V411M mutation.
- To generate models of other mutations of the human sodium channel and simulate the effects of sodium blockers to make a contribution to the patients' treatments.

Chapter 7. Contributions

This thesis was developed in close collaboration with other institutions from a multidisciplinary point of view, which is common in every research field. As a consequence, we have spread the results of this work in high level conferences and scientific reviews of national and international scope.

7.1 Journal Papers

7.1.1 Main contributions

- Romero, L., **Cano, J**., Gomis-Tena, J., Trenor, B., Sanz, F., Pastor, M., et al. (2018). In Silico QT and APD prolongation assay for early screening of drug-induced proarrhythmic risk. *J. Chem. Inf. Model.* 58, 867–878. doi:10.1021/acs.jcim.7b00440 **(Co-first_author)**
- **Cano J.**, Zorio E., Mazzanti A., Arnau M.A., Trenor B., Priori S G., Saiz J. Romero L. Ranolazine as an alternative therapy to flecainide for SCN5A V411M Long QT Syndrome type 3 patients. *Front. Pharmacol. (accepted)* doi:10.3389/fphar.2020.580481

7.1.2 Related contributions

- Gomis-Tena, J., Brown, B. M., **Cano, J**., Trenor, B., Yang, P. C., Saiz, J., et al. (2020). When Does the IC50 Accurately Assess the Blocking Potency of a Drug? *J. Chem. Inf. Model.* doi:10.1021/acs.jcim.9b01085.
- Llopis, J., **Cano, J**., Gomis-Tena, J., Romero, L., Sanz, F., Pastor, M., et al. (2019). In silico assay for preclinical assessment of drug proarrhythmicity. *J. Pharmacol. Toxicol. Methods 99*, 106595. doi:10.1016/j.vascn.2019.05.106.

7.2 Conference papers and communications

7.2.1 Main contributions

- **Cano J**., Saiz, J., Romero L., Gomis-Tena J., Amberg A., Anger L., Ballet V., Guillon J.M., Pastor M. Sanz F., Development of an In-silico Action Potential Model of the Rabbit Purkinje Cell for Assessment of Cardiac Safety Liabilities. Annual SPS meeting. September 2017. Berlin, Germany.
- Romero L., **Cano J**., Gomis-Tena J., Trenor B., Sanz F., Pastor M., Saiz J. In-silico QT Assay for Preclinical Assessment of Drug-Induced Proarrhythmicity. Annual SPS meeting. September 2017. Berlin, Germany.
- **Cano J**., Romero L., Gomis-Tena J., Sanz F., Pastor M., Saiz J., Mejora en la predicción del riesgo de cardiotoxicidad inducida por

fármacos mediante un nuevo biomarcador. CASEIB. November 2016. Valencia, Spain.

- **Cano J**., Arnau M.A., Zorio E., Saiz J., Romero L., Modeling the Effect of Two Sodium Channel Blockers on the LQTS3 Heterozygous V411M Mutation of the SCN5A Sodium Channel. Annual Japanese SPS meeting. March 2020. Tokyo, Japan.
- **Cano J**., Romero L., Gomis-Tena J., Trenor B., Sanz F., Pastor., M., Saiz J., Tx, a New Biomarker for In-Silico Early Assessment of Drug-Induced Proarrhythmic Risk. Virtual Physiological Human meeting. September 2018. Zaragoza, Spain.
- **Cano J**., Arnau M., Zorio E., Saiz J., Romero L., Simulation of the Effects of Flecainide and Ranolazine Under LQTS Type 3 Produced by the Heterozygous SCN5A V411M Mutant. Annual SPS meeting. September 2019. Barcelona, Spain.

7.2.2 Related contributions

- Maturana A., Clancy C., Cano J., Romero L., Modelado y simulación del efecto del moxifloxacino en la componente rápida de la corriente diferida rectificadora de potasio. CASEIB. November 2016. Valencia, Spain.
- Romero L., Cano J., Gomis-Tena J., Trenor B., Sanz F., Pastor M., Saiz J., In silico QT and APD prolongation assay for early screening of druginduced proarrhythmic risk. Gordon Research Conference. February 2017. Ventura, USA.
- Llopis J., Cano J., Gomis-Tena J., Romero L., Sanz F., Pastor M., Trenor B., Saiz J., In-Silico Classifier for Early Screening of Drug-Induced Torsadogenic Risk. Annual SPS meeting. September 2019. Barcelona, Spain.
- Llopis J., Cano J., Gomis-Tena J., Romero L., Trenor B., Saiz J., Estudio in-silico de la cardiotoxicidad inducida por fármacos en células ventriculares sanas y con insuficiencia cardíaca. CASEIB. November 2018. Ciudad Real, Spain.

7.3 Research projects

This PhD thesis was developed within the following projects:

- Ministerio de Economía y Competitividad and Fondo Europeo de Desarrollo Regional (FEDER) DPI2015-69125-R (MINECO/FEDER, UE): “Simulación computacional para la predicción personalizada de los efectos de los fármacos sobre la actividad cardiaca”.
- Dirección General de Política Científica de la Generalitat Valenciana (PROMETEU2016/088): “Modelos computacionales personalizados

- multiescala para la optimización del diagnóstico y tratamiento de arritmias cardiacas (personalised digital heart)".
- Vicerrectorado de Investigación, Innovación y Transferencia de la Universitat Politècnica de València with Ayuda a Primeros Proyectos de Investigación (PAID-06-18), and by Memorial Nacho Barberá.
- Instituto de Salud Carlos III (La Fe Biobank PT17/0015/0043).

7.4 Cardiac Safety prediction tool

Chapter 3 of this PhD contributed to the development under a license agreement (2019) of a tool capable of assessing the TdP risk of drugs during their development stages called "QT/TdP Risk Screen".

The online tool can be accessed through the INSILICOTRIALS website (direct link to the QT/TdP tool):

- https://qttdp.insilicocardio.com/

Appendix. Optimization procedure

This section contains detailed information about the protocols that we used to optimize WT, flecainide and ranolazine models as well as to create the SCN5A V411M mutation model.

A. 1. General considerations

Optimizations were performed with Moreno and coworkers' implementation of the Nelder-Mead simplex, a function called "fminsrchbnd". The implementation of this algorithm was provided by the authors. Its inputs include a set of scalar parameters to be optimized, their corresponding upper and lower boundaries and a custom cost function, which returns the result of a series of tests that evaluate the goodness of the fit of our model to the reference as a scalar value.

Cost functions were iteratively evaluated while modifying the parameters until termination conditions were met, namely, the maximum number of iterations (300) or the error score increment being less than 0.01. The latter was rarely the case because of computational limitations.

Parameters to be optimized were introduced in specific locations in the Markov sodium current formulation as in Moreno and coworkers[89,90] (see Table A.1) which enabled automatic modification of the current dynamics. During the optimizations, parameters were restricted to positive values.

Cost functions evaluated several current dynamics whose score was calculated as the sum of squared differences between simulations and references. Some tests gave results in very different units, which we solved by including custom scalar factors multiplying their error scores to bring them in-line with other tests. We also normalized every test error score by dividing its value by the number of data points. The global error score of a cost function was calculated as the sum of the error scores of all tests. We gathered the error calculations and weights of each test in tables A.2, A.3, A.5 and A.6.

The initial parameters were set to Moreno and coworkers' results, which already closely fit several of the current's dynamics. Naturally, this created a local minimum that was difficult to overcome by the optimization. Therefore, we launched several optimizations with randomly modified parameters (10% variability), along with other strategies specific to the model, such as progressively introducing specific tests in different phases of the optimizations. This created enough differences so that the optimizations could exit the local minimum. The outcomes were controlled by using a specific seed to each randomization ensuring reproducibility.

The endocardial cell action potential model was stimulated during 40-second simulations at the indicated pacing rates in several cost functions as part of the optimizations. Models were paced during 300 seconds at the indicated pacing rates to steady state before starting the optimizations. The final states from these simulations were used as initial states for the endocardial simulations performed during the optimizations.

A. 2. Patch clamp protocols

To reproduce reference patch clamp data from the literature, we created custom code to simulate the same conditions as the experiments, namely, pH, temperature, intra and extracellular sodium concentrations and voltage command protocols. As the intra and extracellular mediums are subject to little change during the length of an experiment, the abovementioned variables were not allowed to evolve.

We integrated the sodium current formulation over the described time and voltage conditions by using Matlab's (The Mathworks.inc, version 2014b) integrated ODE solver for stiff models (function "ode45s"). Current time courses were analyzed as described in the references to generate the required curves. Reference experimental data points were digitized from the original sources using a custom software. The protocols that were used in each cost function are described below.

Temperature dependence in transition rates was calculated using a scaling factor derived from a Q_{10} of 3:

$$T_f = \frac{1}{Q_{10}^{\frac{37-T}{10}}} \qquad \textit{Eq. A.1}$$

Where T represents the temperature (in Celsius).

Patch clamp simulations were usually performed at room temperature (always according to the reference experimental protocol), while action potential simulations were always carried out at 37ºC.

A. 3. Optimization of the wild-type (WT) I_{Na}

We used the Moreno and coworkers' I_{Na} model as a starting point and improved the wild type I_{NaL} formulation by optimizing its time course using new self AP-clamp data[184], further constraining the model to reproduce a flatter time course with increased contribution to the plateau and APD_{90} of the cardiomyocytes.

Table A.1 contains the equations describing the transition rates of the I_{Na} wild type model. Numbers in bold indicate the positions of the fifteen parameters that were inserted for optimization following the scheme of Moreno and coworkers[89,90].

Table A.1. Equations describing the transition rates of the WT and V411M sodium current models. Positions of the parameters (p1, p2, …, p15) to be estimated and optimized were numerated and highlighted in bold. Tf is a temperature factor that was calculated from a Q_{10} of 3.

Transition rates
$\alpha 11 = Tf \cdot \frac{8.5539}{(\boldsymbol{p1}) \cdot e^{-\frac{v}{17.0}} + (\boldsymbol{p2}) \cdot e^{-\frac{v}{150}}}$
$\alpha 12 = Tf \cdot \frac{8.5539}{(\boldsymbol{p1}) \cdot e^{-\frac{v}{15.0}} + (\boldsymbol{p2}) \cdot e^{-\frac{v}{150}}}$
$\alpha 13 = Tf \cdot \frac{8.5539}{(\boldsymbol{p1}) \cdot e^{-\frac{v}{12.0}} + (\boldsymbol{p2}) \cdot e^{-\frac{v}{150}}}$
$\beta 11 = Tf \cdot (\boldsymbol{p3}) \cdot e^{-\frac{v}{20.3}}$
$\beta 12 = Tf \cdot (\boldsymbol{p4}) \cdot e^{-\frac{v-5}{20.3}}$
$\beta 13 = Tf \cdot (\boldsymbol{p5}) \cdot e^{-\frac{v-10}{20.3}}$
$\alpha 3 = Tf \cdot (\boldsymbol{p6}) \cdot e^{-\frac{v}{\boldsymbol{p7}}}$
$\beta 3 = Tf \cdot (\boldsymbol{p8}) \cdot e^{\frac{v}{\boldsymbol{p9}}}$
$\alpha 2 = Tf \cdot (\boldsymbol{p10}) \cdot e^{\frac{v}{\boldsymbol{p11}}}$
$\beta 2 = \frac{\alpha 13 \cdot \alpha 2 \cdot \alpha 3}{\beta 13 \cdot \beta 3}$
$\beta x = (\boldsymbol{p12}) \cdot \alpha 3$
$\alpha x = (\boldsymbol{p13}) \cdot \alpha 2$
$\mu 1 = (\boldsymbol{p14}) \cdot 1.70 \cdot 10^{-7}$
$\mu 2 = (\boldsymbol{p15}) \cdot 5.66 \cdot 10^{-4}$

The optimization of the wild type I_{Na} contained the following tests from Moreno and coworkers[89]: steady state availability, activation, recovery from

inactivation, recovery from use-dependent block and time to half activation. We included three new tests with endocardial simulations designed to fit the APD_{90} restitution curve, to optimize the I_{NaL} current-voltage relationship and the I_{NaL} time course according to the self AP clamp recordings form Horvath and coworkers[184,186] and Hegyi and coworkers[185]. The model was also constrained by the maximum upstroke velocity and the channel Mean Opening Time (MOT). Finally, the amount of charge flowing through the membrane during I_{Naf} (qNaf) was controlled to prevent the model from not depolarizing.

We brought the original Moreno and coworkers' model to steady state at several BCLs (300, 400, 500, 1000, 1500 and 2000 ms) before starting the optimization.

In every iteration, we first stabilized the I_{Na} Markov model by applying a single pulse from -100 mV to -10 mV during 200 ms, followed by a 5-s, -100 mV, resting membrane potential phase. We used the final states from the latter as a starting point for every test involving patch-clamp protocols.

The protocols used to fit the current are described in the bullet point list below:

- Steady state availability: a single 25 ms pulse to -10 mV from a 5-second variable potential test pulse from -120 mV to -40 mV (5 mV intervals) was applied. Peak currents elicited by the second pulse were extracted, normalized to the value at -120 mV and plotted against the pulse voltage.
- Activation: a 25 ms test pulse to variable potentials from -80 mV to 20 mV from a resting potential of -100mV was applied. Then, the resulting channel conductance from the elicited peak currents was calculated, normalized to maximum conductance, and plotted against pulse potential. Conductance values for test potentials above the potential of maximum conductance were set to 1, as in Moreno and coworkers[89].
- Recovery from inactivation: it was evaluated with a standard double-pulse protocol from -100mV to -10mV. The second pulse was delayed with increasingly higher time intervals ranging from 0.1ms to 6s. Peak currents elicited by the second pulse were extracted and normalized to peak currents elicited during the first pulse. Then, they were represented against time intervals.
- Recovery from use-dependent block: First, a train of 300, 25-ms pulses, from -100 mV to -10 mV, at a pacing rate of 25Hz was simulated. Potential was set back to -100mV before a last pulse to -10 mV was applied after a variable delay ranging from 0.5 ms to 9 s.

Maximum current peaks elicited during the second pulse were extracted and normalized to their maximum value. Values were represented against time intervals.

- Tau 50% activation: Tau50 was measured as the time the current took to reach 50% of the maximum peak current at the beginning of each pulse of the activation protocol.
- APD_{90} restitution curve: 40-second simulations with the modified endocardial model at 300, 400, 500, 1000, 1500 and 2000 ms BCLs were performed. Every simulation was carried out in parallel and the last beat was saved for further analysis. We obtained the APD_{90} of saved beats by calculating the interval from the instant of maximum upstroke velocity to the time of 90% repolarization. The data were plotted against BCL and the results were compared to the O'Hara-Rudy model's reference[98].
- I_{NaL} time course: a train of 40 stimuli at 1 Hz was applied to the modified isolated endocardial model and the last beat was saved for further analysis. Three parameters from the I_{NaL} time course were extracted as seen in Figure A.1. Firstly, the "dome" was defined as the maximum late sodium current (registered after the fast sodium current had inactivated). Secondly, the "valley" was defined as the minimum current between peak I_{Naf} and the dome. Finally, the half-time taken by the current to reach the dome from the valley was defined as t_1⁄2. Both valley and t_1⁄2 values were normalized to the current and time of the dome, respectively. Reference dome current was set to to 0.34 pA/pF[107], reference dome-to-valley value to 0.59 and reference t_1⁄2 value to 0.63[184].
- Maximum upstroke velocity was extracted from simulations at 1Hz as the maximum derivative of the action potential time course during phase 0 (depolarization). The target value was set to 250 V/s[98].
- MOT was calculated as in Moreno and coworkers[89], which was included in the code the authors made available.

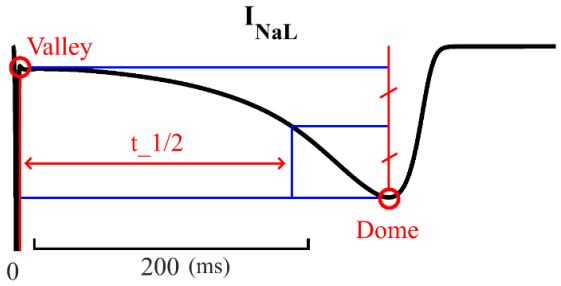

Figure A.1. Parameters (red) evaluated during the optimization of I_{NaL}'s time course. Valley was determined by selecting the lowest current after I_{Na} peak and normalized to the dome, the value of maximum I_{NaL}. The valley to dome half time was measured as the time that took the current to rise to half of the dome current, normalized to the time between valley and dome.

The late to fast proportion was controlled as the maximum I_{NaL} over peak I_{Naf} by means of the protocols used by from Clancy and coworkers[243], but this test was only used to assess whether the simulations were yielding consistent results in prior tests, therefore not being included in the total error score. The reference value was 0.1% as in Moreno and coworkers[90].

Table A.2 contains detailed information about the calculation of the error scores of each test in the cost function as well as the weights that were applied during the optimization of the WT model.

Table A.2. I_{Na} WT model optimization error calculations and weights in the cost function. The words containing "data" and "reference" indicate vectors containing the results of our tests and the experimental reference values, respectively. N is the number of samples. APD refers to a vector containing the APD_{90}s of simulations at BCLs 300, 400, 500, 1000, 1500 and 2000 ms. Mean open time was adjusted to 0.5 at V=-30 mV.

Wild type optimization

Test name	Error calculation	Weight
Steady state availability	(100·sum(data-reference))^2/N	2
Activation	(100·sum(data-reference))^2/N	2
Recovery from inactivation	(100·sum(data-reference))^2/N	1

Recovery from use-dependent block	(100·sum(data-reference))^2/N	0.04
Mean opening time	abs(2 - α2+β13+αx)	1
Tau 50% activation	(100·sum(data-reference))^2/N	1
I_{NaL} time course at BCL 1000 ms	100·((dome-reference_dome)^2+(valley-reference_valley)^2+(time_50-reference_time50))	5
APD_{90} tests (at BCL 300, 400, 500, 1000, 1500 and 2000 ms)	sum(APD_data-APD_reference)^2	BCL 500 ms: 2.5 Others: 1
Max dVdt	sum(dVdt_data-dVdt_reference)^2	1
I_{NaL} current-voltage relationship	(100·sum(data-reference))^2/N	1

Table A.3. I_{Na} V411M mutation model optimization error calculations and weights in the cost function. The words containing "data" and "reference" indicate vectors containing the results of our and the reference target values, respectively. N is the number of samples.

V411M mutation optimization

Test name	**Error calculation**	**Weight**
Activation	((Vh_data-Vh_reference)^2+(slope_data-slope_reference)^2)/2	1
Activation time constant (tau)	sum(Tau_data-tau_reference)^2/N	Positions 4 to 8: 5 Others: 1
Inactivation	((Vh_data-Vh_reference)^2+(slope_data-slope_reference)^2)/2	10
current-voltage relationship	(100·sum(data-reference))^2/N	Positions 6 to 9 from both ends: 2 RestOthers: 1

Prolongation in endocardial cell (%)	(Prolongation_data-Prolongation_reference)^2	2.5
qNaf (to prevent no depolarization)	10^6·(WT_qNaf-V411M_qNaf)^2	2

A. 4. Optimization of the SCN5A V411M mutation

We ought to create a model of the V411M mutation by reproducing the available clinical and experimental data[173–175]. The same parameter locations were used to optimize the transition rates of the mutated V411M I_{Na} model (see Table A.1).

Optimization of the SCN5A V411M mutation model included protocols testing the activation, inactivation, inactivation time constants, current-voltage relationship, and prolongation of the APD_{90}. Before the optimization, we paced the wild type endocardial action potential model to steady state.

One iteration of the cost function was run before starting the optimization in order to create a starting set of curves corresponding to the wild type model. Target values were generated by applying the relative wild-type-to-mutation changes in current dynamics observed by Horne and coworkers[173].

The protocols that we used to fit the mutated current are described in the bullet point list below:

- Activation: a 200-ms pulse to a variable potential from -80 mV to 30 mV was applied and the resulting maximum conductances were extracted from the elicited peak currents and normalized to their maximum value. The data were represented against the pulse potential and fitted to the following Boltzmann equation:

$$\frac{G}{G_{\max}} = \frac{1}{1 + e^{\frac{V_h - V}{s}}} \qquad \textit{Eq. A.2}$$

  Where V_h is the half-maximal voltage and s is the slope of the curve. During the optimizations, V_h and s alterations from the wild type model were calculated to assess this test's error score.

- Inactivation: a variable voltage pre-pulse of 300 ms from -160 mV to 0 mV from a resting potential of -110 mV, followed by a 20-ms pulse to -20 mV, was simulated. Then, peak currents elicited during the second pulse were extracted, normalized to their maximum value and plotted against the pre-pulse potential. Finally, the curve was fitted to a Boltzmann equation (see activation protocols) and V_h and slope alterations were extracted.
- Mean inactivation time constants: time courses of the inactivation current from the activation protocols were isolated (starting from maximum peak current to the end of the pulse) and fitted to a single exponential decay.
- Current-voltage relationship: a variable voltage 250-ms pulse from -80 mV to 40 mV from a resting potential of -110 mV was applied. Elicited peak currents were extracted, normalized to their maximum value and plotted against the pulse potential.
- APD_{90} Prolongation: 40-beat simulations with the heterozygous SCN5A V411M isolated endocardial model (50% wild type and 50% mutated currents) were run and the last beat was saved for further analysis. Prolongation of the APD_{90} was measured relative to the wild type model. Target prolongation was set to a 16% as a surrogate of the QT prolongation.

Table A.3 contains detailed information about the calculation of the error scores of each test in the cost function as well as the weights that were applied during the optimization of the SCN5A V411M model.

A. 5. Optimization of Flecainide

We ought to give insight into the mechanisms that drive flecainide's effectiveness as reported clinically[174,175]. The Moreno and coworkers' Markov formulation of flecainide revealed an I_{NaL} IC_{50} of around 90 μM, inconsistent with the new findings[222,232]. Therefore, we ought to refit flecainide's I_{NaL} blocking dynamics to better reproduce the latest data available concerning its blocking power.

Table A.4 contains the transition rate names and equations describing the dynamics of neutral and charged fractions of flecainide, as well as equations containing drug affinities to specific states. In this table, transition rates belonging to the charged fraction were marked with a plus sign while those belonging to the neutral fraction were marked with an "n". Affinities marked with "on" describe the binding of the drug while "off" affinities describe the

unbinding of the drug. Affinities for the inactive, neutral, closed or bursting states were marked with "i", "n", "c" or "b", respectively. Open state affinities have no special naming convention.

Optimization of flecainide model consisted of the following tests: Steady-state availability, recovery from use-dependent block, I_{Naf} concentration and use-dependent block curves at 0.2, 1 and 3 Hz[108], I_{NaL} IC_{50}[222], and APD_{90} prolongation[130]. The isolated endocardial cellular model was paced to steady state in drug-free conditions previously to the optimization.

Caballero and coworkers[220] found that flecainide enhanced the inward rectifier current (I_{K1}) with a maximum increase of +53.9% and an EC_{50} of 0.8 µM at -50 mV. Therefore, according to the Hill formalism, we estimated that 1.5 µM therapeutic Flecainide[130] should increase its conductance by a 51%. Since the current is mostly active at these potentials, we modeled this effect as a scalar factor multiplying G_{K1}. Flecainide also blocked the rapid potassium delayed rectifier current (I_{Kr}) with an IC_{50} of 3.91 µM[221] reducing its conductance to a 72.3% at 1.5 µM.

Table A.4. Equations describing the transition rates and affinities of the flecainide model. Positions of the parameters (p1, p2, ..., p16) to be optimized were numerated and highlighted in bold.

Transition rates	equations
α11+ and α11n	$\alpha 11$
α12+ and α12n	$\alpha 12$
β11+ and β11n	$\beta 11$
β12+ and β12n	$\beta 12$
αx+	$(\boldsymbol{p1}) \cdot \alpha x$
βx+	$(\boldsymbol{p2}) \cdot \beta x$
α13+	$(\boldsymbol{p3}) \cdot \alpha 13$
α2+	$(\boldsymbol{p4}) \cdot \alpha 2$
β3+	$(\boldsymbol{p5}) \cdot \beta 3$
α3+	$(\boldsymbol{p6}) \cdot \alpha 3$
α4+	$(\boldsymbol{p7}) \cdot \alpha 2$
β4+	$(\boldsymbol{p8}) \cdot \alpha 3$
αxn	$(\boldsymbol{p9}) \cdot \alpha x$
α13n	$(\boldsymbol{p10}) \cdot \alpha 13$
α2n	$(\boldsymbol{p11}) \cdot \alpha 2$
β3n	$(\boldsymbol{p12}) \cdot \beta 3$

α4n	$(\boldsymbol{p13}) \cdot \alpha 2$
β4n	$(\boldsymbol{p14}) \cdot \alpha 3$
k_on = kc_on	$drug_{charged} \cdot diffusion$
k_off = kc_off	$(\boldsymbol{p15}) \cdot 10^{-6} \cdot e^{\frac{-0.7*V*F}{R*T}} * diffusion$
kb_on = kcb_on	k_on
kb_off = kcb_off	$(\boldsymbol{p16}) \cdot 10^{-6} \cdot e^{\frac{-0.7*V*F}{R*T}} * diffusion$
kn_on	$drug\_neutral \cdot diffusion$
kn_off	$400 \cdot 10^{-6} \cdot diffusion$
kni_on	kn_on
kni_off	$5.4 \cdot 10^{-6} \cdot diffusion$
knc_on	kn_on
knc_off	$800 * 10^{-6} \cdot diffusion$
diffusion	$5500\ M^{-1} \cdot ms^{-1}$

The protocols that we used to fit flecainide's model are described in the bullet point list below:

- Steady state availability: the same protocol as in the wild-type model was used to obtain the corresponding curve at 10 μM Flecainide.
- Recovery from use-dependent block: First, a train of 100 pulses at 25 Hz from -100mV to -10mV was simulated. Then, a second identical pulse was applied after a variable interval from 0.5 to 9s at -100mV. Flecainide concentration was set to 10 μM. Peak currents elicited from the delayed pulse were extracted, normalized to the first pulse's elicited current and plotted against time intervals.
- I_{Naf} block curves: The standard protocol consisted of a 30-ms pulse from -100 mV to -20 mV. It was applied 40 times at a rate of 0.2Hz or 60 times at a rate of 1 and 3 Hz. The maximum peak current elicited by the last pulse was extracted for increasing flecainide concentrations and normalized to drug-free conditions.
- I_{NaL} IC_{50}: From a -120mV pulse of 200 ms duration, we applied a 40-ms pulse to -15 mV followed by a second 200-ms pulse to 40 mV. I_{NaL} was measured as the maximum I_{Na} current elicited during a 100-ms ramp from 40 mV to -95 mV (-1.35 V/s) that followed the beforementioned pulses. The protocol was repeated at increasingly higher drug concentrations until 50% block of the control current (drug-free) was reached. The corresponding concentration was retrieved as the I_{NaL} IC_{50}.

- APD_{90} Prolongation: simulations with the isolated cellullar model were performed to test the effects of flecainide every iteration. A train of 40 beats at 1 Hz at 1.5 μM therapeutic flecainide was applied. APD_{90} from the last beat was normalized to drug free conditions to obtain drug-induced prolongation. Target prolongation was adjusted to be as low as possible according to flecainde's clinical and experimental results[130,229].
- Because flecainide has a pKa of 9.3[89], this drug is 99% charged under physiological conditions. Before optimizing the complete drug model – in a first phase – we optimized only neutral flecainide for dose-dependent use-dependent block (see below) at 10 Hz and recovery from use-dependent block for time intervals ranging from 0.5s to 7s. Then, neutral drug parameters were held constant while the remaining parameters were optimized using all protocols in two additional phases. The second phase included the complete drug versions of the abovementioned protocols as well as steady state availability, recovery from use-dependent block and the I_{Naf} IC_{50} use dependence. Finally, the third phase added I_{NaL} IC_{50} and APD_{90} prolongation to the test batch.
- Dose-dependent use-dependent block for neutral flecainide: We simulated a train of 300, 25-ms, pulses at 10Hz from -100mV to -10mV. We normalized the current elicited by the last pulse under increasing neutral flecainide concentrations and normalized the value to the first pulse. We plotted the results against drug concentration.

Table A.5 contains detailed information about the calculation of the error scores of each test in the cost function as well as the weights in the optimization of the flecainide model.

Table A.5. Flecainide model optimization error calculations and weights of the cost function. The words containing "data" and "reference" indicate vectors containing the results of our tests and the reference experimental values, respectively. The I_{NaL} IC_{50} test was not shown. N is the number of samples.

Flecainide optimization

Test name	Error calculation	Weight
Steady state availability	(100·sum(data-reference))^2/N	2
Dose-dependent use-dependent block	(100·sum(data-reference))^2/N	1

Recovery from use-dependent block	(100·sum(data-reference))^2/N	1
Frequency-dependent INaf block at 0.2 Hz	(100·sum(IC50_data-IC50_reference))^2/N	1
Frequency-dependent INaf block at 1 Hz	(100·sum(IC50_data-IC50_reference))^2/N	1
Frequency-dependent INaf block at 3 Hz	(100·sum(IC50_data-IC50_reference))^2/N	1
Prolongation in endocardial cell (%)	10·(Prolongation)^2	1
INaL IC50	1000·(INaL_IC50-INaL_IC50_reference)^2	1

A. 6. Optimization of Ranolazine

Transition velocities and affinities that describe ranolazines' binding, unbinding and current dynamics were determined as described in Table A.6.

Optimization of ranolazine considered the following test protocols: steady-state availability, tonic block of peak and late sodium current, use-dependent block, recovery from use-dependent block and frequency-dependent use-dependent block. Diffusion and affinities for the normal and bursting states were set as in the original model and they were not modified.

The protocols that we used to fit ranolazine's model are described in the bullet point list below:

- Steady state availability: a 100 ms pulse to -10 mV from a variable conditioning potential from -120 mV to -40 mV was applied and the resulting peak current under exposure to 10 μM ranolazine was extracted. Values were normalized to drug-free conditions and plotted against conditioning pulse potential.
- Tonic block: A single 500-ms pulse to -10 mV from a resting potential of -100 mV was applied to evaluate the effect of increasing ranolazine concentrations. I_{Naf} was calculated using the elicited peak current, while I_{NaL} was measured using the remaining current at the end of the pulse. Both values were normalized to drug-free conditions and plotted against drug concentrations to obtain the corresponding IC_{50}s.

- Use-dependent block: 300 25 ms pulses to -10 mV from a resting potential of -100 mV at a rate of 5 Hz and under exposure to increasing ranolazine concentrations were applied. The peak current elicited by the last pulse was extracted, normalized to drug-free conditions and plotted against drug concentrations.
- Recovery from use-dependent block: This protocol is similar to flecainide's recovery from use-dependent block protocol. Intervals ranged from 0.1 s to 10 s and ranolazine concentration was set to 10 μM.

Frequency-dependent use-dependent block: A train of 300 square 25-ms pulses from -100 mV to -10 mV was applied at 1 Hz, 2 Hz, 5 Hz and 10 Hz rates under exposure to 100 μM ranolazine. Peak sodium currents elicited by the last pulse were extracted and normalized to drug-free conditions. Then, they were plotted against pacing rate. Table A.7 contains detailed information about the calculation of the error scores of each test in the cost function as well as the weights that were applied during the optimization of the ranolazine model.

Table A.6. Equations describing the transition rates and affinities of the ranolazine model. Positions of the parameters (p1, p2, ..., p12) to be optimized were numerated and highlighted in bold.

Transition rates	equations
α11+ and α11n	$\alpha 11$
α12+ and α12n	$\alpha 12$
β11+ and β11n	$\beta 11$
β12+ and β12n	$\beta 12$
αx+	$(\boldsymbol{p1}) \cdot \alpha x$
βx+	$(\boldsymbol{p2}) \cdot \beta x$
α13+	$(\boldsymbol{p3}) \cdot \alpha 13$
α2+	$(\boldsymbol{p4}) \cdot \alpha 2$
β3+	$(\boldsymbol{p5}) \cdot \beta 3$
α3+	$(\boldsymbol{p6}) \cdot \alpha 3$
αxn	$(\boldsymbol{p7}) \cdot \alpha x$
α13n	$(\boldsymbol{p8}) \cdot \alpha 13$
α2n	$(\boldsymbol{p9}) \cdot \alpha 2$
β3n	$(\boldsymbol{p10}) \cdot \beta 3$
k_on = kc_on	$drug_{charged} \cdot diffusion$
k_off = kc_off	$(\boldsymbol{p11}) \cdot 10^{-6} \cdot e^{\frac{-0.7*V*F}{R*T}} * diffusion$

kb_on = kcb_on	k_on
kb_off = kcb_off	$(\boldsymbol{p12}) \cdot 10^{-6} \cdot e^{\frac{-0.7*V*F}{R*T}} * diffusion$
kn_on	$drug\_neutral \cdot diffusion$
kn_off	$400 \cdot 10^{-6} \cdot diffusion$
kni_on	kn_on
kni_off	$5.4 \cdot 10^{-6} \cdot diffusion$
knc_on	kn_on
knc_off	$800 * 10^{-6} \cdot diffusion$
diffusion	$5500\ M^{-1} \cdot ms^{-1}$

Table A.7. Ranolazine model optimization error calculations and weights in the cost function. The words containing "data" and "reference" indicate vectors containing the results of our and the reference experimental values, respectively. N is the number of samples.

Ranolazine optimization

Test name	Error calculation	Weight
Steady state availability	(100·sum(data-reference))^2/N	1
Tonic block of INaf	(100·sum(data-reference))^2/N	1
Tonic block of INaL	(100·sum(data-reference))^2/N	1
Recovery from use-dependent block	(100·sum(data-reference))^2/N	1
Frequency-dependent use-dependent block	(100·sum(data-reference))^2/N	1

References

1. European Commission. CVD statistics. https://ec.europa.eu/eurostat/statistics-explained/index.php/Cardiovascular_diseases_statistics (2019).

2. Schwartz, P. J. *et al.* Prevalence of the congenital long-qt syndrome. *Circulation* **120**, 1761–1767 (2009).

3. Steinberg, C. *et al.* Cardiac Abnormalities in First-Degree Relatives of Unexplained Cardiac Arrest Victims. *Circ. Arrhythmia Electrophysiol.* **9**, (2016).

4. Kumar, S. *et al.* Familial cardiological and targeted genetic evaluation: Low yield in sudden unexplained death and high yield in unexplained cardiac arrest syndromes. *Hear. Rhythm* **10**, 1653–1660 (2013).

5. Wallace, E. *et al.* Long QT Syndrome: Genetics and Future Perspective. *Pediatric Cardiology* vol. 40 1419–1430 (2019).

6. Ackerman, M. J. *et al.* HRS/EHRA expert consensus statement on the state of genetic testing for the channelopathies and cardiomyopathies. *Hear. Rhythm* **8**, 1308–39 (2011).

7. Priori, S. G. *et al.* 2015 ESC Guidelines for the management of patients with ventricular arrhythmias and the prevention of sudden cardiac death. *Eur. Heart J.* **36**, 2793–2867 (2015).

8. Bengel, P., Ahmad, S. & Sossalla, S. Inhibition of Late Sodium Current as an Innovative Antiarrhythmic Strategy. *Curr. Heart Fail. Rep.* **14**, 179–186 (2017).

9. Bohnen, M. S. *et al.* Molecular pathophysiology of congenital long QT syndrome. *Physiol. Rev.* **97**, 89–134 (2017).

10. Makita, N. *et al.* The E1784K mutation in SCN5A is associated with mixed clinical phenotype of type 3 long QT syndrome. *J. Clin. Invest.* **118**, 2219–2229 (2008).

11. Abdelsayed, M., Peters, C. H. & Ruben, P. C. Differential thermosensitivity in mixed syndrome cardiac sodium channel mutants. *J. Physiol.* **593**, 4201–23 (2015).

12. Sarganas, G. *et al.* Epidemiology of symptomatic drug-induced long QT syndrome and torsade de pointes in Germany. *Europace* **16**, 101–108 (2014).

13. Arunachalam, K., Lakshmanan, S., Maan, A., Kumar, N. & Dominic, P. Impact of Drug Induced Long QT Syndrome: A Systematic Review. *J. Clin. Med. Res.* **10**, 384–390 (2018).

14. ICH. ICH harmonised tripartite guideline. The nonclinical evaluation

of the potential for delayed ventricular repolarization (QT interval prolongation) by human pharmaceuticals S7B. (2005).

15. ICH. Harmonised Tripartite Guideline. The Clinical Evaluation of QT/QTc Interval Prolongation and Proarrhythmic Potential for Non-Antiarrhythmic Drugs E14. (2005).

16. Darpo, B. *et al.* Cardiac safety research consortium: Can the thorough QT/QTc study be replaced by early QT assessment in routine clinical pharmacology studies? Scientific update and a research proposal for a path forward. *American Heart Journal* vol. 168 262–272 (2014).

17. CIPA. https://cipaproject.org/.

18. Guyton, A. C. & Hall, J. E. *Guyton and Hall Textbook of Medical Physiology, 12th edition*. (2006).

19. Tortora, G. J. & Derrickson, B. H. *Principles of Anatomy and Physiology, 15th Edition*. (2016).

20. Anderson, R. H., Yanni, J., Boyett, M. R., Chandler, N. J. & Dobrzynski, H. The anatomy of the cardiac conduction system. *Clinical Anatomy* vol. 22 99–113 (2009).

21. Grant, A. O. Cardiac ion channels. *Circ. Arrhythm. Electrophysiol.* **2**, 185–94 (2009).

22. Martinez-Mateu, L. *et al.* Factors affecting basket catheter detection of real and phantom rotors in the atria: A computational study. *PLoS Comput. Biol.* **14**, (2018).

23. Anyukhovsky, E. P., Sosunov, E. A. & Rosen, M. R. Regional differences in electrophysiological properties of epicardium, midmyocardium, and endocardium: In vitro and in vivo correlations. *Circulation* **94**, 1981–1988 (1996).

24. Antzelevitch, C. *et al.* The M cell: its contribution to the ECG and to normal and abnormal electrical function of the heart. *J. Cardiovasc. Electrophysiol.* **10**, 1124–52 (1999).

25. Wilson, L. D., Jennings, M. M. & Rosenbaum, D. S. Point: M cells are present in the ventricular myocardium. *Hear. Rhythm* **8**, 930–933 (2011).

26. Zhu, L. *et al.* Automatic delineation of the myocardial wall from CT images via shape segmentation and variational region growing. *IEEE Trans. Biomed. Eng.* **60**, 2887–2895 (2013).

27. Antzelevitch, C. & Fish, J. Electrical heterogeneity within the ventricular wall. *Basic Res. Cardiol.* **96**, 517–527 (2001).

28. Shigekawa, M. & Iwamoto, T. Cardiac Na $^{+}$ -Ca $^{2+}$ Exchange. *Circ. Res.* **88**, 864–876 (2001).

29. Bueno-Orovio, A., Sánchez, C., Pueyo, E. & Rodriguez, B. Na/K pump regulation of cardiac repolarization: Insights from a systems biology approach. *Pflugers Archiv European Journal of Physiology* vol. 466 183–193 (2014).

30. Roden, D. M. & Kupershmidt, S. From genes to channels: Normal mechanisms. *Cardiovascular Research* vol. 42 318–326 (1999).

31. Balser, J. R. The cardiac sodium channel: Gating function and molecular pharmacology. in *Journal of Molecular and Cellular Cardiology* vol. 33 599–613 (Academic Press, 2001).

32. Marban, E., Yamagishi, T. & Tomaselli, G. F. Structure and function of voltage-gated sodium channels. *Journal of Physiology* vol. 508 647–657 (1998).

33. Feher, J. The Cardiac Action Potential. in *Quantitative Human Physiology* 528–536 (Elsevier, 2012). doi:10.1016/B978-0-12-800883-6.00049-5.

34. Bravený, P. Heart, calcium and time. *Exp. Clin. Cardiol.* **7**, 3 (2002).

35. Sicouri, S. & Antzelevitch, C. A subpopulation of cells with unique electrophysiological properties in the deep subepicardium of the canine ventricle. The M cell. *Circ. Res.* **68**, 1729–1741 (1991).

36. Li, W. *et al.* Larger rate dependence of late sodium current in cardiac Purkinje cells: A potential link to arrhythmogenesis. *Hear. Rhythm* **14**, 422–431 (2017).

37. Dusturia, N., Choi, S. W., Song, K. S. & Lim, K. M. Effect of myocardial heterogeneity on ventricular electro-mechanical responses: A computational study. *Biomed. Eng. Online* **18**, (2019).

38. Tamura, T. & Chen, W. *Seamless healthcare monitoring: Advancements in wearable, attachable, and invisible devices*. *Seamless Healthcare Monitoring: Advancements in Wearable, Attachable, and Invisible Devices* (2017). doi:10.1007/978-3-319-69362-0.

39. Brunton, L. & Hilal-Dandan, R. *Goodman and Gilman Manual of Pharmacology and Therapeutics, Second Edition*. (2008). doi:10.1036/0071443436.

40. Benjamin, E. J. *et al. Heart Disease and Stroke Statistics-2019 Update: A Report From the American Heart Association*. *Circulation* vol. 139 (2019).

41. Reumann, M., Gurev, V. & Rice, J. J. Computational modeling of cardiac disease: Potential for personalized medicine. *Per. Med.* **6**, 45–66 (2009).

42. Lopez, E. O. & Jan, A. Cardiovascular Disease. (2019).

43. Csige, I. *et al.* The Impact of Obesity on the Cardiovascular System. *J. Diabetes Res.* **2018**, (2018).

44. Malamed, S. F. & Orr, D. L. Angina Pectoris. in *Medical Emergencies in the Dental Office* vol. 8 440–455 (Elsevier, 2015).

45. Tanai, E. & Frantz, S. Pathophysiology of heart failure. *Compr. Physiol.* **6**, 187–214 (2016).

46. Ongstad, E. L. & Gourdie, R. G. Can heart function lost to disease be regenerated by therapeutic targeting of cardiac scar tissue? *Seminars in Cell and Developmental Biology* vol. 58 41–54 (2016).

47. Wu, J., Wu, J. & Zipes, D. P. Early Afterdepolarizations, U Waves, and Torsades de Pointes. *Circulation* **105**, 675–676 (2002).

48. Redfern, W. S. *et al.* Relationships between preclinical cardiac electrophysiology, clinical QT interval prolongation and torsade de pointes for a broad range of drugs: Evidence for a provisional safety margin in drug development. *Cardiovasc. Res.* **58**, 32–45 (2003).

49. Vicente, J. *et al.* Mechanistic Model-Informed Proarrhythmic Risk Assessment of Drugs: Review of the "CiPA" Initiative and Design of a Prospective Clinical Validation Study. *Clin. Pharmacol. Ther.* **103**, 54–66 (2018).

50. Witchel, H. J. Drug-induced hERG Block and Long QT Syndrome. *Cardiovasc. Ther.* **29**, 251–259 (2011).

51. Moreno, J. D. & Clancy, C. E. Pathophysiology of the cardiac late Na current and its potential as a drug target. *J. Mol. Cell. Cardiol.* **52**, 608–619 (2012).

52. Campos, F. O., Shiferaw, Y., Vigmond, E. J. & Plank, G. Stochastic spontaneous calcium release events and sodium channelopathies promote ventricular arrhythmias. *Chaos* **27**, 093910 (2017).

53. Echt, D. S. *et al.* Mortality and Morbidity in Patients Receiving Encainide, Flecainide, or Placebo: The Cardiac Arrhythmia Suppression Trial. *N. Engl. J. Med.* **324**, 781–788 (1991).

54. Stevenson, W. G. Ventricular scars and ventricular tachycardia. *Transactions of the American Clinical and Climatological Association* vol. 120 403–412 (2009).

55. WILLIAMS, E. M. V. A Classification of Antiarrhythmic Actions Reassessed After a Decade of New Drugs. *J. Clin. Pharmacol.* **24**, 129–147 (1984).

56. Roden, D. M. Cellular basis of drug-induced torsades de pointes. *Br. J. Pharmacol.* **154**, 1502–7 (2008).

57. Woosley, R. & Romero, K. www.Crediblemeds.org, QTdrugs List, AZCERT, Inc. 1822 Innovation Park Dr., Oro Valley, AZ 85755.

58. Kramer, J. *et al.* MICE models: superior to the HERG model in predicting Torsade de Pointes. *Sci. Rep.* **3**, 2100 (2013).

59. COURTEMANCHE, M. & WINFREE, A. T. RE-ENTRANT ROTATING WAVES IN A BEELER–REUTER BASED MODEL OF TWO-DIMENSIONAL CARDIAC ELECTRICAL ACTIVITY. *Int. J. Bifurc. Chaos* **01**, 431–444 (1991).

60. Panfilov, A. V. & Holden, A. V. *Computational Biology of the Heart*. (1997).

61. Davies, M. R. *et al.* Recent developments in using mechanistic cardiac modelling for drug safety evaluation. *Drug Discovery Today* vol. 21 924–938 (2016).

62. Sadrieh, A. *et al.* Multiscale cardiac modelling reveals the origins of notched T waves in long QT syndrome type 2. *Nat. Commun.* **5**, 1–11 (2014).

63. Cho, C. R., Labow, M., Reinhardt, M., van Oostrum, J. & Peitsch, M. C. The application of systems biology to drug discovery. *Current Opinion in Chemical Biology* vol. 10 294–302 (2006).

64. Noble, D. Modeling the heart. *Physiology* **19**, 191–197 (2004).

65. Mirams, G. R. *et al.* Simulation of multiple ion channel block provides improved early prediction of compounds' clinical torsadogenic risk. *Cardiovasc. Res.* **91**, 53–61 (2011).

66. Mirams, G. R. *et al.* Prediction of Thorough QT study results using action potential simulations based on ion channel screens. *J. Pharmacol. Toxicol. Methods* **70**, 246–54 (2014).

67. Davies, M. R. *et al.* An in silico canine cardiac midmyocardial action potential duration model as a tool for early drug safety assessment. *Am. J. Physiol. Heart Circ. Physiol.* **302**, 1466–1480 (2012).

68. Mistry, H. B., Davies, M. R. & Di Veroli, G. Y. A new classifier-based strategy for in-silico ion-channel cardiac drug safety assessment. *Front. Pharmacol.* **6**, 59 (2015).

69. Beattie, K. A. *et al.* Evaluation of an in silico cardiac safety assay: Using ion channel screening data to predict QT interval changes in the rabbit ventricular wedge. *J. Pharmacol. Toxicol. Methods* **68**, 88–96 (2013).

70. Boyle, P. M. *et al.* Computationally guided personalized targeted ablation of persistent atrial fibrillation. *Nat. Biomed. Eng.* **3**, 870–879 (2019).

71. Hodgkin, A. L. & Huxley, A. F. A quantitative description of membrane current and its application to conduction and excitation in nerve. *J. Physiol.* **117**, 500–544 (1952).

72. Schwiening, C. J. A brief historical perspective: Hodgkin and Huxley. *Journal of Physiology* vol. 590 2571–2575 (2012).

73. Fink, M. *et al.* Cardiac cell modelling: Observations from the heart of the cardiac physiome project. *Prog. Biophys. Mol. Biol.* **104**, 2–21 (2011).

74. Sheets, M. F. & Ten Eick, R. E. Whole-Cell Voltage Clamp of Cardiac Sodium Current. in *Methods in Neurosciences* vol. 19 169–188 (Academic Press, 1994).

75. MALTSEV, V. & UNDROVINAS, A. A multi-modal composition of the late Na+ current in human ventricular cardiomyocytes. *Cardiovasc. Res.* **69**, 116–127 (2006).

76. Undrovinas, A. I., Maltsev, V. A., Kyle, J. W., Silverman, N. & Sabbah, H. N. Gating of the late Na+ channel in normal and failing human myocardium. *J. Mol. Cell. Cardiol.* **34**, 1477–1489 (2002).

77. Moreno, J. D., Lewis, T. J. & Clancy, C. E. Parameterization for In-Silico Modeling of Ion Channel Interactions with Drugs. *PLoS One* **11**, e0150761 (2016).

78. Basharin, G. P., Langville, A. N. & Naumov, V. A. The life and work of A.A. Markov. in *Linear Algebra and Its Applications* vol. 386 3–26 (North-Holland, 2004).

79. Colquhoun, D. & Hawkes, A. G. The Principles of the Stochastic Interpretation of Ion-Channel Mechanisms. in *Single-Channel Recording* 397–482 (Springer US, 1995). doi:10.1007/978-1-4419-1229-9_18.

80. Linaro, D. & Giugliano, M. Markov Models of Ion Channels. in *Encyclopedia of Computational Neuroscience* 1649–1660 (Springer New York, 2015). doi:10.1007/978-1-4614-6675-8_131.

81. Clancy, C. E. & Rudy, Y. Na+ channel mutation that causes both

Brugada and long-QT syndrome phenotypes: A simulation study of mechanism. *Circulation* **105**, 1208–1213 (2002).

82. Bezanilla, F. & Armstrong, C. M. Inactivation of the sodium channel: I. sodium current experiments. *J. Gen. Physiol.* **70**, 549–566 (1977).

83. Armstrong, C. M. & Bezanilla, F. Inactivation of the sodium channel: II. gating current experiments. *J. Gen. Physiol.* **70**, 567–590 (1977).

84. Grant, a O. Molecular biology of sodium channels and their role in cardiac arrhythmias. *Am. J. Med.* **110**, 296–305 (2001).

85. Hartmann, H. A., Tiedeman, A. A., Chen, S. F., Brown, A. M. & Kirsch, G. E. Effects of III-IV linker mutations on human heart Na+ channel inactivation gating. *Circ. Res.* **75**, 114–122 (1994).

86. Motoike, H. K. *et al.* The Na+ Channel Inactivation Gate Is a Molecular Complex: A Novel Role of the COOH-terminal Domain. *J. Gen. Physiol.* **123**, 155–165 (2004).

87. Rudy, Y. & Silva, J. R. Computational biology in the study of cardiac ion channels and cell electrophysiology. *Q. Rev. Biophys.* **39**, 57–116 (2006).

88. Zhu, Z. I. & Clancy, C. E. L-type Ca2+ channel mutations and T-wave alternans: a model study. *AJP Hear. Circ. Physiol.* **293**, H3480--H3489 (2007).

89. Moreno, J. D. *et al.* A computational model to predict the effects of class I anti-arrhythmic drugs on ventricular rhythms. *Sci. Transl. Med.* **3**, 98ra83 (2011).

90. Moreno, J. D. *et al.* Ranolazine for congenital and acquired late INa-linked arrhythmias: in silico pharmacological screening. *Circ. Res.* **113**, e50–e61 (2013).

91. Yang, P.-C. *et al.* In silico prediction of drug therapy in catecholaminergic polymorphic ventricular tachycardia. *J. Physiol.* **594**, 567–93 (2016).

92. Noble, D. A modification of the Hodgkin—Huxley equations applicable to Purkinje fibre action and pacemaker potentials. *J. Physiol.* **160**, 317–352 (1962).

93. Fink, M. & Noble, D. Pharmacodynamic effects in the cardiovascular system: The modeller's view. in *Basic and Clinical Pharmacology and Toxicology* vol. 106 243–249 (2010).

94. Davies, M. R. *et al.* Recent developments in using mechanistic cardiac modelling for drug safety evaluation. *Drug Discov. Today* **21**, 924–38

(2016).

95. ten Tusscher, K. H. W. J. A model for human ventricular tissue. *AJP Hear. Circ. Physiol.* **286**, H1573--H1589 (2003).

96. Courtemanche, M., Ramirez, R. J. & Nattel, S. Ionic mechanisms underlying human atrial action potential properties: Insights from a mathematical model. *Am. J. Physiol. - Hear. Circ. Physiol.* **275**, (1998).

97. Grandi, E., Pasqualini, F. S. & Bers, D. M. A novel computational model of the human ventricular action potential and Ca transient. *J. Mol. Cell. Cardiol.* **48**, 112–121 (2010).

98. O'Hara, T., Virág, L., Varró, A. & Rudy, Y. Simulation of the undiseased human cardiac ventricular action potential: model formulation and experimental validation. *PLoS Comput. Biol.* **7**, e1002061 (2011).

99. Rush, S. & Larsen, H. A practical algorithm for solving dynamic membrane equations. *IEEE Trans. Biomed. Eng.* **25**, 389–392 (1978).

100. Victorri, B., Vinet, A., Roberge, F. A. & Drouhard, J. P. Numerical integration in the reconstruction of cardiac action potentials using Hodgkin-Huxley-type models. *Comput. Biomed. Res.* **18**, 10–23 (1985).

101. Mayourian, J., Sobie, E. A. & Costa, K. D. An Introduction to Computational Modeling of Cardiac Electrophysiology and Arrhythmogenicity. *Methods Mol. Biol.* **1816**, 17–35 (2018).

102. Benson, A. P., Aslanidi, O. V., Zhang, H. & Holden, A. V. The canine virtual ventricular wall: a platform for dissecting pharmacological effects on propagation and arrhythmogenesis. *Prog. Biophys. Mol. Biol.* **96**, 187–208 (2008).

103. Plonsey, R. & Barr, R. C. *Bioelectricity. A Quantitative Approach.* (1988).

104. Hulme, E. C. & Trevethick, M. A. Ligand binding assays at equilibrium: validation and interpretation. *Br. J. Pharmacol.* **161**, 1219–37 (2010).

105. Li, Z. *et al.* Assessment of an In Silico Mechanistic Model for Proarrhythmia Risk Prediction Under the CiPA Initiative. *Clin. Pharmacol. Ther.* **105**, 466–475 (2019).

106. Li, Z. *et al.* Improving the In Silico Assessment of Proarrhythmia Risk by Combining hERG (Human Ether-à-go-go-Related Gene) Channel-Drug Binding Kinetics and Multichannel Pharmacology. *Circ. Arrhythm. Electrophysiol.* **10**, e004628 (2017).

107. Dutta, S. *et al.* Optimization of an In silico Cardiac Cell Model for Proarrhythmia Risk Assessment. *Front. Physiol.* **8**, 616 (2017).

108. Penniman, J. R., Kim, D. C., Salata, J. J. & Imredy, J. P. Assessing use-dependent inhibition of the cardiac Na± current (INa) in the PatchXpress automated patch clamp. *J. Pharmacol. Toxicol. Methods* **62**, 107–118 (2010).

109. Brennan, T. P., Fink, M., Rodriguez, B. & Tarassenko, L. T. Modelling effects of sotalol on action potential morphology using a novel markov model of the HERG channel. in *IFMBE Proceedings* vol. 16 50–53 (Springer Verlag, 2007).

110. Di Veroli, G. Y., Davies, M. R., Zhang, H., Abi-Gerges, N. & Boyett, M. R. High-throughput screening of drug-binding dynamics to HERG improves early drug safety assessment. *Am. J. Physiol. Circ. Physiol.* **304**, H104–H117 (2013).

111. Shah, R. R. Drugs, QT interval prolongation and ICH E14: The need to get it right. *Drug Safety* vol. 28 115–125 (2005).

112. Vassallo, P. & Trohman, R. G. Prescribing amiodarone: An evidence-based review of clinical indications. *Journal of the American Medical Association* vol. 298 1312–1322 (2007).

113. Lazzara, R. Amiodarone and torsade de pointes. *Annals of Internal Medicine* vol. 111 549–551 (1989).

114. Farkas, A. S. & Nattel, S. Minimizing repolarization-Related proarrhythmic risk in drug development and clinical practice. *Drugs* **70**, 573–603 (2010).

115. Adams, C. P. & Brantner, V. V. Spending on new drug development. *Health Econ.* **19**, 130–141 (2010).

116. Adams, C. P. & Brantner, V. V. Estimating the cost of new drug development: is it really 802 million dollars? *Health Aff.* **25**, 420–8 (2006).

117. Davie, C. *et al.* Comparative Pharmacology of Guinea Pig Cardiac Myocyte and Cloned hERG (I Kr) Channel. *J. Cardiovasc. Electrophysiol.* **15**, 1302–1309 (2004).

118. Fermini, B. *et al.* A New Perspective in the Field of Cardiac Safety Testing through the Comprehensive In Vitro Proarrhythmia Assay Paradigm. *J. Biomol. Screen.* **21**, 1–11 (2016).

119. Hancox, J. C., McPate, M. J., El Harchi, A. & Zhang, Y. H. The hERG Potassium Channel and hERG Screening for Drug-Induced Torsades de Pointes. *Pharmacol. Ther.* **119**, 118–132 (2008).

120. Hancox, J. C. & James, A. F. Refining insights into high-affinity drug binding to the human ether-à-go-go-related gene potassium channel. *Mol. Pharmacol.* **73**, 1592–5 (2008).

121. Witchel, H. J. The hERG potassium channel as a therapeutic target. *Expert Opinion on Therapeutic Targets* vol. 11 321–336 (2007).

122. Pollard, C. E. *et al.* An introduction to QT interval prolongation and non-clinical approaches to assessing and reducing risk. *Br. J. Pharmacol.* **159**, 12–21 (2010).

123. Shah, R. R. & Hondeghem, L. M. Refining detection of drug-induced proarrhythmia: QT interval and TRIaD. *Hear. Rhythm* **2**, 758–772 (2005).

124. Crumb, W. J., Vicente, J., Johannesen, L. & Strauss, D. G. An evaluation of 30 clinical drugs against the comprehensive in vitro proarrhythmia assay (CiPA) proposed ion channel panel. *Journal of Pharmacological and Toxicological Methods* vol. 81 251–262 (2016).

125. Colatsky, T. *et al.* The Comprehensive in Vitro Proarrhythmia Assay (CiPA) initiative - Update on progress. *Journal of Pharmacological and Toxicological Methods* (2016) doi:10.1016/j.vascn.2016.06.002.

126. Fermini, B. *et al.* A new perspective in the field of cardiac safety testing through the comprehensive in vitro proarrhythmia assay paradigm. *J. Biomol. Screen.* **21**, 1–11 (2016).

127. Obiol-Pardo, C., Gomis-Tena, J., Sanz, F., Saiz, J. & Pastor, M. A multiscale simulation system for the prediction of drug-induced cardiotoxicity. *J. Chem. Inf. Model.* **51**, 483–492 (2011).

128. Passini, E. *et al.* Human in silico drug trials demonstrate higher accuracy than animal models in predicting clinical pro-arrhythmic cardiotoxicity. *Front. Physiol.* **8**, 1–15 (2017).

129. Parikh, J., Gurev, V. & Rice, J. J. Novel two-step classifier for Torsades de Pointes risk stratification from direct features. *Front. Pharmacol.* **8**, 1–18 (2017).

130. DailyMed. https://dailymed.nlm.nih.gov/dailymed/index.cfm.

131. Tox Portal. www.tox-portal.net.

132. Kim, S. *et al.* PubChem Substance and Compound databases. *Nucleic Acids Res.* **44**, D1202-1213 (2016).

133. Wishart, D. S. *et al.* DrugBank 5.0: a major update to the DrugBank database for 2018. *Nucleic Acids Res.* **46**, D1074–D1082 (2018).

134. Elkins, R. C. *et al.* Variability in High-Throughput Ion-Channel

Screening Data and Consequences for Cardiac Safety Assessment. *J. Pharmacol. Toxicol. Methods* **68**, 112–122 (2013).

135. Okada, J. -i. *et al.* Screening system for drug-induced arrhythmogenic risk combining a patch clamp and heart simulator. *Sci. Adv.* **1**, 142 (2015).

136. Lancaster, M. C. & Sobie, E. A. Improved Prediction of Drug-Induced Torsades de Pointes Through Simulations of Dynamics and Machine Learning Algorithms. *Clin. Pharmacol. Ther.* **100**, 371–9 (2016).

137. Carter, J. V., Pan, J., Rai, S. N. & Galandiuk, S. ROC-ing along: Evaluation and interpretation of receiver operating characteristic curves. *Surg. (United States)* **159**, 1638–1645 (2016).

138. Cantilena, L., Koerner, J., Temple, R. & Throckmorton, D. FDA evaluation of cardiac repolarization data for 19 drugs and drug candidates. *Clin. Pharmacol. Ther.* **79**, 29 (2006).

139. Zicha, S. *et al.* Molecular basis of species-specific expression of repolarizing K+ currents in the heart. *Am. J. Physiol. Heart Circ. Physiol.* **285**, 1641–1649 (2003).

140. Virág, L. *et al.* The slow component of the delayed rectifier potassium current in undiseased human ventricular myocytes. *Cardiovasc. Res.* **49**, 790–797 (2001).

141. Cubeddu, L. X. Drug-induced Inhibition and Trafficking Disruption of ion Channels: Pathogenesis of QT Abnormalities and Drug-induced Fatal Arrhythmias. *Curr. Cardiol. Rev.* **12**, 141–54 (2016).

142. Liu, H., Atkins, J. & Kass, R. S. Common Molecular Determinants of Flecainide and Lidocaine Block of Heart Na $^{+}$ Channels. *J. Gen. Physiol.* **121**, 199–214 (2003).

143. Kanlop, N., Chattipakorn, S. & Chattipakorn, N. Effects of cilostazol in the heart. *J. Cardiovasc. Med.* **12**, 88–95 (2011).

144. Iram, F., Ali, S., Ahmad, A., Khan, S. A. & Husain, A. A review on dronedarone: Pharmacological, pharmacodynamic and pharmacokinetic profile. *J. Acute Dis.* **5**, 102–108 (2016).

145. Zhang, X. *et al.* Thorough QT/QTc study of ritonavir-boosted saquinavir following multiple-dose administration of therapeutic and supratherapeutic doses in healthy participants. *J. Clin. Pharmacol.* **52**, 520–9 (2012).

146. Lu, H. R. *et al.* Predicting drug-induced slowing of conduction and pro-arrhythmia: identifying the 'bad' sodium current blockers. *Br. J. Pharmacol.* **160**, 60–76 (2010).

147. Wiśniowska, B. & Polak, S. Am I or am I not proarrhythmic? Comparison of various classifications of drug TdP propensity. *Drug Discov. Today* **22**, 10–16 (2017).

148. Chang, K. C. *et al.* Uncertainty quantification reveals the importance of data variability and experimental design considerations for in silico proarrhythmia risk assessment. *Front. Physiol.* **8**, 1–17 (2017).

149. Gomis-Tena, J. *et al.* When Does the IC50 Accurately Assess the Blocking Potency of a Drug? *J. Chem. Inf. Model.* (2020) doi:10.1021/acs.jcim.9b01085.

150. Brugada, J., Brugada, R. & Brugada, P. Channelopathies: A new category of diseases causing sudden death. *Herz* vol. 32 185–191 (2007).

151. Satler, C. a, Vesely, M. R., Duggal, P., Ginsburg, G. S. & Beggs, a H. Multiple different missense mutations in the pore region of HERG in patients with long QT syndrome. *Hum. Genet.* **102**, 265–272 (1998).

152. Wilde, A. A. M. & Amin, A. S. Clinical Spectrum of SCN5A Mutations: Long QT Syndrome, Brugada Syndrome, and Cardiomyopathy. *JACC Clin. Electrophysiol.* **4**, 569–579 (2018).

153. Han, D., Tan, H., Sun, C. & Li, G. Dysfunctional Nav1.5 channels due to SCN5A mutations. *Experimental Biology and Medicine* vol. 243 852–863 (2018).

154. He, F. Z., McLeod, H. L. & Zhang, W. Current pharmacogenomic studies on hERG potassium channels. *Trends Mol. Med.* **19**, 227–238 (2013).

155. Alonso-Atienza, F., Requena-Carrión, J., Rojo-Álvarez, J. L., Berenfeld, O. & Jalife, J. Action potential alternans in LQT3 syndrome: A simulation study. in *Annual International Conference of the IEEE Engineering in Medicine and Biology - Proceedings* vol. 2007 640–643 (Conf Proc IEEE Eng Med Biol Soc, 2007).

156. Yang, P.-C. *et al.* A computational model predicts adjunctive pharmacotherapy for cardiac safety via selective inhibition of the late cardiac Na current. *J. Mol. Cell. Cardiol.* **99**, 151–161 (2016).

157. Silva, J. & Rudy, Y. Subunit Interaction Determines I Ks Participation in Cardiac Repolarization and Repolarization Reserve. *Circulation* **112**, 1384–1391 (2005).

158. Zareba, W. *et al.* Influence of the genotype on the clinical course of the long-QT syndrome. *N. Engl. J. Med.* **339**, 960–965 (1998).

159. Weiss, J. N., Garfinkel, A., Karagueuzian, H. S., Chen, P. S. & Qu, Z.

Early afterdepolarizations and cardiac arrhythmias. *Hear. Rhythm* **7**, 1891–1899 (2010).

160. Huang, H., Priori, S. G., Napolitano, C., O'Leary, M. E. & Chahine, M. Y1767C, a novel SCN5A mutation, induces a persistent Na+ current and potentiates ranolazine inhibition of Nav1.5 channels. *Am. J. Physiol. - Hear. Circ. Physiol.* **300**, (2011).

161. January, C. T. & Riddle, J. M. Early afterdepolarizations: Mechanism of induction and block. A role for L-type Ca2+ current. *Circ. Res.* **64**, 977–990 (1989).

162. Jervel, A. & Lange-Nielsen, F. Deafness, electrocardiographic abnormalities and sudden death. *JAMA J. Am. Med. Assoc.* **201**, 624–625 (1967).

163. Moss, A. J. & McDonald, J. Unilateral cervicothoracic sympathetic ganglionectomy for the treatment of long QT interval syndrome. *N. Engl. J. Med.* **285**, 903–904 (1971).

164. Johnson, J. N. & Ackerman, M. J. QTc: How long is too long? *British Journal of Sports Medicine* vol. 43 657–662 (2009).

165. Migdalovich, D. *et al.* Mutation and gender-specific risk in type 2 long QT syndrome: Implications for risk stratification for life-threatening cardiac events in patients with long QT syndrome. *Hear. Rhythm.* **8**, 1537–1543 (2011).

166. Alings, M. & Wilde, A. 'Brugada' syndrome: Clinical data and suggested pathophysiological mechanism. *Circulation* **99**, 666–673 (1999).

167. Berecki, G. *et al.* Long-QT syndrome-related sodium channel mutations probed by the dynamic action potential clamp technique. *J. Physiol.* **570**, 237–250 (2006).

168. Tan, B. H. *et al.* A novel C-terminal truncation SCN5A mutation from a patient with sick sinus syndrome, conduction disorder and ventricular tachycardia. *Cardiovasc. Res.* **76**, 409–417 (2007).

169. Benson, D. W. *et al.* Congenital sick sinus syndrome caused by recessive mutations in the cardiac sodium channel gene (SCN5A). *J. Clin. Invest.* **112**, 1019–1028 (2003).

170. Ortiz-Bonnin, B. *et al.* Electrophysiological characterization of a large set of novel variants in the SCN5A-gene: identification of novel LQTS3 and BrS mutations. *Pflugers Arch. Eur. J. Physiol.* **468**, 1375–1387 (2016).

171. Deschênes, I. *et al.* Electrophysiological characterization of SCN5A

mutations causing long QT (E1784K) and Brugada (R1512W and R1432G) syndromes. *Cardiovasc. Res.* **46**, 55–65 (2000).

172. Chadda, K. R., Jeevaratnam, K., Lei, M. & Huang, C. L.-H. Sodium channel biophysics, late sodium current and genetic arrhythmic syndromes. *Pflugers Arch.* **469**, 629–641 (2017).

173. Horne, A. J., Eldstrom, J., Sanatani, S. & Fedida, D. A novel mechanism for LQT3 with 2:1 block: a pore-lining mutation in Nav1.5 significantly affects voltage-dependence of activation. *Hear. Rhythm* **8**, 770–7 (2011).

174. Blich, M. *et al.* Specific Therapy Based on the Genotype in a Malignant Form of Long QT3, Carrying the V411M Mutation. *Int. Heart J.* **60**, 979–982 (2019).

175. Carrasco, J. I. *et al.* Flecainide, a Therapeutic Option in a Patient With Long QT Syndrome Type 3 Caused by the Heterozygous V411M Mutation in the SCN5A Gene. *Rev. Española Cardiol. (English Ed.* **65**, 1058–1059 (2012).

176. Maltsev, V. A. & Undrovinas, A. Late sodium current in failing heart: Friend or foe? *Prog. Biophys. Mol. Biol.* **96**, 421–451 (2008).

177. Saint, D. A. The cardiac persistent sodium current: an appealing therapeutic target? *Br. J. Pharmacol.* **153**, 1133–1142 (2009).

178. Trenor, B. *et al.* Simulation and Mechanistic Investigation of the Arrhythmogenic Role of the Late Sodium Current in Human Heart Failure. *PLoS One* **7**, e32659 (2012).

179. Makielski, J. C. Late sodium current: A mechanism for angina, heart failure, and arrhythmia. *Trends Cardiovasc. Med.* **26**, 115–22 (2016).

180. Nagatomo, T. *et al.* Temperature dependence of early and late currents in human cardiac wild- type and long Q-T ΔKPQ Na+ channels. *Am. J. Physiol. - Hear. Circ. Physiol.* **275**, 2016–2024 (1998).

181. Nagatomo, T., January, C. T. & Makielski, J. C. Preferential block of late sodium current in the LQT3 DeltaKPQ mutant by the class I(C) antiarrhythmic flecainide. *Mol. Pharmacol.* **57**, 101–107 (2000).

182. Belardinelli, L. *et al.* A novel, potent, and selective inhibitor of cardiac late sodium current suppresses experimental arrhythmias. *J. Pharmacol. Exp. Ther.* **344**, 23–32 (2013).

183. Noble, D. & Noble, P. J. Late sodium current in the pathophysiology of cardiovascular disease: consequences of sodium-calcium overload. *Heart* **92 Suppl 4**, iv1–iv5 (2006).

184. Horvath, B. *et al.* Dynamics of the late Na(+) current during cardiac action potential and its contribution to afterdepolarizations. *J. Mol. Cell. Cardiol.* **64**, 59–68 (2013).

185. Hegyi, B. *et al.* β-adrenergic regulation of late Na+ current during cardiac action potential is mediated by both PKA and CaMKII. *J. Mol. Cell. Cardiol.* **123**, 168–179 (2018).

186. Horváth, B. *et al.* Late sodium current in human, canine and guinea pig ventricular myocardium. *J. Mol. Cell. Cardiol.* **139**, 14–23 (2020).

187. Soltis, A. R. & Saucerman, J. J. Synergy between CaMKII substrates and β-adrenergic signaling in regulation of cardiac myocyte Ca2 handling. *Biophys. J.* **99**, 2038–2047 (2010).

188. Moss, A. J. *et al.* Effectiveness and Limitations of β-Blocker Therapy in Congenital Long-QT Syndrome. *Circulation* **101**, 616–623 (2000).

189. Abu-Zeitone, A., Peterson, D. R., Polonsky, B., McNitt, S. & Moss, A. J. Efficacy of different beta-blockers in the treatment of long QT syndrome. *J. Am. Coll. Cardiol.* **64**, 1352–1358 (2014).

190. Priori, Silvia, Schwartz, P. J., Grillo, M. & Bottelli, G. Association of Long QT Syndrome Loci and Cardiac Events Among Patients Treated With beta-Blockers. *Jama* **292**, 1341–1344 (2004).

191. Priori, S. G. *et al.* Task Force on sudden cardiac death of the European Society of Cardiology. *Eur. Heart J.* **22**, 1374–1450 (2001).

192. Foody, J. M., Farrell, M. H. & Krumholz, H. M. β-blocker therapy in heart failure: Scientific review. *J. Am. Med. Assoc.* **287**, 883–889 (2002).

193. Mazzanti, A. *et al.* Gene-specific therapy with mexiletine reduces arrhythmic events in patients with long QT syndrome type 3. *J. Am. Coll. Cardiol.* **67**, 1053–1058 (2016).

194. Chorin, E. *et al.* Ranolazine for Congenital Long-QT Syndrome Type III: Experimental and Long-Term Clinical Data. *Circ. Arrhythm. Electrophysiol.* **9**, 139–148 (2016).

195. Thomas, S. H. L. & Behr, E. R. Pharmacological treatment of acquired QT prolongation and torsades de pointes. *Br. J. Clin. Pharmacol.* **81**, 420–427 (2016).

196. Anderson, H. N. *et al.* Lidocaine attenuation testing: An in vivo investigation of putative LQT3-associated variants in the SCN5A-encoded sodium channel. *Hear. Rhythm* **14**, 1173–1179 (2017).

197. Wang, G. K., Russell, G. & Wang, S.-Y. Persistent human cardiac Na+

currents in stably transfected mammalian cells: Robust expression and distinct open-channel selectivity among Class 1 antiarrhythmics. *Channels (Austin).* **7**, 263–74 (2013).

198. Groenewegen, W. A. *et al.* A novel LQT3 mutation implicates the human cardiac sodium channel domain IVS6 in inactivation kinetics. *Cardiovasc. Res.* **57**, 1072–1078 (2003).

199. Aliot, E., Capucci, A., Crijns, H. J., Goette, A. & Tamargo, J. Twenty-five years in the making: Flecainide is safe and effective for the management of atrial fibrillation. *Europace* **13**, 161–173 (2011).

200. Chorin, E. *et al.* Long-term flecainide therapy in type 3 long QT syndrome. *Europace* **20**, 370–376 (2018).

201. Zhu, Y., Kyle, J. W. & Lee, P. J. Flecainide sensitivity of a Na channel long QT mutation shows an open-channel blocking mechanism for use-dependent block. *Am. J. Physiol. - Hear. Circ. Physiol.* **291**, 29–37 (2006).

202. Wehrens, X. H. T., Abriel, H., Cabo, C., Benhorin, J. & Kass, R. S. Arrhythmogenic Mechanism of an LQT-3 Mutation of the Human Heart Na $^{+}$ Channel α-Subunit. *Circulation* **102**, 584–590 (2000).

203. Sicouri, S., Belardinelli, L. & Antzelevitch, C. Antiarrhythmic effects of the highly selective late sodium channel current blocker GS-458967. *Hear. Rhythm* **10**, 1036–1043 (2013).

204. Pignier, C. *et al.* Selective inhibition of persistent sodium current by F 15845 prevents ischaemia-induced arrhythmias. *Br. J. Pharmacol.* **161**, 79–91 (2010).

205. Bacic, D. *et al.* Eleclazine, an inhibitor of the cardiac late sodium current, is superior to flecainide in suppressing catecholamine-induced ventricular tachycardia and T-wave alternans in an intact porcine model. *Hear. Rhythm* **14**, 448–454 (2017).

206. Vacher, B., Pignier, C., Létienne, R., Verscheure, Y. & Le Grand, B. F 15845 inhibits persistent sodium current in the heart and prevents angina in animal models. *Br. J. Pharmacol.* **156**, 214–225 (2009).

207. Postema, P. G., De Jong, J. S. S. G., Van der Bilt, I. A. C. & Wilde, A. A. M. Accurate electrocardiographic assessment of the QT interval: Teach the tangent. *Hear. Rhythm* **5**, 1015–1018 (2008).

208. Colquhoun, D., Dowsland, K. a, Beato, M. & Plested, A. J. R. How to impose microscopic reversibility in complex reaction mechanisms. *Biophys. J.* **86**, 3510–3518 (2004).

209. Roberts, B. N., Yang, P. C., Behrens, S. B., Moreno, J. D. & Clancy,

C. E. Computational approaches to understand cardiac electrophysiology and arrhythmias. *American Journal of Physiology - Heart and Circulatory Physiology* vol. 303 766–783 (2012).

210. Vandenberg, C. A. & Bezanilla, F. A sodium channel gating model based on single channel, macroscopic ionic, and gating currents in the squid giant axon. *Biophys. J.* **60**, 1511–1533 (1991).

211. Vanier, M. C. & Bower, J. M. A comparative survey of automated parameter-search methods for compartmental neural models. *J. Comput. Neurosci.* **7**, 149–171 (1999).

212. Milescu, L. S., Akk, G. & Sachs, F. Maximum likelihood estimation of ion channel kinetics from macroscopic currents. *Biophys. J.* **88**, 2494–2515 (2005).

213. Chen, F., Chu, A., Yang, X., Lei, Y. & Chu, J. Identification of the parameters of the beeler-reuter ionic equation with a partially perturbed particle swarm optimization. *IEEE Trans. Biomed. Eng.* **59**, 3412–3421 (2012).

214. Weber, F. M. *et al.* Adaptation of a minimal four-state cell model for reproducing atrial excitation properties. in *Computers in Cardiology* vol. 35 61–64 (2008).

215. Dokos, S. & Lovell, N. H. Parameter estimation in cardiac ionic models. in *Progress in Biophysics and Molecular Biology* vol. 85 407–431 (Prog Biophys Mol Biol, 2004).

216. Guo, T., Al Abed, A., Lovell, N. H. & Dokos, S. Optimisation of a generic ionic model of cardiac myocyte electrical activity. *Comput. Math. Methods Med.* **2013**, (2013).

217. Groenendaal, W. *et al.* Cell-specific cardiac electrophysiology models. *PLoS Comput. Biol.* **11**, e1004242 (2015).

218. Nelder, J. A. & Mead, R. A Simplex Method for Function Minimization. *Comput. J.* **7**, 308–313 (1965).

219. Lagarias, J. C., Reeds, J. a., Wright, M. H. & Wright, P. E. Convergence Properties of the Nelder--Mead Simplex Method in Low Dimensions. *SIAM J. Optim.* **9**, 112–147 (1998).

220. Caballero, R. *et al.* Flecainide increases Kir2.1 currents by interacting with cysteine 311, decreasing the polyamine-induced rectification. *Proc. Natl. Acad. Sci.* **107**, 15631–15636 (2010).

221. Paul, A. A., Witchel, H. J. & Hancox, J. C. Inhibition of the current of heterologously expressed HERG potassium channels by flecainide and comparison with quinidine, propafenone and lignocaine. *Br. J.*

Pharmacol. **136**, 717–29 (2002).

222. Matsukawa, H., Izumi, T., Yamaguchi, M., Tomizawa, S. & Ohshiro, H. Safety Pharmacology Assessment of Cardiac Ion Channels by Manual Patch Clamp With CiPA Protocols. Poster session presented at 2019 annual meeting of Safety Pharamacology Society, Barcelona, ES. **September**, (2019).

223. Antzelevitch, C. *et al.* Electrophysiological effects of ranolazine, a novel antianginal agent with antiarrhythmic properties. *Circulation* **110**, 904–10 (2004).

224. Kaufman, E. S. Use of ranolazine in long-QT syndrome type 3. *J. Cardiovasc. Electrophysiol.* **19**, 1294–5 (2008).

225. Moss, A. J. *et al.* Ranolazine shortens repolarization in patients with sustained inward sodium current due to type-3 long-QT syndrome. *J. Cardiovasc. Electrophysiol.* **19**, 1289–1293 (2008).

226. Moss, A. J. *et al.* Safety and efficacy of flecainide in subjects with long QT-3 syndrome (ΔKPQ mutation): A randomized, double-blind, placebo-controlled clinical trial. in *Annals of Noninvasive Electrocardiology* vol. 10 59–66 (2005).

227. Melgari, D., Zhang, Y., El Harchi, A., Dempsey, C. E. & Hancox, J. C. Molecular basis of hERG potassium channel blockade by the class Ic antiarrhythmic flecainide. *J. Mol. Cell. Cardiol.* **86**, 42–53 (2015).

228. Ducroq, J. *et al.* Action potential experiments complete hERG assay and QT-interval measurements in cardiac preclinical studies. *J. Pharmacol. Toxicol. Methods* **56**, 159–170 (2007).

229. Lu, H. R., Vlaminckx, E. & Gallacher, D. J. Choice of cardiac tissue in vitro plays an important role in assessing the risk of drug-induced cardiac arrhythmias in human: beyond QT prolongation. *J. Pharmacol. Toxicol. Methods* **57**, 1–8 (2008).

230. Smallwood, J. K., Robertson, D. W. & Steinberg, M. I. Electrophysiological effects of flecainide enantiomers in canine Purkinje fibres. *Naunyn. Schmiedebergs. Arch. Pharmacol.* **339**, 625–629 (1989).

231. Wang, D. W., Yazawa, K., Makita, N., George, A. L. & Bennett, P. B. Pharmacological targeting of long QT mutant sodium channels. *J. Clin. Invest.* **99**, 1714–20 (1997).

232. Guo, D. & Jenkinson, S. Simultaneous assessment of compound activity on cardiac Nav1.5 peak and late currents in an automated patch clamp platform. *J. Pharmacol. Toxicol. Methods* **99**, 106575 (2018).

233. Anyukhovsky, E. P., Sosunov, E. A. & Rosen, M. R. Regional Differences in Electrophysiological Properties of Epicardium, Midmyocardium, and Endocardium. *Circulation* **94**, 1981–1988 (1996).

234. Liu, N., Napolitano, C., Venetucci, L. A. & Priori, S. G. Flecainide and Antiarrhythmic Effects in a Mouse Model of Catecholaminergic Polymorphic Ventricular Tachycardia. *Trends Cardiovasc. Med.* **22**, 35–39 (2012).

235. Lampert, A. & Korngreen, A. *Markov Modeling of Ion Channels*. *Computational Neuroscience* vol. 123 (Elsevier Inc., 2014).

236. Johannesen, L. *et al.* Late Sodium Current Block for Drug-Induced Long QT Syndrome: Results from a Prospective Clinical Trial. *Clin. Pharmacol. Ther.* **99**, 214–223 (2016).

237. Ben-Shalom, R., Aviv, A., Razon, B. & Korngreen, A. Optimizing ion channel models using a parallel genetic algorithm on graphical processors. *J. Neurosci. Methods* **206**, 183–194 (2012).

238. Ben-Shalom, R., Liberman, G. & Korngreen, A. Accelerating compartmental modeling on a graphical processing unit. *Front. Neuroinform.* **7**, (2013).

239. Perissinotti, L. L. *et al.* Kinetic Model for NS1643 Drug Activation of WT and L529I Variants of Kv11.1 (hERG1) Potassium Channel. *Biophys. J.* **108**, 1414–1424 (2015).

240. Maltsev, V. A., Sabbah, H. N. & Undrovinas, A. I. Late Sodium Current is a Novel Target for Amiodarone: Studies in Failing Human Myocardium. *J. Mol. Cell. Cardiol.* **33**, 923–932 (2001).

241. Zhu, W. *et al.* Predicting patient response to the antiarrhythmic mexiletine based on genetic variation: Personalized medicine for long QT syndrome. *Circ. Res.* **124**, 539–552 (2019).

242. Ficker, E., Jarolimek, W., Kiehn, J., Baumann, a & Brown, a M. Molecular determinants of dofetilide block of HERG K+ channels. *Circ. Res.* **82**, 386–395 (1998).

243. Clancy, C. E. & Kass, R. S. Defective cardiac ion channels: From mutations to clinical syndromes. *J. Clin. Invest.* **110**, 1075–1077 (2002).